Dissertation
submitted to the
Combined Faculties for the Natural Sciences
and for Mathematics
of the Ruperto-Carola University of Heidelberg,
Germany
for the degree of
Doctor of Natural Sciences

presented by
Dipl.-Phys. Albrecht Haase
born in: Berlin
Oral examination: June 29$^{\text{th}}$, 2005

Single atom detection in low finesse cavities

Referees: Prof. Dr. Jörg Schmiedmayer
Prof. Dr. Markus Oberthaler

Zusammenfassung

Detektion einzelner Atome in Resonatoren niedriger Finesse

Im Rahmen dieser Doktorarbeit wurde der Grundstein gelegt für die Integration mikrooptischer Elements auf Atomchips. Dies beinhaltete theoretische und experimentelle Untersuchungen zur Möglichkeit der Detektion einzelner Atome mit Hilfe von optischen Resonatoren niedriger Güte. Hierfür wurde ein theoretisches Model zur Beschreibung des gekoppelten Systems Atom-Resonator entwickelt. Angewandt auf einen optischen Faserresonator auf dem Atomchip, sagt dieses Model das Erreichen eines Signal-zu-Rausch-Verhältnisses von über 30 für die Einzelatomdetektion voraus, für Meßintervalle von 10μs.
Des weiteren wurde ein Experiment mit kalten Rubidium Atomen aufgebaut, das den ersten Atomchip mit integriertem Faserresonator aufnehmen wird. Eine Serie von Experimenten mit einem makroskopischen Testresonator, der in seinen Eigenschaften einem Faserresonantor gleicht, wurde durchgeführt. Indem man den Resonator sehr nah am konzentrischen Punkt betreibt, kann dessen Fokusbreite auf 12μm reduziert werden, bei einer Finesse von 1200. Diese Parameter liegen in der gleichen Größenordnung wie die eines Faserresonators. Experimente mit Atomen, die frei durch den Resonator fallen oder mit Hilfe eines magnetischen Leiters hindurchgeführt werden, bestätigten die Voraussagen der Theorie bezüglich des Einflusses der Atome auf das Resonatortransmissionssignal.

Abstract

Single atom detection in low finesse cavities

Within the framework of this thesis the cornerstone for the integration of microoptical elements for single atom manipulation on atom chips was laid. This involved theoretical and experimental investigations of the possibility of single atom detection in optical low finesse cavities. A theoretical model was developed to describe the coupled atom-cavity system. This model was applied to an experimentally feasible on-chip optical fibre cavity. A signal-to-noise ratio of above 30 for single atom detection with such a device within 10μs is predicted.
Furthermore, an experiment with cold rubidium atoms was constructed. It is going to host the first fibre cavity chip. The theory was verified by a series of experiments with a macroscopic test resonator modelling the fibre cavity setup. By operating the resonator close to the concentric limit, the cavity mode waist was decreased to 12μm at a finesse of 1200. This is on the same order of magnitude as the fibre cavity parameters. Experiments with atoms falling freely or being magnetically guided through the cavity have confirmed the theoretical predictions for the atomic effect on the cavity transmission signal.

Contents

1 Introduction

In the 100th year after Einstein's first epoch making discoveries, this introduction into the physics of atom-light interaction can not begin differently than by emphasizing his big contributions to the subject. It all began with his Nobel-prize-awarded work "On a heuristic viewpoint concerning the production and transformation of light" [Ein05], which proposed the existence of light quanta, later called photons, to describe the photoelectric effect. Later in his work "On the quantum theory of light", he proposed the process of stimulated emission besides absorption and spontaneous emission and set up simple rate equations including the famous Einstein coefficients to describe those processes [Ein17].
For a long time the spontaneous emission rate was believed to be an intrinsic property of matter, until later it was understood that spontaneous emission is a property of the coupled atom-vacuum system, strongly dependent on the surrounding environment, which defines the local mode density. Purcell was able to quantify this phenomenon through his spontaneous emission enhancement factor, given by the ratio of local mode density close to a surface and the free space mode density [Pur46].
In the following times, the effect of boundary conditions on atomic radiation was intensively studied by theorists [Bar70, Mor73, Mil73, Kle81] and, as soon as the required techniques had been developed to prepare, control, and observe isolated atoms and molecules close to surfaces, also experimental evidence was found. Pioneering experiments have been carried out by Dexhage, examining the fluorescence of organic dyes deposited on organic dyes above metallic mirrors [Dex74]. The first serious inhibition of spontaneous emission by a factor of 20 for a Rydberg atom between parallel conducting plates has been observed by the group of Kleppner in [Hul85], while the Haroche group observed no spontaneous decay during 13 natural lifetimes of Cesium atoms placed in a μm-sized gap between two metallic mirrors [Jhe87]. This results reflect the fact that the mode density decreases drastically as soon as the atom surface distance falls below half the wavelength.
Another milestone was reached after being able to build resonant cavities. If their length is much larger then half the wavelength,these cavities enhance vacuum fluctuations instead of surpressing them. The resulting enhancement of spontaneous emission has been observed for the first time in experiments performed by the Haroche group, where an enhancement factor of 500 for Sodium Rydberg atoms in a microwave cavity was measured [Goy83]. By varying the cavity length over both regimes enhancement as well as inhibition of spontaneous emission in the optical regime could be observed in [Hei87a, DeM87].
All these first experiment were paving the way to a new field called cavity quantum electrodynamics (CQED) [Ber94]. From then on a race started to constantly increase

the quality of the cavities, in order to decreases the decay rate of the cavity field. An important stage in this race was the transition from the weak to the strong coupling regime, where the atom-light-coupling constant becomes larger than the cavity decay rate and the spontaneous emission rate. A first example was an experiment performed in the Walther group [Mes85]. As long as the cavity decay rate was much larger than the rate at which atoms from an atomic beam were passing a microwave cavity, no interaction was possible between an atom and a photon emitted by its forerunner. But the more the cavity decay rate was reduced, the stronger the atom-field coupling became and the stronger the field was building up in the cavity, until a steady state was reached, called the single-atom maser.
From then on, more and more cavity QED effects could be observed. Changes in the frequency and linewidth for spontaneous emission in a cavity have been found in [Hei87b], the van der Waals interaction between an atom and its mirror image in the cavity walls were measured in [San92], optical bistabillity was observed [Rem91], and the single atom vacuum Rabi splitting could be resolved in [Tho92], reflecting the fact that the resonance of an atom, which is dressed by the cavity field in the strong coupling regime is splitting up into two normal modes as described by the Jaynes-Cummings model [Jay63, Tra68].
In the 90's the field of cavity QED took advantage of the powerful recently gained ability of cooling and trapping atoms by laser light. This technique was proposed already in [Hae75] and a realization in form of the first magneto-optical trap for neutral atoms was achieved in [Raa87]. From then on, cold atoms could be used to study their interaction with cavity fields. This led to outstanding experiments mainly in the groups of Kimble and Rempe. The most important among them were the observation of single atom trajectories within a cavity [Hoo98], the trapping of single atoms with single photons in a cavity [Pin00, Hoo00], the realization of an one atom laser [McK03], the cooling of single atoms by a cavity [Mau04], and the observation of the normal mode splitting of a single trapped atom [Mau05].
Besides experiments exploring the fundamental physics of coupled atom-cavity systems, the first applications came about, like for instance a deterministic source of single photons [Kuh02, McK04], which is of big relevance in quantum communication [Ben92], or the realization of a quantum phase gate [Rau99] and the engineering of multiparticle entanglement [Rau00], both fundamental ingredients for quantum information processing [Nie00].
This work presented in this thesis tries to combine the powerful technologies, developed in the experiments described so far, with another, much younger field of quantum optics, the manipulation of cold atoms on atom chips [Fol00, Fol02]. Atom chips are semiconductor chips carrying nanofabricated metal structures [Gro04], which allow to produce customized magnetic and electric potentials to implement a large variety of quantum optical elements for cold atom manipulation. To give a few examples of what has been achieved so far, besides the implementation of atomic waveguides [Luo04], beamsplitters [Cas00], trap arrays [Kru03], and conveyer belts [Hae01], Bose-Einstein condensation has been achieved in atom chip traps [Ott01, Hae01, Lea02, Sch03], and its coherence properties have been studied [Tre04]. Considering that all this experiments can be combined on a single device, the atom chip is quickly developing into a microfabricated,

integrated quantum optics lab.
On the other hand, the elements which are so far integrated in the atom chip, are using only electric and magnetic potentials to manipulate the atoms. The light which is involved in every experiment with atom chips, is still coming from macroscopic laser beams. In order to complete the concept of a fully integrated quantum optics toolbox, the missing building block is integrated microoptics, which brings light to certain spots in order to prepare, manipulate, and detect the atoms locally. To enhance the atom-light interaction, central elements will be integrated microcavities and, as the trapping potentials are on the way to precisely control the dynamics of single atoms, also the microcavity should be able to resolve a single atom passing through the mode.
This thesis describes the first step towards this goal. In this work, the feasibility of the concept of single-atom detection with an on-chip microcavity has been examined theoretically and an experiment was set up to test all required components. The thesis is structured in the following way: In Chapter 2 an introduction to the theory of resonators is given, including first considerations about a possible microcavity geometry. Chapter 3 is devoted to the theory of atom-light interaction, and a model is developed, which describes the coupled atom-microcavity system. At the end of this chapter a few remarks on the generalization to many atom systems are made. In Chapter 4, the experimental setup is presented, which consists in a source of cold Rubidium atoms, whose interactions with a macroscopic test cavity are studied. Moreover, the first steps to include an atomchip with integrated microcavity based on optical fibres are described. Chapter 5 presents first experiments with this test cavity which was constructed to model the future microcavitiy setup. Finally in Chapter 5.5, some conclusions are drawn and an outlook is given on future perspectives of integrated microcavities on atom chips.

2 Resonator Theory

Beside an introduction to the theory of optical resonators, in this Chapter, a resonator geometry shell be identified, where the mode waist can be made extremely small, which is favourable to enhance the interaction with atoms placed into the cavity waist, as it will be explained in detail in Chapter 3. The experimental realizability and possible constrains on this resonator geometry shell be discussed.
In Section 2.1 the wave equation for beam-like intensity distributions is derived and Gaussian beams as its solutions are introduced. In Section 2.2 these concepts are extended from free space beams to resonator modes. The problem of matching the incoming beam to the cavity mode is treated in Section 2.3. In Section 2.4.4 different cavity geometries are introduced, their properties are discussed and their stability is evaluated. Finally, a setup for an optical fibre resonator is proposed in Section 2.5.

2.1 Wave optics and Gaussian beams

2.1.1 Paraxial wave equation

Electromagnetic fields in free space are generally described by the Helmholtz-equation

$$\left[\nabla^2 + k^2\right] E(x,y,z) = 0. \tag{2.1}$$

Let us consider a field distribution propagating beam-like in the z-direction, meaning that the intensity distribution in the radial directions (x,y) is decreasing rapidly. The main variation in the z-direction is a plain wave propagation factor which can be extracted $E(x,y,z) = \mathcal{E}(x,y,z)e^{-ikz}$. This leads to a reduced wave equation for $\mathcal{E}$

$$\frac{\partial^2\mathcal{E}}{\partial x^2} + \frac{\partial^2\mathcal{E}}{\partial y^2} + \frac{\partial^2\mathcal{E}}{\partial z^2} - 2ik\frac{\partial\mathcal{E}}{\partial z} = 0. \tag{2.2}$$

Furthermore, the amplitude $\mathcal{E}(x,y,z)$ is generally varying much slower as a function of z, than transversally, which can be expressed mathematically by the paraxial approximation

$$\left|\frac{\partial^2\mathcal{E}}{\partial z^2}\right| \ll \left|2k\frac{\partial\mathcal{E}}{\partial z}\right| \text{ or } \left|\frac{\partial^2\mathcal{E}}{\partial x^2}\right| \text{ or } \left|\frac{\partial^2\mathcal{E}}{\partial y^2}\right|. \tag{2.3}$$

In this approximation Equation 2.3 reduces to the paraxial wave equation

$$\frac{\partial^2\mathcal{E}}{\partial x^2} + \frac{\partial^2\mathcal{E}}{\partial y^2} - 2ik\frac{\partial\mathcal{E}}{\partial z} = 0. \tag{2.4}$$

This approximation is valid for describing almost all optical resonators. Discussions about its breakdown in the context of strongly focussed beams, where the beam waist becomes comparable with the wavelength, can be found in [vEnk00, vEnk01, vEnk04, Dom02]. This situation is so far not encountered in the systems described here.

2.1.2 Gaussian beams

Very useful, exact solutions of the paraxial wave equation are normalized Gaussian spherical waves, so called Gaussian beams (see [Sie86])

$$E(x,y,z) = \left(\frac{2}{\pi}\right)^{1/2} \frac{\exp\left[ikz - i\arctan\left(\frac{\lambda z}{\pi w_0^2}\right)\right]}{w(z)} \times \times \exp\left[-\frac{x^2+y^2}{w^2(z)} + ik\frac{x^2+y^2}{2R(z)}\right], \tag{2.5}$$

where $R(z)$ is the wave-front curvature and $w(z)$ the width of the transversal intensity profile. The quantity $w_0 = w(0)$ is the waist of the beam. This parameters are depicted in Figure 2.1. The quantity

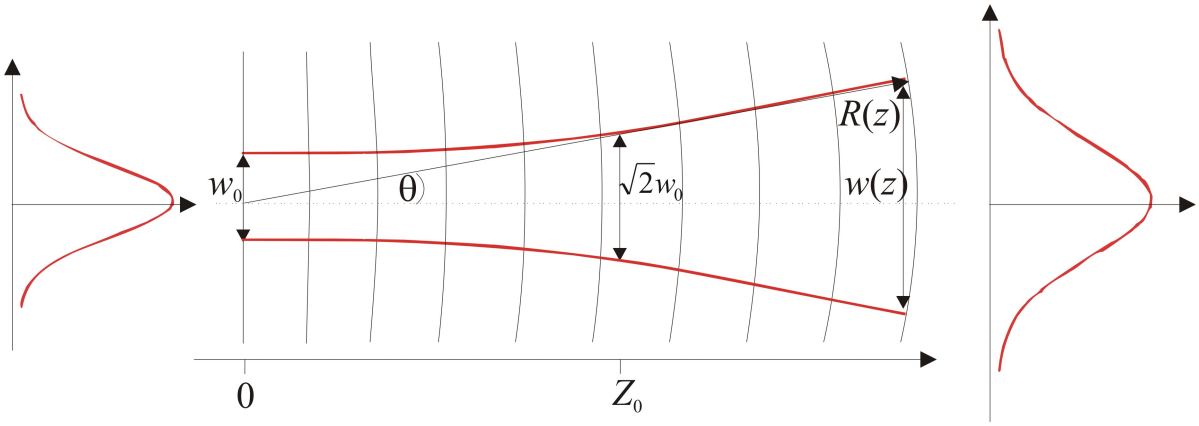

Figure 2.1: The parameters that define a Gaussian beam are waist size w_0 and the Rayleigh length z_0. They determine the spatial dependent beam width $w(z)$ and radius of curvature $R(z)$.

$$\varphi(z) = \arctan\left(\frac{\lambda z}{\pi w_0^2}\right) = \arctan\left(\frac{z}{z_0}\right), \tag{2.6}$$

is called the Guoy phase [Guo90], which is the phase shift acquired by a Gaussian beam in comparison to a spherical wave during the propagation in the axial direction z. The quantity z_0 is called the Rayleigh length

$$z_0 = \frac{\pi w_0^2}{\lambda}, \tag{2.7}$$

and its physical meaning will become clear later in this section.

The propagation of these Gaussian beams can be completely described by the so-called complex source point coordinates $q(z)$, defined as

$$\frac{1}{q(z)} = \frac{1}{R(z)} + i\frac{\lambda}{\pi w^2(z)}, \tag{2.8}$$

where the real part reflects the radius of curvature, and the imaginary part the beam width. At the beam waist the radius of curvature diverges, which determines

$$q(0) = q_0 = -i\frac{\pi w_0^2}{\lambda} = iz_0, \tag{2.9}$$

The Guoy phase term can be simplified in these coordinates, and one finds

$$\frac{\exp(-i\varphi(z))}{w(z)} = \frac{q_0}{w_0 q(-z)}. \tag{2.10}$$

Using this identity, the Gaussian spherical waves expressed in complex source point coordinates simplify as follows

$$E(x,y,z) = \left(\frac{2}{\pi}\right)^{1/2} \frac{q_0}{w_0 q(-z)} \exp\left[ikz - ik\frac{x^2+y^2}{2q(-z)}\right]. \tag{2.11}$$

Substituting this expression into the paraxial wave equation and assuming $z = 0$ to be the position of the beam waist, one finds the simple z-dependence of the quantity $q(z)$

$$q(z) = q_0 + z. \tag{2.12}$$

Equating separately the real and imaginary part of Equation 2.12 one finds for the radius of curvature

$$R(z) = z[1 + (z_0/z)^2] \tag{2.13}$$

and for the beam width

$$w(z) = w_0\sqrt{1 + (z/z_0)^2}. \tag{2.14}$$

Now the Rayleigh length z_0 (see Equation 2.7) can be identified as the distance from the beam waist, at which the beam width has expanded by a factor of $\sqrt{2}$. Finally the divergence angle of a Gaussian beam at large distances $z \gg z_0$ is given by

$$\theta \approx \frac{w(z)}{z} \approx \frac{\lambda}{\pi w_0}. \tag{2.15}$$

All this is sketched in Figure 2.1.
From these expressions describing a Gaussian beam, one sees that the field distribution is completely determined by the wavelength λ, the position of the waist, and the waist size w_0. The only restriction to these parameters is the requirement $w_0 \gg \lambda$ which was assumed for the derivation of the paraxial wave equation.

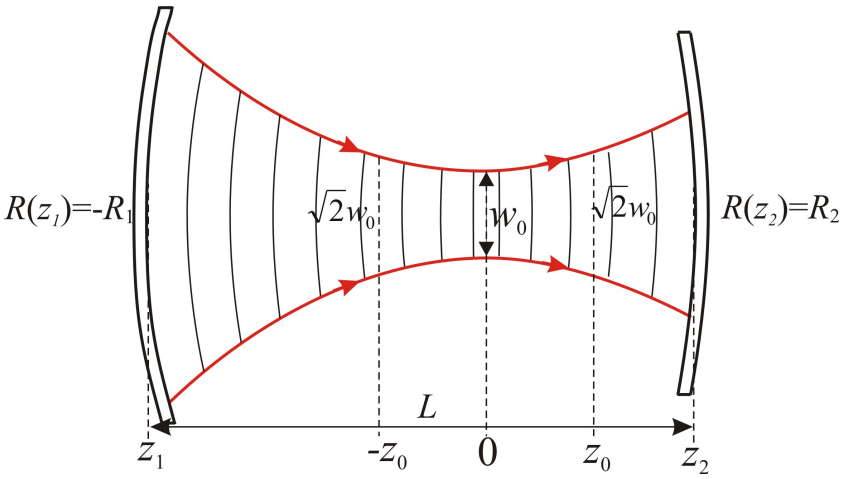

Figure 2.2: Sketch of a resonator, formed by two spherical mirrors. For a given resonator length L, the mirror positions $z_{1,2}$ relative to the position of the mode waist w_0, are determined by the radii of curvature of the mirrors $R_{1,2}$ as shown in Equations 2.18 and 2.19. At the Rayleigh length z_0, the beam has expanded by a factor of $\sqrt{2}$ compared to its waist.

2.2 Gaussian resonator modes

The characteristics of Gaussian beams will now be used to find a description of the modes of optical resonators formed by two concave mirrors of curvatures R_1 and R_2. The two mirrors are positioned on the z-axis at z_1 and at z_2 as depicted in Figure 2.2.

2.2.1 Mode geometry

A steady-state intensity pattern inside the cavity is usually refered to as the resonator mode. A Gaussian beam can only exist inside a cavity, if there is a self consistent solution for $q(z)$ after one round trip within the optical system of the resonator. After this round trip both real and imaginary part have to be equal to their previous value, respectively. This implies that at the mirror positions the radius of curvature of the mode has to match the radius of curvature of the mirrors [1]

$$R(z_{1,2}) = z_{1,2} + \frac{z_0^2}{z_{1,2}} = \mp R_{1,2}. \tag{2.16}$$

These two conditions together with the condition fixed by a given resonator length $L = z_2 - z_1$, provide a system of three equations, which determines the three parameters z_0, z_1, and z_2. If one now introduces the resonator g-parameters $g_{1,2} = 1 - L/R_{1,2}$, the

[1] Since the mirror at z_1 is concave (positiv R_1), the Gaussian mode is converging and has therefore a negative curvature, $-R_1$.

solution is

$$z_0^2 = \frac{g_1 g_2 (1 - g_1 g_2) L^2}{(g_1 + g_2 - 2 g_1 g_2)^2}, \tag{2.17}$$

$$z_1 = -\frac{g_2 (1 - g_1) L}{g_1 + g_2 - 2 g_1 g_2}, \tag{2.18}$$

$$z_2 = \frac{g_1 (1 - g_2) L}{g_1 + g_2 - 2 g_1 g_2}. \tag{2.19}$$

Equations 2.18 and 2.19 determine the relative position of the mode waist, Equation 2.17 determines the waist size. Those are the only free parameters of a Gaussian beam, as discussed in Section 2.1.2, thus the Gaussian resonator mode is completely defined. The cavity mode waist and the beam width at the mirrors can now be expressed in terms of the resonator g-parameters

$$w_0 = \left(\frac{\lambda L}{\pi}\right)^{1/2} \left(\frac{g_1 g_2 (1 - g_1 g_2)}{(g_1 + g_2 - 2 g_1 g_2)^2}\right)^{1/4}, \tag{2.20}$$

$$w_{1,2} = \left(\frac{\lambda L}{\pi}\right)^{1/2} \left(\frac{g_{2,1}}{g_{1,2}(1 - g_1 g_2)}\right)^{1/4}. \tag{2.21}$$

2.2.2 Mode spectrum

To calculate the Eigenfrequencies of the resonator, one has to look at the phase change of the Gaussian mode during one resonator round trip. To keep the cavity field unchanged after a round trip, the relative phase has to be an integer multiple of 2π. Thus the phase change from mirror to mirror has to be an integer multiple of π. Using the expression for the phase along the resonator axis $(x, y = 0)$ from Equation 2.5, this condition becomes

$$k z_1 - \arctan\left(\frac{\lambda z_1}{\pi w_0^2}\right) - k z_2 + \arctan\left(\frac{\lambda z_2}{\pi w_0^2}\right) = j\pi, \qquad j = 0, 1, 2... \tag{2.22}$$

Substituting the resonator conditions from Equations 2.18, 2.19, and 2.20 gives the cavity Eigenvalues of k. They can be translated into a frequency condition using the dispersion relation $\nu = kc/2\pi$

$$\nu_j = \frac{c}{2L}\left(j + \frac{1}{\pi}\arccos\sqrt{g_1 g_2}\right). \tag{2.23}$$

Hence the free spectral range (FSR), which is the frequency spacing between two modes, is given by

$$\nu_{FSR} = \frac{c}{2L}. \tag{2.24}$$

The resonance condition 2.23 allows for two counter-propagating Gaussian modes. The intensity profile, given by the interference between these modes, create the standing wave interference pattern

$$I(x, y, x) = |E(x, y, z) + E^*(x, y, z)|^2 = |E_0|^2 |\psi(x, y, z) + \psi^*(x, y, z)|^2, \tag{2.25}$$

where the mode function $\psi(x, y, z)$ is given by

$$\begin{aligned}\psi(x,y,z) &= \frac{1}{2}\frac{w_0}{w(z)}\frac{\exp\left[ikz - i\varphi(z)\right]}{w(z)} \times \\ &\quad \times \exp\left[-\frac{x^2+y^2}{w^2(z)} - ik\frac{x^2+y^2}{2R(z)}\right]. \end{aligned} \tag{2.26}$$

The normalization is chosen such that the cavity mode volume becomes

$$V_m = \int d^3r \, |\psi(\vec{r})|^2 = \frac{\pi}{4} w_0^2 L, \tag{2.27}$$

which is equal to the volume of a cylinder of diameter w_0 and length L.

2.2.3 Higher-order modes

A more general type of solutions of the paraxial wave equation are the Hermite-Gaussian modes. They are indeed physical solutions of the stable two mirror resonator as well [Sie86].

$$\begin{aligned}\phi(x,y,z) &= \frac{1}{\sqrt{2^{2+n+m} n! m!}} \frac{w_0}{w(z)} \exp\left[ikz - i(m+n+1)\varphi(z)\right] \\ &\quad \times \mathrm{H_m}\left(\sqrt{2}\frac{x}{w(z)}\right) \mathrm{H_n}\left(\sqrt{2}\frac{y}{w(z)}\right) \\ &\quad \times \exp\left[-\frac{x^2+y^2}{w^2(z)} + ik\frac{x^2+y^2}{2R(z)}\right]. \end{aligned} \tag{2.28}$$

H_i is the Hermite polynomial of i-th order. The field amplitude is again normalized to the mode volume V_m as given in Equation 2.27. Since the zero-order Hermite polynomial $H_0(z) = 1$, the zero-order Hermite-Gaussian mode is equivalent to the Gaussian beam mode from Equation 2.26. The transversal intensity distribution of a few higher-order examples can be seen in Figure 2.3.

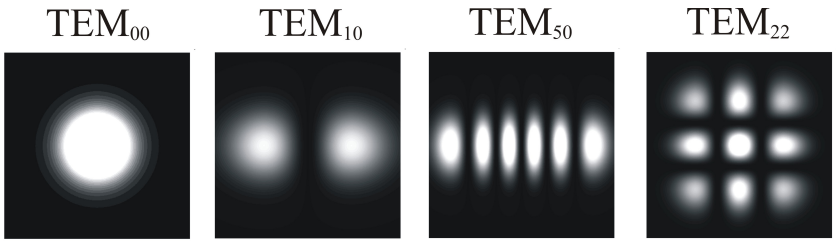

Figure 2.3: Examples for the transversal intensity distribution of Hermite-Gaussian modes. The modes are called TEM, for transversal electromagnetic, and labeled by the indices of the two corresponding Hermite polynomials.

The properties of these higher order modes are the same as for the ground mode regarding waist position (Equation 2.18 and 2.19), waist size (Equation 2.14), and beam width

on the mirrors (Equation 2.21). The resonance frequency condition for the Hermite-Gaussian mode of order m, n changes to

$$\nu_{jmn} = \frac{c}{2L}\left(j + \frac{1}{\pi}(m+n+1)\arccos\sqrt{g_1 g_2}\right), \qquad j,m,n \;\epsilon\; \{0,1,2,...\}\,. \tag{2.29}$$

2.2.4 Resonator quality

A measure for the quality of a resonator is the time light cycles between the mirrors without leaving the resonator. The number of round trips is given by the ratio between time per round trip and the loss rate, which for a cavity of length L and decay rate κ is

$$n_r = \frac{c/2L}{2\kappa}. \tag{2.30}$$

Another figure of merit is the resonator finesse, given by the ratio of its free spectral range and its linewidth (full width at half maximum, FWHM). This can be linked to the number of round trips the following way

$$\mathfrak{F} = \frac{FSR}{\Delta\nu} = \frac{c/2L}{2\kappa/2\pi} = 2\pi n_r. \tag{2.31}$$

In a perfect resonator the losses are caused only by transmission through the mirrors. In this case the loss rate is $\kappa = \kappa_T = cT/2L$, where T is the mirror transmission. The finesse then simply becomes

$$\mathfrak{F} = \frac{\pi}{T}. \tag{2.32}$$

In the experiment, the real cavity decay will have additional contributions which can be accounted for by an additional loss rate, giving a total loss rate

$$\kappa = \kappa_T + \kappa_{lo}. \tag{2.33}$$

The transmitted fraction of the cavity input power is given by (see Section 3.3)

$$P_{\text{out}} = \left(\frac{\kappa_T}{\kappa}\right)^2 P_{\text{in}}. \tag{2.34}$$

2.3 Mode matching

To solve the problem of mode-matching of the incident laser beam to the cavity mode, we can use the ABCD-matrix formalism acting on the complex source point coordinates introduced in Equation 2.8.

2.3.1 ABCD Matrices

As shown in the last section, a Gaussian beam remains a Gaussian beam during its propagation in vacuum. It should now be investigated how optical elements change its properties. Generally, these optical elements can be described by transformations of the form

$$q_b = \frac{Aq_a + B}{Cq_a + D}, \tag{2.35}$$

where

$$\begin{pmatrix} A & B \\ C & D \end{pmatrix} \tag{2.36}$$

is a characteristic matrix for the optical element.
The trivial element, propagation in vacuum, does the following: If the beam parameters, summarized by q, are known in a plane $z = z_a$, in a plane $z = z_b$ they are given at a distance $d = z_b - z_a$ according to Equation 2.12 by

$$q_b = q_a + d. \tag{2.37}$$

The corresponding translation matrix is

$$\begin{pmatrix} A & B \\ C & D \end{pmatrix} = \begin{pmatrix} 1 & d \\ 0 & 1 \end{pmatrix}. \tag{2.38}$$

This is equivalent to the ray matrix used in geometrical optics [Col60], where the propagation of ray vectors is described:

$$\begin{pmatrix} r_b \\ r'_b \end{pmatrix} = \begin{pmatrix} 1 & d \\ 0 & 1 \end{pmatrix} \begin{pmatrix} r_a \\ r'_b \end{pmatrix}. \tag{2.39}$$

The quantities $r_{a,b}$ are the radial displacement from the optical axis and $r'_{a,b}$ are the slope with respect to this axis. It turns out that this is a general conclusion, the ABCD-matrices which transform Gaussian beams are equivalent to the ray matrices in geometrical optics [Sie86].
Beside the translation matrix, other important basic elements are the reflection matrix

$$\begin{pmatrix} A & B \\ C & D \end{pmatrix} = \begin{pmatrix} 1 & 0 \\ -2/R & 1 \end{pmatrix}, \tag{2.40}$$

($R < 0$ for convex, $R > 0$ for concave surfaces) and the refraction matrix

$$\begin{pmatrix} A & B \\ C & D \end{pmatrix} = \begin{pmatrix} 1 & 0 \\ \frac{n_1 - n_2}{n_2 R} & \frac{n_1}{n_2} \end{pmatrix}. \tag{2.41}$$

This matrix formulation allows to decompose complex optical systems into a series of simple elements. The ABCD-matrix describing the whole system, is formed by multiplying the matrices of the basic elements.

A biconcave lens (with refractive index n) is described by the matrix product of a refraction matrix at the convex vacuum-glass interface, a translation matrix within the glass part and another refraction matrix at the concave glass-vacuum interface. For a thin lens, the translation matrix can be neglected and the product of the two refraction matrices remain:

$$\begin{pmatrix} 1 & 0 \\ \frac{n-1}{R_2} & \frac{n}{1} \end{pmatrix} \begin{pmatrix} 1 & 0 \\ \frac{1-n}{nR_1} & \frac{1}{n} \end{pmatrix} = \begin{pmatrix} 1 & 0 \\ -(n-1)\left(\frac{1}{R_1} - \frac{1}{R_1}\right) & 1 \end{pmatrix} = \begin{pmatrix} 1 & 0 \\ -\frac{1}{f} & 1 \end{pmatrix}, \tag{2.42}$$

the non-zero off-diagonal element can be identified as the lens law and thus expressed in terms of the focal length f.

2.3.2 Matching the cavity parameters

The above described formalism can now be used to find the mode matching conditions for coupling a Gaussian beam into a cavity of length L formed by two mirrors with radius of curvature R using a thin lens of focal length f. The incoming laser can be

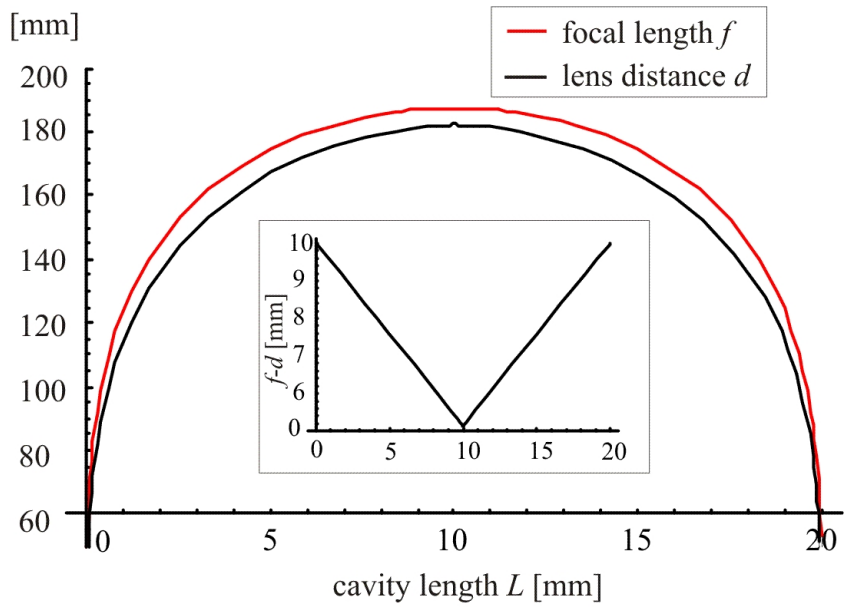

Figure 2.4: The figure shows the solution of the mode matching equations 2.46 and 2.47. The required focal length f (red curve) and the distance d between lens and cavity mirror (black curve) are plotted as a function of the cavity length L.

assumed to be a Gaussian beam with infinite radius of curvature and waist w_{in}

$$q_{in} = -i\frac{\pi w_{in}^2}{\lambda}. \tag{2.43}$$

The optical system to couple into the cavity can be decomposed into a thin lens of focal length f and a free propagation of distance d to the first cavity mirror

$$\begin{pmatrix} A & B \\ C & D \end{pmatrix} = \begin{pmatrix} 1 & d \\ 0 & 1 \end{pmatrix} \times \begin{pmatrix} 1 & 0 \\ -1/f & 1 \end{pmatrix} = \begin{pmatrix} 1-d/f & d \\ -1/f & 1 \end{pmatrix}. \tag{2.44}$$

The q-parameter of the incoming beam is transformed according to Equation 2.35. Equating the real part and the imaginary part separately to the respective cavity parameters yields

$$\Re(q_{out}) = -1/R, \qquad \Im(q_{out}) = \frac{\lambda}{\pi w_1^2}, \tag{2.45}$$

where, as defined previously, R is the cavity mirror radius of curvature (the wave front curvature has to be negative since the incoming beam is converging) and w_1 is the beam width on that mirror. To match the incoming beam to the cavity mode, the required focal length is

$$f = \frac{\pi w_{in}^2}{\lambda}\left[\left(\frac{\pi w_{in} w_1}{R_1 \lambda}\right)^2 + \left(\frac{w_{in}}{w_1}\right)^2 - 1\right]^{-1/2}, \tag{2.46}$$

and the mirror's appropriate distance is

$$d = \begin{cases} \dfrac{\sqrt{\left(\frac{w_{in}}{w_1}\right)^2 + R_1^2\left(\frac{\lambda}{\pi w_1^2}\right)^2\left[\left(\frac{w_{in}}{w_1}\right)^2 - 1\right]} - R_1^2\left(\frac{\lambda}{\pi w_1^2}\right)}{\frac{1}{R_1} + R_1\left(\frac{\lambda}{\pi w_1^2}\right)^2} & : \quad L < R_1, \\ \dfrac{\sqrt{\left(\frac{w_{in}}{w_1}\right)^2 + R_1^2\left(\frac{\lambda}{\pi w_1^2}\right)^2\left[\left(\frac{w_{in}}{w_1}\right)^2 - 1\right]} - 1}{\frac{1}{R_1} + R_1\left(\frac{\lambda}{\pi w_1^2}\right)^2} & : \quad L > R_1. \end{cases} \tag{2.47}$$

Figure 2.4 shows an according graph for the cavity mirrors with $R = 10$mm, as used in the experiment (see Section 4.5). The figure points up two important facts. Firstly, the closer one gets to the point where $L = 2R$ (the concentric point, see Section sec:stabil), the stronger the focussing lens has to be (shorter focal length) and secondly, as shown in the inset, changing the length from the confocal to the concentric point, the position of the pump beam focus changes from the first mirror to the centre of the cavity ($f - d = 10$mm).

2.4 Resonator stability

To find a criterion for the stability of the resonator mode, one can take a deeper look at Equation 2.20. The quantity w_0^4 becomes negative if $g_1 g_2(1 - g_1 g_2) < 0$, so that real and finite solutions can exist only for

$$0 < g_1 g_2 < 1. \tag{2.48}$$

This can be referred to as a stability criterion, since it coincides with the general condition for stable solutions in a resonator formed by two spherical mirrors, as derived by pure ray optics [Sie86, Hoc03]. This criterion is illustrated in the following stability diagram (Figure 2.5), where the hatched areas, are those in which the condition 2.48 is fulfilled.

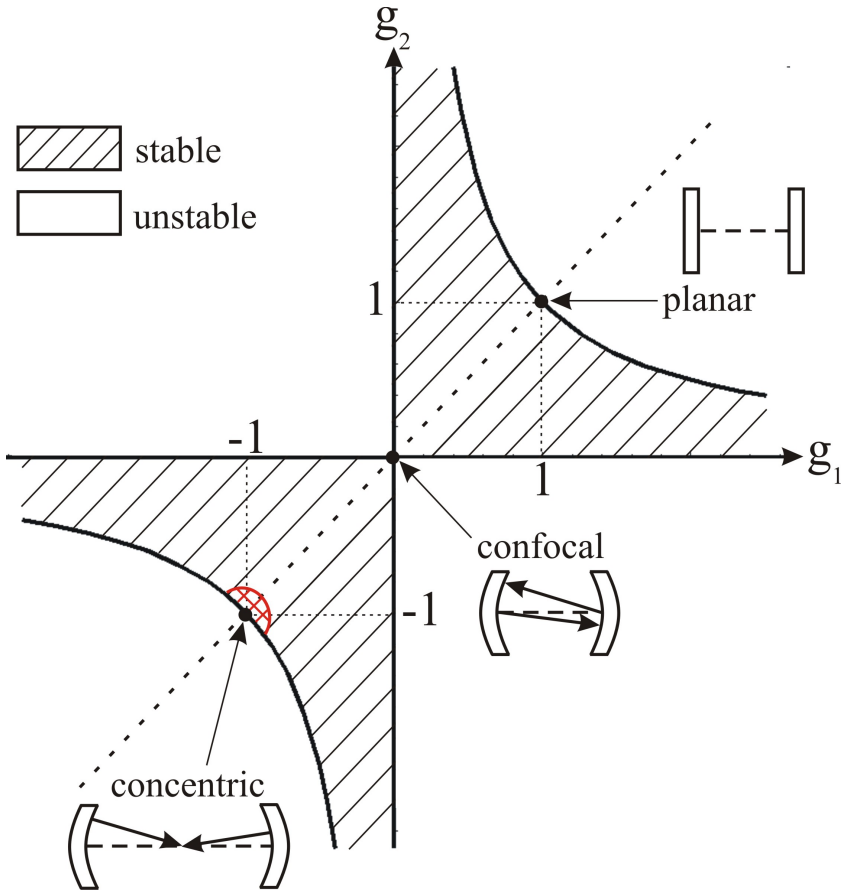

Figure 2.5: The fibre shows the stability diagram for resonators formed by two spherical mirrors. As a function of the two g parameters the stability criterion 2.48 is evaluate. The hatched area shows the region where the cavities are stable. Of special interest is the diagonal line which corresponds to symmetric cavities, and especially the confocal point in the centre and the planar and concentric limits at the edges of the stability region.

Of special interest in this work is the diagonal line in the diagram, which corresponds to symmetric resonators, where both mirror radii are equal. On this line there are three characteristic points, which will be examined in more detail: the confocal point at the centre and the the planar and the concentric limit at the edges of the stability region.

2.4.1 Near-planar resonators

When the radii of curvature of the resonator mirrors are equal and very large

$$R_1 = R_2 = R \gg L \leftrightarrow g_1 = g_2 \approx 1, \tag{2.49}$$

the resonator is called near-planar. It has the property that the beam width is large and almost constant

$$w_0^2 \approx w_1^2 = w_2^2 \approx \frac{L\lambda}{\pi}\sqrt{\frac{R}{2L}}, \tag{2.50}$$

w_0 being the beam waist and $w_{1,2}$ the beam width at the mirrors. Since one aim of this work is to decrease the mode waist as much as possible, the near-planar configuration is not of special interest.

2.4.2 Confocal resonators

A resonator is called confocal if

$$L = R_1 = R_2 = R \leftrightarrow g_1 = g_2 = 0. \tag{2.51}$$

(i.e. the two focal points (at $R/2$) coincide. This is the configuration of highest stability in the sense that it is highly insensitive to misalignment of one or the other mirror. This is due to the fact that the centre of curvature stays at the other mirror surface, when one of mirror is tilted. The Rayleigh length equals half the resonator length, so the beam width at the mirrors is a factor of $\sqrt{2}$ larger than the waist (see also Figure 2.6).

$$w_0^2 = \frac{L\lambda}{2\pi}, \qquad w_1^2 = w_2^2 = \frac{L\lambda}{\pi}. \tag{2.52}$$

Figure 2.6 also shows that small waists are achieved close to the concentric limit. The

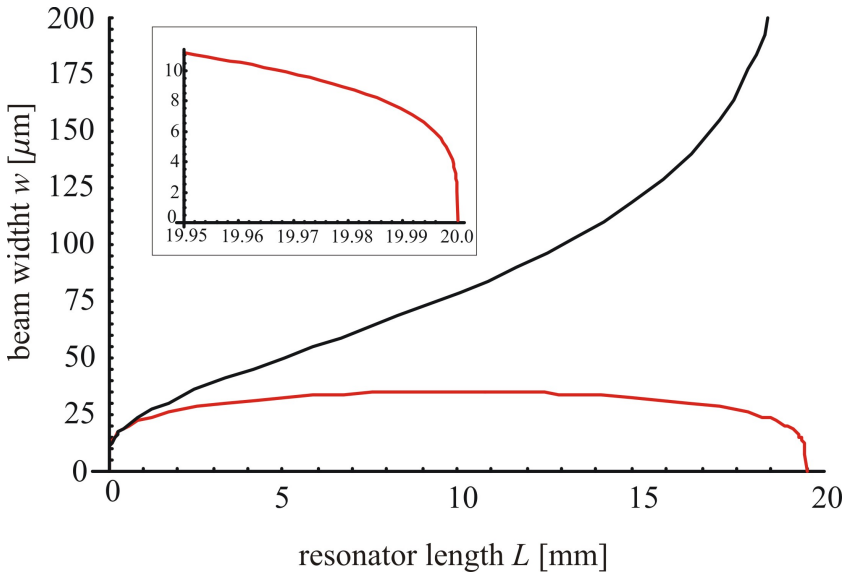

Figure 2.6: The plot shows the mode width at the waist position (red curve) and at the mirrors (black curve) as a function of the resonator length for $R = 10$mm. The inset shows the rapid decrease of the mode waist close to the concentric limit.

limit $L \to 0$ is hard to reach, since finite sized curved mirrors touch each other at some point.

2.4.3 Near-concentric resonators

When the resonator length is only slightly smaller than the the sum of both radii, the resonator is called near-concentric

$$R_1 = R_2 \approx L/2 + \Delta L \leftrightarrow g_1 = g_2 \approx -1 + \Delta L/R, \qquad \Delta L \ll L. \tag{2.53}$$

The beam width at the waist and at the mirrors is given by

$$w_0^2 \approx \frac{L\lambda}{\pi}\sqrt{\frac{\Delta L}{4L}}, \qquad w_{1,2}^2 \approx \frac{L\lambda}{\pi}\sqrt{\frac{4L}{\Delta L}}. \tag{2.54}$$

The waist w_0 and can theoretically be made arbitrarily small. The drawback is that this point is close to the edge of the stability region and the more the concentric point is approached, the more sensitive the cavity becomes. In fact, small mirror misalignment cause larger and larger cavity axis misalignments as illustrated in Figure 2.7. Nevertheless, this is the point at which most of the experiments described in this thesis have been carried out, since it allowed to decrease the mode waist independently of the resonator length. This was necessary in order to combine a mode cross section not much larger than the atomic scattering cross section with a mirror distance which allowed to send a MOT-beam through the cavity (see Chapter 4).

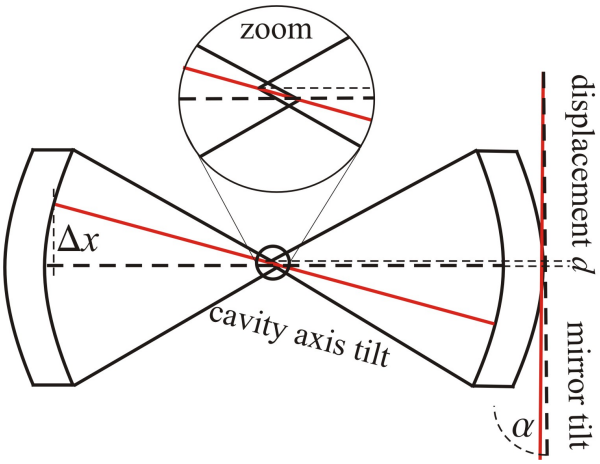

Figure 2.7: The figure shows how small mirror tilts lead to big cavity axis tilts, close to the concentric point.

2.4.4 Stability close to the concentric limit

To quantitatively estimate how far one can approach the concentric limit for a given alignment accuracy, one can calculate the deviation of the mode position from the mirror centre caused by a transversal displacement d of one of the mirrors as shown in Figure 2.7

$$\Delta x = \frac{Rd}{2R - L}, \tag{2.55}$$

or due to a tilt of one of the mirrors by an angle α where $d = R\alpha$ for $\alpha ß 1$

$$\Delta x = \frac{R^2\alpha)}{2R - L}. \tag{2.56}$$

Both terms diverge for $L \to 2R$ as shown in Figure 2.8. In the figure both mirrors have a radius of curvature of $R = 10$mm, so that the concentric point is at $L = 20$mm. The angular displacement is translated into a lateral misalignment of one of the micrometer screws , controlling the mirror mount (at a distance of 4.5mm from the centre) (see Figure 4.10). An axial misalignment of 1μm by one of the crews causes a mirror tilt of 0.013°. The graph shows, as an example, the mode spot displacement on the cavity mirrors for a transversal displacement of $d = 1\mu$m (black curve) or a longitudinal displacement of one screw (red curve) by $d = 1\mu$m. It can be seen from the curves that this accuracy would not allow to extend the length to more than 19.99mm, since the mode would start to leave the mirrors (which are of 6mm diameter).

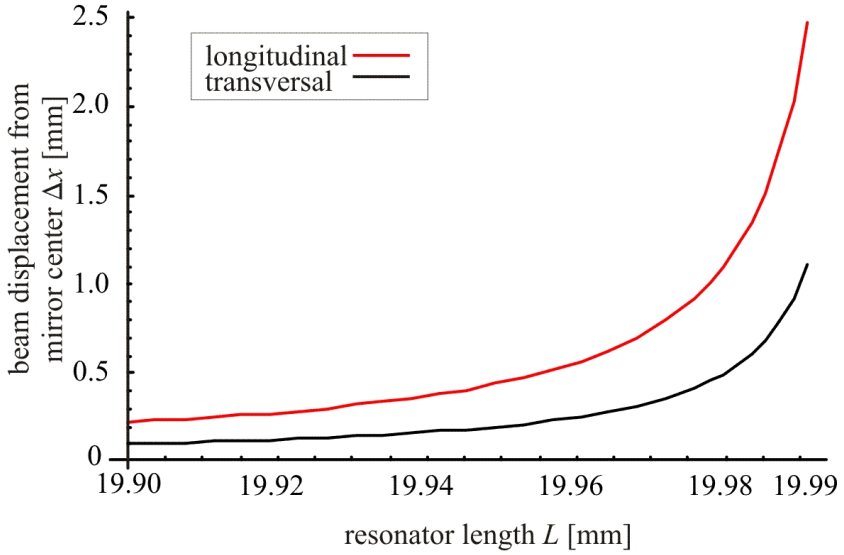

Figure 2.8: The figure quantifies the misalignment of the optical axis caused by small mirror misalignments, depending on how close to the concentric point at 20mm the cavity is. Here Δx denotes the displacement of the mode from the mirror centre, caused by a transversal displacement $d = 1\mu$m (black curve), or an axial displacement $d = 1\mu$m of one of the micrometer screws (which leads to a mirror tilt of 0.013°).

All this shows that in a realistic experiment with a near-concentric resonator, the mode waist can not be decreased arbitrarily. Since below a certain distance to the concentric point, the required stability becomes impossible to realize. But there is a way to overcome this problem. In optical fibres the light is focussed much stronger which should allow to build resonators with a much stronger coupling. One possible setup will be desribed in the next section.

2.5 Fibre gap cavity

A microsciopic cavity formed by two optical fibres has two advantages, beside the small beam waist, it can be relatively easy integrated on an atom chip surface. A possible setup is depicted in Figure 2.9. The resonator of length is formed by two mirrors implanted into optical fibres at a distance $L/2$ from the fibre endface. Between the two fibres a small gap of size d is left. The atoms to be detected are guided through this gap by magnetic potentials created by a current carrying wire (see section 4.4). As shown in

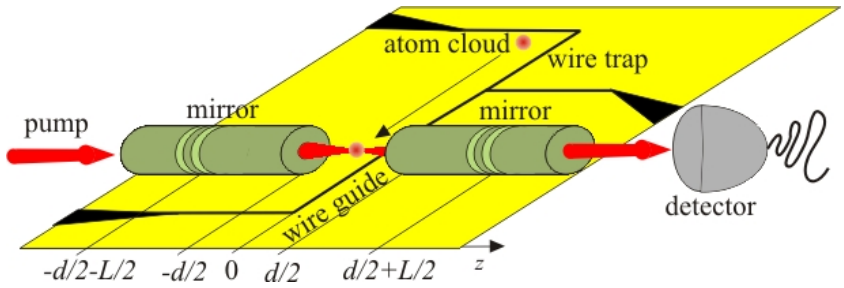

Figure 2.9: Schematics of a possible cavity geometry. The cavity mirrors are implanted into a fibre, the atoms are interacting withe the mode in a μm-wide gap

Figure 2.9, the cavity mirrors are not formed by the fibre endfaces, but are implanted into the fibre, which has the technical reason that cavity length tuning can now be done by simply stretching one of the fibre, while the fibre ends are robustly fixed to the chip surface (see Section 4.8.4). For this configuration the cavity parameters will now be calculated.

2.5.1 Cavity modes

The mode volume has to be split into 3 sections, the two fibre arms and the gap. The electric fields in these sections can be expressed by a polarization vector $\vec{e}_0$, amplitudes $E_\pm$, and mode functions $f_\pm(\vec{r})$, where the index + denotes modes traveling to the right, − denotes modes traveling to the left.

$$\vec{E(r)} = \vec{e_0} \times \begin{cases} E_{1+}f_{1+}(\vec{r}) + E_{1-}f_{1-}(\vec{x}) & \text{for } z < -d/2, \\ E_{2+}f_{2+}(\vec{r}) + E_{2-}f_{2-}(\vec{x}) & \text{for } |z| < d/2, \\ E_{3+}f_{3+}(\vec{r}) + E_{3-}f_{3-}(\vec{x}) & \text{for } z > d/2. \end{cases} \tag{2.57}$$

Since this geometry is radially symmetric with respect to the optical axis, cylindrical coordinates $\vec{r} = (r, \phi, z)$ are going to be used.
The transverse profile of the fibre mode functions is Gaussian, axially these functions are plane waves

$$f_{1\pm}(\vec{r}) = e^{-r^2/w_0^2} e^{\pm ik_1(z+d/2)}, \tag{2.58}$$

$$f_{3\pm}(\vec{r}) = e^{-r^2/w_0^2} e^{\pm ik_1(z-d/2)}. \tag{2.59}$$

They emerge into Gaussian beams in the gap

$$\begin{aligned} f_{2+}(\vec{x}) &= \frac{w_0}{w(z+d/2)} \exp\left[-\frac{r^2}{w^2(z+d/2)}\right. \\ &\quad \left. +ik_0\frac{r^2}{2R(z+d/2)} + ik_0(z+d/2) - i\varphi(z+d/2)\right], \end{aligned} \tag{2.60}$$

$$\begin{aligned} f_{2-}(\vec{x}) &= \frac{w_0}{w(z-d/2)} \exp\left[-\frac{r^2}{w^2(z-d/2)}\right. \\ &\quad \left. -ik_0\frac{r^2}{2R(z-d/2)} - ik_0(z-d/2) + i\varphi(z-d/2)\right]. \end{aligned} \tag{2.61}$$

The usual Gaussian beam parameters are beam width $w(z)$, radius of curvature $R(z)$, Guoy phase $\varphi(z)$, and Rayleigh length z_0, as introduced in Section 2.1. The parameters k_0, k_1 are the longitudinal wave numbers in vacuum and in the fibre, respectively. $\lambda_{0,1} = \frac{2\pi}{k_{0,1}}$ are the corresponding wavelengths.
The mode inside the fibre is emerging into an expanding Gaussian beam in the gap. Because of this divergence, the beam does not exactly match the fibre modes on the other end of the gap. To calculate the corresponding losses, the gap modes are projected onto the fibre mode at the fibre surface

$$\begin{aligned} f_{2-}(r, z=-d/2) &= Q f^*_{2+}(r, z=-d/2) + f^{\perp}_{2-}(r, z=-d/2), \\ f_{2+}(r, z=d/2) &= Q f^*_{2-}(r, z=d/2) + f^{\perp}_{2+}(r, z=d/2), \end{aligned} \tag{2.62}$$

where Q denotes the mode matched fraction of the amplitude, $f^*_{2\pm}$ are the complex-conjugate mode functions, while $f^{\perp}$ denotes the field orthogonal to the fibre mode, which is lost from the cavity. One finds

$$Q = |Q|e^{i\phi} = \frac{w_0}{w(d/2)} e^{ik_0 d - i\phi(d/2)}. \tag{2.63}$$

The leading term of the phase expansion of Q is linear in $d/2z_0$ since

$$\phi\left(\frac{d}{2}\right) = \arctan\left(\frac{d}{2z_0}\right) \approx \frac{d}{2z_0} + \mathcal{O}\left(\frac{d}{2z_0}\right)^3, \tag{2.64}$$

while the amplitude's leading term is quadratic:

$$\frac{w_0}{w\left(\frac{d}{2}\right)} = \frac{1}{\sqrt{1+\left(\frac{d}{2}\right)^2}} \approx 1 - \left(\frac{d}{2}\right)^2 + \mathcal{O}\left(\frac{d}{2z_0}\right)^4. \tag{2.65}$$

If one calculates the cavity modes in perturbation theory in $d/2z_0$, first order terms can be used to calculate the boundary conditions, which determine the cavity resonance frequency. Second order terms can then be used to calculate the losses due to the mode mismatch.

The boundary conditions at the mirror and the continuity equations at the fibre-vacuum interfaces lead to the following cavity resonance condition

$$\frac{d}{2}\left(2k_0 - \frac{1}{z_0}\right) = m\pi - 2\arctan\left[\frac{1}{n}\tan\left(k_1\frac{L}{2}\right)\right], \tag{2.66}$$

where m is an integer number and $n = k_1/k_0$ is the refractive index of the fibre. For the electric field amplitudes the following relations are obtained:

$$|E_{1+}| = |E_{1-}| = |E_{3+}| = |E_{3-}|, \tag{2.67}$$

$$|E_{2+}| = |E_{2-}| = |E_{1+}|\left|\frac{1+n-(1-n)e^{-ik_1L}}{2}\right|. \tag{2.68}$$

2.5.2 Cavity parameters

To calculate the cavity loss rate and the atom-cavity coupling strength, let us look first at the energy flux through the cavity. The energy flux density is given by the Pointing vector $\vec{S} = \vec{E} \times \vec{H}$. The energy flux is its z-component times the mode cross section

$$S_z = \frac{\pi}{4} w_0^2 c\epsilon_0 |E_{2+}|^2. \tag{2.69}$$

This leads to a energy loss per round trip in the cavity of

$$S_{loss} = 2S_z(1 - |Q|^2). \tag{2.70}$$

The total energy stored in every cavity mode is given by the energy density $\varepsilon = \frac{1}{2}(ED + HB) = \epsilon\epsilon_0|E|^2$ times the mode volume $V_m = Lw_0^2\pi/4$ (neglecting the small part stored in the gap):

$$W = 2n^2\epsilon_0|E_{1+}|\frac{\pi}{4}w_0^2 L. \tag{2.71}$$

Beside the decay rate through the mirror κ_T, the cavity loss rate is given by the ratio between energy loss S_{loss} and energy stored in both modes W, which, using Equation 2.68, becomes

$$2\kappa_{gap} = \frac{c}{L}\left(\frac{d}{z_0}\right)^2\left|\frac{1+n-(1-n)e^{-ik_1L}}{4n}\right|^2. \tag{2.72}$$

In the experiment additional losses due to imperfect materials and surfaces will be unavoidable, so the total cavity decay rate per round trip[2] will be given by

$$2\kappa = 2\kappa_T + 2\kappa_{gap} + 2\kappa_{add}. \tag{2.73}$$

The coupling constant between atom and cavity field will be derived in detail in the next chapter in Section 3.2.5. However, we can anticipate the results and write it here

[2]The quantity 2κ corresponds to the loss rate per full round trip ($2L$), measured by $2\pi \times$ FWHM

in terms of the cavity parameters. From Equation 3.38 using the cavity field in the gap (on axis) one finds

$$g = \frac{d_{10}E_0}{\hbar} = \left|1 + n - (1-n)e^{-ik_1 L}\right| \sqrt{\frac{3\Gamma c}{n^2 L w_0^2 k_0^2}}, \tag{2.74}$$

where d_{10} is the electric dipole matrix element given by Equation 3.37, E_0 is the field amplitude. The cooperativity parameter (see Equation 3.32) then becomes

$$\frac{g^2}{\kappa\gamma} = \frac{48}{w_0^2 k_0^2}\left(\frac{T}{\left|1 + n - (1-n)\exp(-ik_1 L)\right|^2} + \left(\frac{d}{z_0}\right)^2\right)^{-1}, \tag{2.75}$$

where the prefactor $\frac{48}{w_0^2 k_0^2}$ is nothing but the ratio between atomic scattering cross section σ and cavity mode cross section $A = w_0^2\pi/4$. It is independent of the cavity length, which is important, since this allows to arbitrarily choose the cavity length, without diminishing the coupling to the atoms. The first term in the brackets arises due to the fact that boundary conditions have to be matched at the mirrors and at the fibre endfaces. It contains L but it shows an oscillating behavior with a period λ/n and can thus be tuned to a maximum value by properly aligning fibre length and gap size.
Finally these quantities shell be filled with life. Cavity parameters will be estimated which are feasible to reach under realistic conditions in the fabrication process and in the experiment. If one assumes that the gap has to be at least 5μm wide, to be able to send atoms through there without too much disturbance from the side walls, one finds the following possible parameters

Cavity length L	20.8 mm	Mode waist w_0	2.92 μm
Fibre ind. of refra. n	1.5	FSR	$2\pi \times 7.2$ GHz
Gap size d	5.08 μm	Gap loss κ_{gap}	$2\pi \times 6.3$ MHz
Mirror transm. T	0.004	Transm. rate κ_T	$2\pi \times 3.1$ MHz
Finesse $\mathfrak{F}$	390	Coupling const. g	$2\pi \times 12.3$ MHz

This cavity would than have a single-atom cooperativity parameter of

$$\frac{g^2}{\kappa\gamma} = 5.3, \tag{2.76}$$

which is already above one and thus on the way into the strong coupling regime (see Section 3.2.4).

3 Theory of atom-light interaction in a cavity

In this chapter the basic theory of the interaction of a classical light field with a two level atom will be derived. Section 3.1 presents rough estimates, which shows the important parameters governing the atom-light coupling. In Section 3.2 a semi-classical model for the coupled system is developed and the enhancement of this coupling in a resonator is discussed. Based on this model, the feasibility of using these resonators as single atom detectors is discussed in Section 3.3 in the case of resonant pumping. In Section 3.4 non-resonant atom detection strategies are considered in the context of non-demolition measurements. Finally, in Section 3.5 the validity limit of the model in the case of more than one atom in the resonator is determined.

3.1 Simple Model

To enhance the atom-light interaction for the purpose of single atom detection, there are two main strategies. The first is to focus the beam down to a cross section of the order of the atomic scattering cross section. The second to enhance the interaction time.
For the first strategy, the signal-to-noise ratio can be estimated using a very simple model. The incoming light is assumed to be in a coherent state with amplitude α_0, $N_0 = |\alpha_0|^2$ is the mean photon number per unit time. If this number is below the saturation limit, in a measurement interval τ N_0 will be changed due to scattering by an atom by

$$\Delta N = N_0 - N = N_0 \frac{\sigma_A}{A}. \tag{3.1}$$

The ratio $\frac{\sigma_A}{A}$ of the resonant free space atomic scattering cross section $\sigma_A = \frac{3\lambda^2}{2\pi}$ [Jac99] and the beam cross section A determines the fraction of the incoming photon number being scattered by the atom. If one measures this change in photon number, the outcome will be limited by the shot noise level $\sqrt{N}$, so the signal-to-noise ratio is given by

$$S = \frac{\Delta N}{\sqrt{N}} \cong \sqrt{N_0} \frac{\sigma_a}{A}, \tag{3.2}$$

which increases, with decreasing A. Note that this ratio cannot be maximized arbitrarily, because if σ_a becomes comparable to the beam cross section A, the paraxial and dipole approximations (see Section sec:parax), on which this expression is based, break down [vEnk00, vEnk01, Dom02, vEnk04].

The second strategy to enhance the atom-light coupling, namely increasing the interaction time, can be realized by increasing the number of transits of every photon through the interaction region by installing cavity mirrors around it. The mean scattered photon number inside the cavity is then enhanced by the number of round trips in the cavity

$$\Delta N_{\mathrm{cav}} = N n_r, \tag{3.3}$$

which increases the signal-to-noise ratio to

$$S_{\mathrm{cav}} = n_r \sqrt{N_0} \frac{\sigma_A}{A}. \tag{3.4}$$

The number of round trips is represented by the figure of merit for the quality of a cavity, its finesse, which is given by $\mathcal{F} = 2\pi n_{\mathrm{rt}}$ (see Section 2.2.4).
The goal is now to find a combination of these two enhancement factors, which leads to a single-atom signal-to-noise ratio > 1 and is experimentally realizable. To justify this very naive approach to single atom detection, the mechanisms of atom-light interaction will be examined in a more profund way.

3.2 Model of the coupled system atom-cavity

3.2.1 Quantum mechanical prerequisites

In the following, the light will be treated quasi-classically. Thus a coherent state is assumed at all times. This is the state with the minimum uncertainty in both phase space variables amplitude and phase, The photon number state expansion of the coherent state is

$$|\alpha\rangle = \exp\left(-\frac{1}{2}|\alpha|^2\right) \sum_{n=0}^{\infty} \frac{\alpha^n}{\sqrt{n!}} |n\rangle. \tag{3.5}$$

It is an Eigenstate of the photon annihilation operator a, thus

$$a|\alpha\rangle = \alpha|\alpha\rangle, \qquad \langle\alpha|a^\dagger = \langle\alpha|\alpha^*, \tag{3.6}$$

where the Eigenvalues are the coherent state amplitudes, from which the average photon number can be directly computed

$$N = |\alpha|^2 = \langle\alpha|a^\dagger a|\alpha\rangle. \tag{3.7}$$

In the following, the commutation relation of the photon creation and annihilation operators will be of importance

$$\left[a, a^\dagger\right] = 1. \tag{3.8}$$

The atoms are treated as two level systems with ground state $|0\rangle$ and excited state $|1\rangle$. The raising $\sigma^+ = |1\rangle\langle 0|$ and lowering operators $\sigma^- = |0\rangle\langle 1|$ interchange between these states

$$\sigma^+|0\rangle = |1\rangle, \qquad \sigma^-|1\rangle = |0\rangle. \tag{3.9}$$

The Hilbert space of the total system is given by the product of the Hilbert space of the the atom and that of the radiation field. The atomic state and the state of the radiation field are described by the reduced density operators ρ^{A} and ρ^{R}. The density matrix of the total system is $\rho = \rho^{\mathrm{A}} \otimes \rho^{\mathrm{R}}$. Given ρ, the reduced density matrices are obtained by partially tracing out the other subsystem, e.g. for the atomic state

$$\rho^{\mathrm{A}} = \mathrm{Tr}_{\mathrm{R}}(\rho), \tag{3.10}$$

or in terms of matrix elements

$$\rho^{\mathrm{A}}_{ab} = \langle a|\rho^{\mathrm{A}}|b\rangle = \sum_{\alpha}\langle a,\alpha|\rho|b,\alpha\rangle = \sum_{\alpha}\rho_{a\alpha b\alpha}. \tag{3.11}$$

3.2.2 Hamiltonian

The coupled atom-cavity system will be described by the parameters depicted in Figure 3.1. The single-mode cavity of resonance frequency ω_{c} is pumped with light of frequency ω at a pumping rate η. The cavity decay rate κ accounts for the coupling to a reservoir. The atom will be modeled by a two level system with a transition frequency ω_{a} and an excited state decay rate Γ. It is coupled to the cavity mode with the single-photon Rabi frequency $g(\vec{r})$. Its position dependence is given by the mode shape.

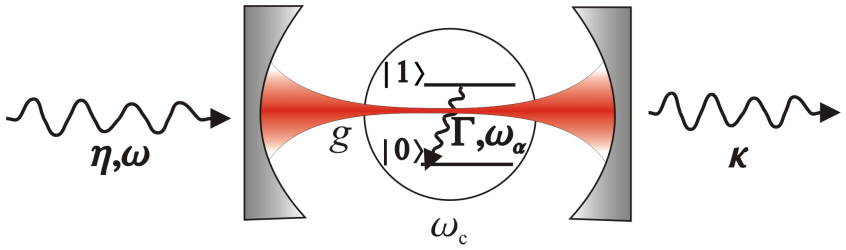

Figure 3.1: Atom-cavity coupling model: ω is the pumping frequency, η the pump rate, ω_c the cavity resonance frequency, κ the cavity mode decay rate, ω_a the atomic resonance frequency, Γ the decay rate of the atomic excited state, and g the coupling constant.

In a frame rotating with pumping frequency ω the Hamlitonian looks as follows:

$$H = \underbrace{-\hbar\Delta_a\sigma^+\sigma^-}_{\text{atom}} \underbrace{-\hbar\Delta_c a^\dagger a}_{\text{cavity field}} \underbrace{-i\hbar\eta\left(a-a^\dagger\right)}_{\text{pump field}} \underbrace{-i\hbar g\left(a^\dagger\sigma^- - \sigma^+ a\right)}_{\text{interaction}}, \tag{3.12}$$

where $\Delta_{\mathrm{c}} = \omega - \omega_{\mathrm{c}}, \Delta_{\mathrm{a}} = \omega - \omega_{\mathrm{a}}$. A Liouvillian damping term describes the damping of the cavity with the decay rate κ and the damping of the atomic system with a spontaneous emmission rate Γ

$$\mathcal{L}\rho = -\kappa\left(\{a^\dagger a,\rho\}_+ - 2a\rho a^\dagger\right) - \Gamma\left(\{\sigma^+\sigma^-,\rho\}_+ - 2\sigma^-\rho\sigma^+\right). \tag{3.13}$$

Throughout this work these decay rates denote 2π times half the width at half maximum of the resonance lines.

This leads to the full quantum master equation

$$\dot{\rho} = -\frac{i}{\hbar}\left[H, \rho\right] + \mathcal{L}\rho. \tag{3.14}$$

Expanded in terms of a and ρ the maser equation becomes

$$\begin{aligned}\dot{\rho} = {} & i\Delta_c\left(a^\dagger a\rho - \rho a^\dagger a\right) + i\Delta_a\left(\sigma^+\sigma^-\rho - \rho\sigma^+\sigma^-\right) - \\ & -g\left(a^\dagger\sigma^-\rho - \rho a^\dagger\sigma^- - a\sigma^+\rho - \rho a\sigma^+\right) - \eta\left(a\rho - \rho a - a^\dagger\rho + \rho a^\dagger\right) - \\ & -\kappa\left(a^\dagger a\rho + \rho a^\dagger a - 2a\rho a^\dagger\right) - \Gamma\left(\sigma^+\sigma^-\rho + \rho\sigma^+\sigma^- - 2\sigma^-\rho\sigma^+\right).\end{aligned} \tag{3.15}$$

3.2.3 Equations of Motion

To convert the master equation 3.15 into an equivalent set of partial differential equations, the matrix elements of the atomic density operator have to be calculated by computing the partial trace (Equation 3.11) and using the commutation relation in Equation 3.8. This generates three equations of motion for the atom

$$\frac{\partial}{\partial t}\rho_{00}^A = 2\Gamma\rho_{11}^A - g\left(\alpha^*\rho_{10}^A + \alpha\rho_{01}^A\right), \tag{3.16}$$

$$\frac{\partial}{\partial t}\rho_{11}^A = -2\Gamma\rho_{11}^A + g\left(\alpha^*\rho_{10}^A + \alpha\rho_{01}^A\right), \tag{3.17}$$

$$\frac{\partial}{\partial t}\rho_{01}^A = \left(-\Gamma - i\Delta_a\right)\rho_{01}^A + g\alpha^*\left(\rho_{00}^A - \rho_{11}^A\right). \tag{3.18}$$

The equation of motion for the field is derived from

$$\alpha = \langle a\rangle = \mathrm{Tr}\left(\rho a\right) \tag{3.19}$$

and thus

$$\dot{\alpha} = frac\partial\partial t\langle a\rangle = \frac{\partial}{\partial t}\mathrm{Tr}\left(\rho a\right) = \mathrm{Tr}\left(\dot{\rho}a\right). \tag{3.20}$$

By substituting into the master equation 3.15 one obtains

$$\begin{aligned}\dot{\alpha} = {} & i\Delta_c\mathrm{Tr}\left(aa^\dagger\rho^R a\otimes\rho^{\mathrm{A}} - \rho^{\mathrm{A}}\otimes\rho^{\mathrm{R}}a^\dagger aa\right) + \\ & i\Delta_a\mathrm{Tr}\left(\sigma^+\sigma^-\rho^{\mathrm{A}}\otimes\rho^{\mathrm{R}}a - \rho^{\mathrm{A}}\sigma^+\sigma^-\otimes\rho^{\mathrm{R}}a\right) - \\ & -ig\mathrm{Tr}\left(\sigma^+\rho^{\mathrm{A}}\otimes a\rho^{\mathrm{R}}a - \rho^{\mathrm{A}}\sigma^+\otimes\rho^{\mathrm{R}}aa + a^\dagger\rho^{\mathrm{R}}a\otimes\sigma^-\rho^{\mathrm{A}} + \rho^{\mathrm{R}}a^\dagger a\otimes\rho^{\mathrm{A}}\sigma^-\right) - \\ & -\eta\mathrm{Tr}\left(a\rho^{\mathrm{R}}a\otimes\rho^{\mathrm{A}} - \rho^{\mathrm{R}}aa\otimes\rho^{\mathrm{A}} - a^\dagger\rho^{\mathrm{R}}a\otimes\rho^{\mathrm{A}} + \rho^{\mathrm{R}}a^\dagger a\otimes\rho^{\mathrm{A}}\right) - \\ & -\kappa\mathrm{Tr}\left(a^\dagger a\rho^{\mathrm{R}}a\otimes\rho^{\mathrm{A}} + \rho^{\mathrm{A}}\otimes\rho^{\mathrm{R}}a^\dagger aa - 2a\rho^{\mathrm{R}}a^\dagger a\otimes\rho^{\mathrm{A}}\right) - \\ & -\Gamma\mathrm{Tr}\left(\sigma^+\sigma^-\rho^{\mathrm{A}}\otimes\rho^{\mathrm{R}}a + \rho^{\mathrm{R}}a\otimes\rho^{\mathrm{A}}\sigma^+\sigma^- - 2\sigma^-\rho^{\mathrm{A}}\sigma^+\otimes\rho^{\mathrm{R}}a\right).\end{aligned} \tag{3.21}$$

The trace over both subspaces can be decomposed into the partial traces

$$\mathrm{Tr}\left(O\right) = \mathrm{Tr}^{\mathrm{A}}\left[\mathrm{Tr}^{\mathrm{R}}\left(O_{\mathrm{A}}\otimes O_{\mathrm{R}}\right)\right] = \mathrm{Tr}^{\mathrm{A}}\left(O_{\mathrm{A}}\right)\mathrm{Tr}^{\mathrm{R}}\left(O_{\mathrm{R}}\right). \tag{3.22}$$

By making use of the invariance of the trace under cyclic permutations and the commutation relation for the photonic operators, one finds

$$\dot{\alpha} = (i\Delta_c - \kappa)\,\alpha - g\rho_{10}^{\mathrm{A}} + \eta. \tag{3.23}$$

From now on, the superscript A will be suppressed and the atomic matrix elements will be denoted by ρ_{ij} with $i, j \epsilon \{0, 1\}$.

3.2.4 Solutions

The stationary solutions of the above equations of motion can be determined by setting the temporal derivatives to zero. For the atomic coherence one finds

$$\rho_{10} = \frac{g\alpha\,(\rho_{00} - \rho_{11})}{\Gamma - i\Delta_a}. \tag{3.24}$$

Substituting this into Equation 3.17 and using the normalization of the atomic populations $\rho_{00} + \rho_{11} = 1$, one finds

$$\rho_{11} = \frac{g^2 N}{\Gamma^2 + \Delta_a^2 + 2g^2 N}, \tag{3.25}$$

where $N = |\alpha|^2$ is the average intra-cavity photon number.
To determine the influence of the atom-light interaction on the radiation field amplitude, one first inserts the solution for ρ_{11} into Equation 3.24 and obtains

$$g\rho_{10} = \frac{\Gamma + i\Delta_a}{\Gamma^2 + \Delta_a^2 + 2g^2 N} g^2 \alpha =: (\gamma + iU)\alpha, \tag{3.26}$$

where

$$\gamma := \frac{g^2 \Gamma}{\Gamma^2 + \Delta_a^2 + 2g^2 N} \tag{3.27}$$

and

$$U := \frac{g^2 \Delta_a}{\Gamma^2 + \Delta_a^2 + 2g^2 N}. \tag{3.28}$$

The stationary solution for the light amplitude, obtained from Equation 3.23, then becomes

$$\alpha = \frac{\eta}{(\kappa + \gamma) - i\,(\Delta_c - U)}. \tag{3.29}$$

Now the physical meaning of the newly introduced terms becomes obvious: γ, being added to the real part of the cavity field, is an additional decay rate due to spontaneous scattering and therefore proportional to the atomic decay constant, while U adds to the imaginary part and thus represents an additional phase shift, due to coherent scattering. It is proportional to the detuning between light and atomic frequency.
This results in an averaged intra-cavity photon number

$$N = |\alpha|^2 = \frac{\eta^2}{(\kappa + \gamma)^2 + (\Delta_c - U)^2}. \tag{3.30}$$

It should be noted that this expression is only an implicit solution for the photon number since γ and U still contain N. But an explicit solution can be easily obtained by standard numerical methods. In the limit of low atomic saturation ($2Ng^2 \ll \Gamma^2$), the photon number is

$$N = \eta^2 \left[\left(\kappa + \frac{g^2\Gamma}{\Gamma^2 + \Delta_a^2} \right)^2 + \left(\Delta_c - \frac{g^2\Delta_a}{\Gamma^2 + \Delta_a^2} \right)^2 \right]^{-1}. \tag{3.31}$$

To quantify the the atom-cavity coupling strength, one has to look for the condition when the atom induced effects become important. This is the case when the coupling constant g becomes larger than the cavity decay rate κ and bigger than the atomic decay rate Γ. These conditions are combined in the definition of the cooperativity parameter $\frac{g^2}{\kappa\Gamma}$ [Ber94]. Depending on this parameter being smaller or bigger than one, one speaks of the weak or strong coupling regime

$$\begin{aligned} \frac{g^2}{\kappa\Gamma} &\ll 1 \quad \rightarrow \quad \text{weak coupling regime,} \\ \frac{g^2}{\kappa\Gamma} &\gg 1 \quad \rightarrow \quad \text{strong coupling regime.} \end{aligned} \tag{3.32}$$

This parameter will be used throughout this whole chapter to describe the coupling strength and, as will be shown later in Section 3.3.1, it is a direct measure for the single-atom detection feasibility of a cavity.

3.2.5 Refined model

Before discussing detection strategies, the parameters of the developed atom-cavity model have to be defined more precisely. As depicted in Figure 3.2 the cavity length is

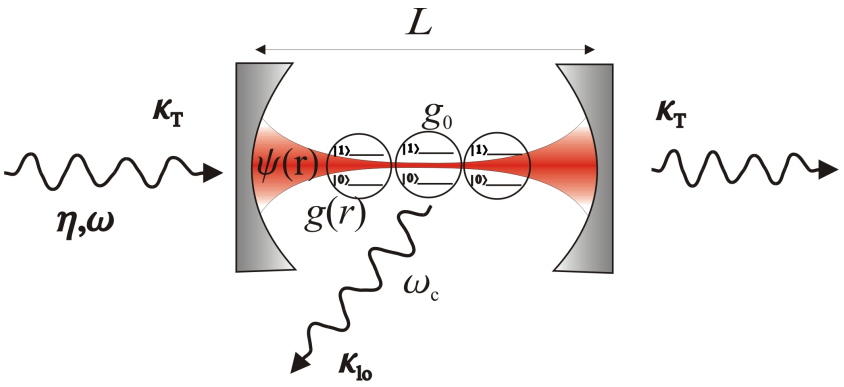

Figure 3.2: The cavity length is L, its decay rate given by the transmission rates through the mirrors κ_T and the scattering rate into other modes κ_{lo}. The coupling constant $g(\vec{r})$ is position dependent. It is given by a maximum value g_0 times the mode function $\psi(\vec{r})$

denoted by L, its decay rate $\kappa = \kappa_T + \kappa_{\text{lo}}$ is given by the transmission rate through the mirrors $\kappa_T = \frac{cT}{2L}$ (where T is the mirror transmission) and the loss rate into other modes

κ_{lo}. The number of transmitted photons N_{out} can be related to the average photon number inside the cavity N, and the cavity pump rate η can be related to the incident laser power j_{in}

$$N_{\mathrm{out}} = N\kappa_T\tau \quad \text{and} \quad \eta = \sqrt{j_{\mathrm{in}}\kappa_T}. \tag{3.33}$$

The electric field in the cavity is position dependent, which can be expressed by the mode function $\psi(\vec{r})$ which for the two counter-propagating modes yields $\vec{E}(\vec{r}) = \vec{E}_0\,[\psi(\vec{r}) + \psi(\vec{r})^*]$. The integral over this mode function gives cavity mode volume (see Equation 2.27)

$$V_m = \int d^3r\,|\psi(\vec{r})|^2. \tag{3.34}$$

The atom couples to the field of a cavity mode by the electric dipole transition and the coupling constant therefore has the same position dependence as the mode field

$$g(\vec{r}) = \frac{\vec{d}_{10}\cdot\vec{E}_0\psi(\vec{r})}{\hbar} = g_0\psi(\vec{r}). \tag{3.35}$$

The electric field strength per photon in the cavity can be calculated from the total energy in the cavity

$$\varepsilon = \hbar\omega = \int d^3r\epsilon_0|\vec{E}(\vec{r})|^2 = \epsilon_0 2|\vec{E}_0|^2V_m \;\Rightarrow\; |\vec{E}_0| = \sqrt{\frac{\hbar\omega}{2\epsilon_0 V_m}}. \tag{3.36}$$

From Fermi's golden rule an expression for the electric dipole transition matrix element can be found

$$\Gamma = \frac{\gamma^3}{6\pi\hbar c^3}\frac{|d_{10}|^2}{\epsilon_0} \Rightarrow d_{10} = \sqrt{\frac{6\pi\epsilon_0\hbar c^3\Gamma}{\omega^3}}, \tag{3.37}$$

so the maximum coupling constant becomes

$$g_0 = \frac{\vec{d}_{10}\vec{E}_0}{\hbar} = \sqrt{\frac{d_{01}^2\omega}{2\hbar\epsilon_0 V_m}} = \sqrt{\frac{3\Gamma c\lambda^2}{4\pi V_m}}. \tag{3.38}$$

If now the mode volume is expressed by the mode cross section A times cavity length L and the the resonant atomic scattering cross section $\sigma_a = \frac{3\lambda^2}{2\pi}$ is introduced, one finds

$$g_0^2 = \frac{\sigma_a}{A}\Gamma\frac{c}{2L}, \tag{3.39}$$

which shows that the coupling strength can be decomposed into the scattering probability $\frac{\sigma}{A}$ (see Equation 3.1) times the atomic decay rate Γ divided by the cavity round trip time $\frac{2L}{c}$.
In the following, the coupled atom-cavity model will be used to predict for the feasibility of detecting the presence of a single atom in the cavity mode by measuring the cavity transmission signal, especially for miniaturized cavities as described in Section 2.5.

3.3 Resonant atom detection

The strategies to detect a single atom based on its interaction with the cavity mode rely on the two effects the atom has on the cavity field (see Equations 3.27 and 3.28). These are the enhanced decay rate due to spontaneous scattering and the additional phase shift due to coherent scattering. The important parameters to choose are the detunings of the pump light with respect to the atomic transition and with respect to the cavity resonance frequency. In this section the case of resonant pumping is discussed, the following section treats the off-resonant case.
In the resonant case the pump light frequency is chosen to be equal to the atomic transition ($\Delta_a = 0$), and the cavity frequency is tuned to this resonance ($\Delta_c = 0$). The number of photons transmitted through the cavity can be derived from Equation 3.30 to be

$$N_{\text{out}} = \frac{\eta^2}{(\kappa+\gamma)^2}\kappa_T\tau = j_{\text{in}}\tau\left(\frac{\kappa_T}{\kappa}\right)^2\frac{\kappa^2}{(\kappa+\gamma)^2} = N_{\text{out},0}\frac{\kappa^2}{(\kappa+\gamma)^2}. \tag{3.40}$$

$N_{\text{out},0}$ is the number of photons transmitted through the empty cavity ($\gamma = 0$) which is the the input power diminished by the factor $\left(\frac{\kappa_T}{\kappa}\right)^2$, due to intra-cavity losses.

3.3.1 Signal-to-noise ratio

Hence the measurable signal due to a single atom in the cavity is

$$\begin{aligned}\Delta N_{\text{out}} &= N_{\text{out},0} - N_{\text{out}} = j_{\text{in}}\tau\left(\frac{\kappa_T}{\kappa}\right)^2\left[1 - \frac{\kappa^2}{(\kappa+\gamma)^2}\right] \\ &= N_{\text{out},0}\left[1 - \frac{\kappa^2}{(\kappa+\gamma)^2}\right].\end{aligned} \tag{3.41}$$

For the signal-to-noise ratio this yields

$$\begin{aligned}S &= \frac{\Delta N_{\text{out}}}{\sqrt{N_{\text{out}}}} = \sqrt{N_{\text{out},0}}\left(\frac{\kappa+\gamma}{\kappa} - \frac{\kappa}{\kappa+\gamma}\right) \\ &= \sqrt{N_{\text{out},0}}\left(1 + \frac{\gamma}{\kappa} - \frac{1}{1+\frac{\gamma}{\kappa}}\right).\end{aligned} \tag{3.42}$$

The Figure 3.3 shows the results discussed above for resonant pumping and cavity parameters chosen to be realistic for the fibre cavities discussed in Section 2.5, which are $(g, \kappa_T, \kappa_{\text{lo}}) = 2\pi \times (12, 3, 6)$MHz, corresponding to a fibre cavity of length $L = 21$mm and waist $w_0 = 2.92\mu$m. In Figure 3.3 (a), the cavity transmission N_{out} with an atom present in the cavity mode (lower curve) and without (upper curve) are plotted. Beside the number of outcoupled photons (solid lines), the quantum noise given by the width of the Poissonian number distribution of the coherent state $\sqrt{N_{\text{out}}}$ (dashed lines) are plotted as a function of pumping power. The transmitted photon number is linear for the cavity without atoms. For the case of an atom present in the cavity, this photon number is strongly reduced as long as the atomic transition is not saturated. At the

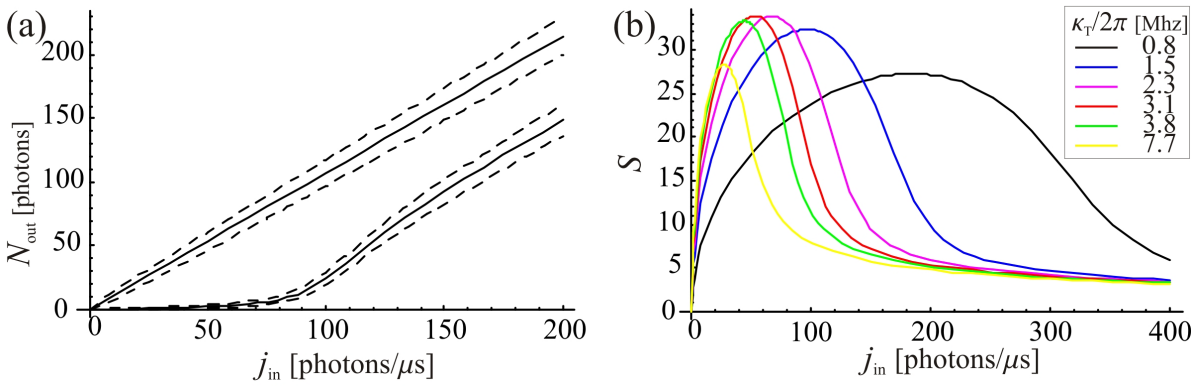

Figure 3.3: Figure (a) shows the transmitted photon number with (lower solid curve) and without (upper solid curve) an atom present in the cavity, the dashed curves correspond to the quantum noise level, the cavity parameters are $(g, \kappa_T, \kappa_{\rm lo}) = 2\pi \times (12, 3, 6)$MHz. Figure (b) shows the corresponding signal-to-noise ratio, for the same cavity parameters except the mirror transmission is different for the different curves. The cavity transmission rates κ_T, as listed in the inset, correspond to mirror transmissions of $(0.1, 0.2, 0.3, 0.4, 0.5, 1)\%$ (from right to left).

saturation point this photon number bends, and for strong coupling the curves for $N_{\rm out}$ and $N_{\rm out,0}$ differ by a constant value, as predicted by Equation 3.49.

The atomic decay rate for the D2 transition of Rb is $\Gamma = 2\pi\times 3$ MHz. Now one can compute the cooperativity parameter $\frac{g_0^2}{\kappa\Gamma} = 5.3$. Even though this is not yet deep in the strong coupling regime (see Equation 3.32), a single atom detection in $\tau = 10\mu$s integration time is feasible with signal-to-noise ratio $S > 30$, as shown in Figure 3.3 (b). In this plot the cavity parameters are the same as in (a), except for the mirror transmission rate, which is varied over the different curves.

The maximum value is obtained at $\kappa_T \approx 2\pi \times 3$MHz, which is about half the loss rate $\kappa_{\rm lo} = \pi\times 6.3$MHz. The general relation between κ_T and $\kappa_{\rm lo}$ to get the best signal-to-noise ratio can be found numerically to be

$$\begin{aligned} \kappa_T &\approx \kappa_{\rm lo}/2, \qquad \text{for} \quad \frac{g(\vec{r})^2}{\kappa\Gamma} \ll 1 \quad \text{(weak coupling)}, \\ \kappa_T &\approx \kappa_{\rm lo}, \qquad \text{for} \quad \frac{g(\vec{r})^2}{\kappa\Gamma} \gg 1 \quad \text{(strong coupling)}, \end{aligned} \tag{3.43}$$

To find the limit for single atom detection in the weak-coupling regime, the loss rate is further increased, keeping the mirror transmission rate at the optimal value of $\kappa_T = \kappa_{\rm lo}/2$. Figure 3.4 shows the result in a log-log-plot again as a function of the pump rate. Signal-to-noise ratios larger than 1 can be reached for loss rates up to $\kappa_{\rm lo} = 2\pi\times 500$MHz, which corresponds to a finesse of $\mathfrak{F} = 2.4$ for the fiber cavity described above.

This shows drastically, how well a small mode cross-section, providing a large coupling constant g, compensates for high cavity decay rates. This is a motivation to push miniaturization of optical cavities to enhance the atom-light interaction.

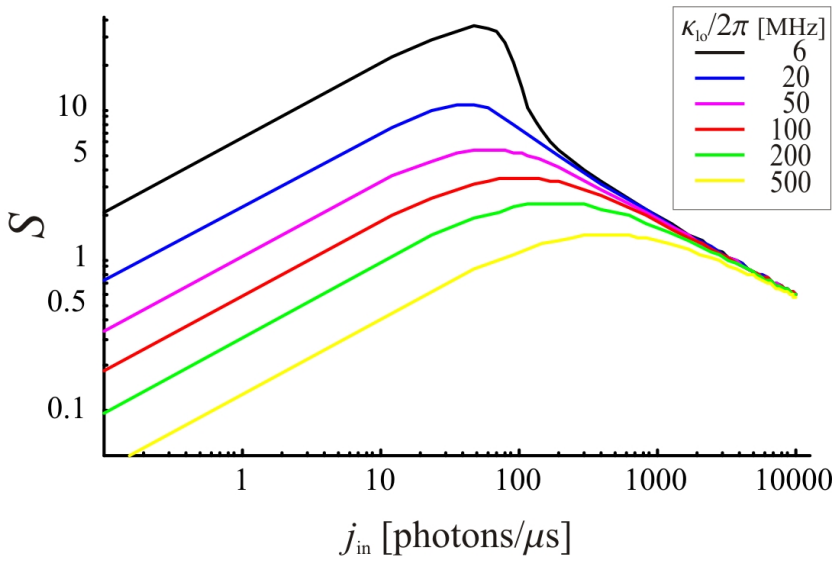

Figure 3.4: The signal-to-noise is plotted as a function of pump power for different cavity loss rates κ_{lo}, as listed in the inset. The mirror transmission rate was chosen to be optimal for every curve $\kappa_T = \kappa_{\mathrm{lo}}/2$

Low atomic saturation

If one now assumes weak pumping ($N \ll 1$), which causes low atomic saturation ($2Ng(\vec{r})^2 \ll \Gamma^2$), the additional cavity decay rate (from Equation 3.27) can be simplified to $\gamma = \frac{g(\vec{r})^2}{\Gamma}$. The figure of merit for the signal-to-noise ratio is the ratio of the additional cavity decay due to the atoms and the intrinsic decay rate

$$\frac{\gamma}{\kappa} = \frac{g(\vec{r})^2}{\kappa\Gamma}, \tag{3.44}$$

This expression is identical to the cooperativity parameter, which has been identified before (see Equation 3.32).
In the limit of weak coupling ($\frac{g(\vec{r})^2}{\kappa\Gamma} \ll 1$), Equation 3.42 reduces to

$$S = 2\sqrt{N_{\mathrm{out},0}}\frac{g(\vec{r})^2}{\kappa\Gamma} = 2\sqrt{j_{\mathrm{in}}\tau}\frac{\kappa_T}{\kappa}\frac{g(\vec{r})^2}{\kappa\Gamma}. \tag{3.45}$$

Instead in the strong coupling limit ($\frac{g(\vec{r})^2}{\kappa\Gamma} \gg 1$), one finds

$$S = \sqrt{N_{\mathrm{out},0}}\frac{g(\vec{r})^2}{\kappa\Gamma} = \sqrt{j_{\mathrm{in}}\tau}\frac{\kappa_T}{\kappa}\frac{g(\vec{r})^2}{\kappa\Gamma}. \tag{3.46}$$

Hence, for low atomic saturation the signal-to-noise ratio is proportional to the square root of the pumping power j_{in} and the integration time τ, but it is linear in the cooperativity parameter. Losses degrade the signal-to-noise by the factor κ_T/κ. Assuming maximum coupling $g(\vec{r}) = g_0$, Equation 3.38 can be used to express the cooperativity parameter as

$$\frac{g_0^2}{\kappa\Gamma} = 2\frac{\sigma_a}{A}n_{\mathrm{rt}}, \tag{3.47}$$

and thus the cavity enhanced signal-to-noise ratio is proportional to

$$S \propto \sqrt{N_{\mathrm{out},0}}\frac{\sigma_a}{A}n_{\mathrm{rt}}, \tag{3.48}$$

as predicted by the simple model in Section 3.1. This reflects again the two strategies useful to maximize the atom detection probability, namely to increase the number of round trips by increasing the cavity quality and to decrease the cavity mode waist. An interesting point is that the cooperativity parameter does not depend upon cavity length[1]. This will be of importance later, when the miniaturization of cavities is discussed.

High atomic saturation

In the opposite case of high atomic saturation ($2Ng(\vec{r})^2 \gg \Gamma^2$) due to strong pumping ($N \gg 1$), the additional cavity decay rate reduces to $\gamma = \frac{\Gamma}{2N} = \frac{\Gamma\kappa^2}{2j_{\mathrm{in}}\kappa_T}$, and since $\frac{\gamma}{\kappa} \ll 1$ the transmitted photon number simplifies to

$$N_{\mathrm{out}} = j_{\mathrm{in}}\tau\left(\frac{\kappa_T}{\kappa}\right)^2\left(1 - \frac{\Gamma\kappa}{j_{\mathrm{in}}\kappa_T}\right) = N_{\mathrm{out},0} - \Gamma\tau\frac{\kappa_T}{\kappa}. \tag{3.49}$$

This is the result for the empty cavity reduced by the number of scattered photons at the saturation limit $M_{\mathrm{sat}} = \Gamma\tau$ times the cavity transmittance factor $\frac{\kappa_T}{\kappa}$.
For the signal to noise level one finds

$$S = \sqrt{N_{\mathrm{out},0}}\frac{\Gamma\kappa^2}{j_{\mathrm{in}}\kappa_T} = \sqrt{j_{\mathrm{in}}\tau}\frac{\kappa_T}{\kappa}\frac{\Gamma\kappa}{j_{\mathrm{in}}\kappa_T} = \sqrt{\frac{\tau}{j_{\mathrm{in}}}}\Gamma. \tag{3.50}$$

After the atomic transition is saturated, the signal-to-noise ratio decreases with the inverse square root of the input power, since the number of photons scattered is limited by the saturation value $M_{\mathrm{sat}} = \Gamma\tau$, while the noise level increases further $\sqrt{N_{\mathrm{out}}} = \sqrt{j_{\mathrm{in}}\tau}$. The interesting fact here is that this result is independent of all cavity parameters.

3.3.2 Disturbance of the atom

Another quantity of interest is the average number of photons scattered by the atom during a detection process. For a state preserving single atom detection, one only has to make sure not to influence the atomic motion too much during the detection process, in order to keep the atom within the mode volume as long as possible. The effect on the atomic motion is discussed in detail in [Hor03]. For more ambitious goals like using cavities for reversible quantum logic operations small or no spontaneous decay would have to be required.

[1] This is valid as long as the cavity length does not influence the loss rate, which is true in the present experiment, where losses are dominated by scattering at surfaces.

The number of spontaneous emissions during the integration time is given by the decay rate and the population of the excited state (Equation 3.25)

$$M = 2\Gamma\tau\rho_{11} = 2\Gamma\tau\frac{g(\vec{r})^2 N}{\Gamma^2 + 2g(\vec{r})^2 N}. \tag{3.51}$$

In the case of high saturation, as mentioned before, this number will be constant and given by the saturation value

$$M_{\mathrm{sat}} = \Gamma\tau. \tag{3.52}$$

Low atomic saturation

In the limit of low atomic saturation ($2g(\vec{r})^2 N \ll \Gamma^2$) this can be approximated by

$$M = 2\tau\frac{g(\vec{r})^2 N}{\Gamma} = \frac{2\tau g(\vec{r})^2}{\Gamma}\frac{j_{\mathrm{in}}\kappa_T}{\kappa^2}\left(\frac{1}{1+\frac{g(\vec{r})^2}{\kappa\Gamma}}\right)^2. \tag{3.53}$$

In the weak-coupling limit $\left(\frac{g(\vec{r})^2}{\kappa\Gamma} \ll 1\right)$, $N = N_0$ holds, and, expressed in terms of the signal-to-noise ratio S in Equation 3.45, the number of spontaneous emissions becomes

$$M = 2\tau j_{\mathrm{in}}\frac{\kappa_T}{\kappa}\frac{g(\vec{r})^2}{\kappa\Gamma} = S^2\,\frac{1}{2}\frac{\kappa}{\kappa_T}\left(\frac{g(\vec{r})^2}{\kappa\Gamma}\right)^{-1}. \tag{3.54}$$

In the strong-coupling limit $\left(\frac{g(\vec{r})^2}{\kappa\Gamma} \gg 1\right)$, using Equation 3.46, one finds

$$M = 2\tau j_{\mathrm{in}}\frac{\kappa_T}{\kappa}\left(\frac{g(\vec{r})^2}{\kappa\Gamma}\right)^{-1} = S^2\,2\frac{\kappa}{\kappa_T}\left(\frac{g(\vec{r})^2}{\kappa\Gamma}\right)^{-3}. \tag{3.55}$$

Hence, for a fixed signal-to-noise ratio in the strong-coupling regime, the number of spontaneously scattered photons is inversely proportional to the cooperativity parameter. This can be related to cavity finesse, since the cooperativity parameter is proportional to the number of round trips n_{rt} according to Equation 3.32) and consequently proportional to the cavity finesse according to Equation 2.31. Which means that the number of spontaneous scattering events, necessary to achieve a certain signal-to-noise ratio, is proportional to $\mathfrak{F}^{-3}$. This shows that the best strategy to drastically decrease the number of spontaneous scattering events is to improve the cavity finesse.
In Figure 3.5 the number of spontaneously scattered photons is plotted for different cavity loss rates, from $\kappa_{\mathrm{lo}} = 2\pi \times 20\mathrm{MHz}$, a value which has been realized for a fibre cavity already experimentally (see Section 4.8.4), to $\kappa_{\mathrm{lo}} = 2\pi \times 6\mathrm{MHz}$, which is the fibre cavity loss rate due the mode-mismatch in a 5μm gap (see Section 2.5). In the region where the signal-to-noise ratio is highest, the number of spontaneous scattering events is large. If one wants to disturb the atom as little as possible, the pump rates will have to be kept small, as shown in Figure 3.6. This figure shows a zoom into the small input power region of Figure 3.5. The figure shows that it is possible to push the number of

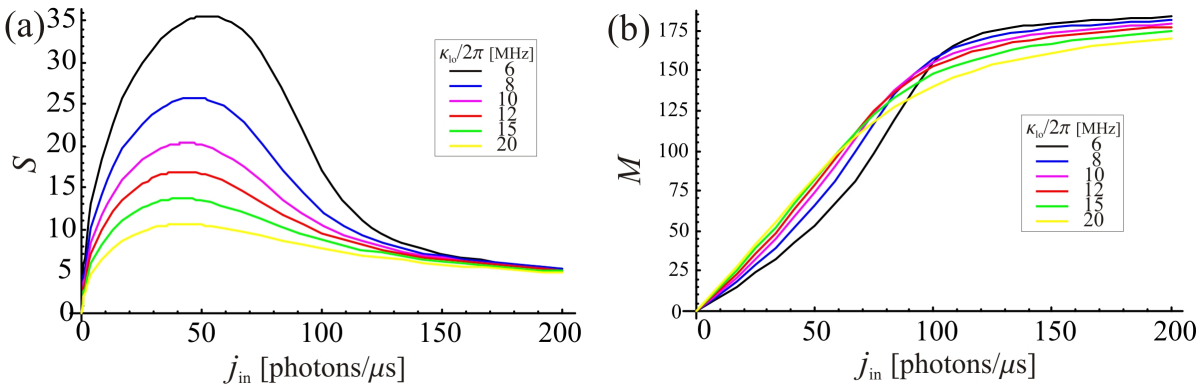

Figure 3.5: Figure (a) shows the signal-to-noise ratio for cavities of different loss rates, as listed in the inset, in Figure (b) the number of spontaneous emissions during the detection interval of $\tau = 10\mu$s is plotted for the same cavity parameters.

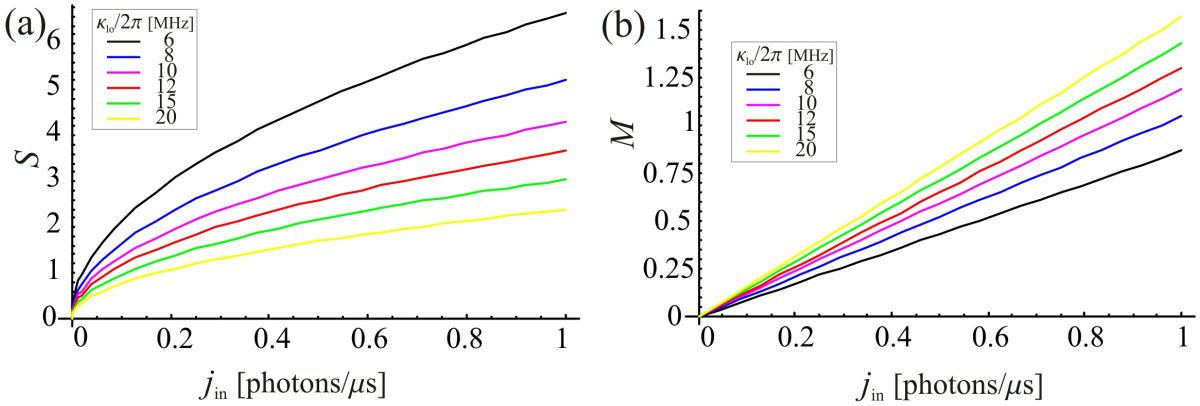

Figure 3.6: The plots represent a zoom into Figure 3.5 for small pump powers, to show the parameter region where the disturbance of the atom during the detection process is smallest. The different cavity loss rates for the curves are listed in the insets, respectively.

scattered photons far below one, while maintaining a signal-to-noise above one.
A technical problem may occur, since an increasing number of round trips decreases the outcoupled photon number for the same atomic saturation level. This can be estimated by looking at the number of transmitted photons during a detection process as a function of the signal to noise ratio. In the weak coupling limit

$$N_{\text{out}} \approx N_{\text{out},0} = S^2 \frac{1}{4} \left(\frac{g(\vec{r})^2}{\kappa\Gamma} \right)^{-2} . \tag{3.56}$$

Hence for fixed signal-to-noise ratio, the absolute signal level is proportional to $1/n_{\text{rt}}^2$, which for cavities of higher finesse will require the use of very sensitive detectors, if one wants to explore the low-saturation limit where a non-destructive detection of single atoms is possible.

In summary, single atom sensitivity can be achieved with a minimal backaction on the atom due to a cavity-induced increased atom-coupling. This is a clear advantage compared to conventional fluorescence imaging, where detection of single atoms is not possible without strongly disturbing it.

3.4 Off-resonant atom detection

In the last section, cavity and atom were pumped resonantly. It has been shown that single atom detection with a small number of scattering events is feasible, but this requires quite strong coupling, causing small absolute signal amplitudes. The question is now, whether larger absolute signals can be obtained by detuning the pump beam from the atomic transition. The dispersive interaction of atoms and cavity would then be used to detect the atom.
If one now assumes large atom-pump detuning ($\Delta_a \gg \Gamma$), but keeps the cavity in resonance with the pump beam ($\Delta_c = 0$), the atom's influence on the cavity decay rate is much smaller than the influence on the light shift ($\gamma \ll U$). So Equation 3.29 becomes

$$\alpha = \frac{\eta}{\kappa + iU} = \frac{\eta}{\kappa}\frac{1}{1 - i\phi}, \tag{3.57}$$

where

$$\phi = -\frac{U}{\kappa}. \tag{3.58}$$

If ϕ is small, Equation 3.57 can be written as

$$\alpha = \frac{\eta}{\kappa}e^{i\phi} = \alpha_0 e^{i\phi}. \tag{3.59}$$

This shows that ϕ actually causes a phase shift, rather than an amplitude change to the cavity signal. The outcoupled photon number $N_{\text{out}} = |\alpha|^2\kappa_T\tau = \alpha_0^2\kappa_T\tau = N_{\text{out},0}$ is constant independent of the presence of an atom in the cavity. Hence, a phase sensitive technique is needed to detect a change in the signal.

3.4.1 Homodyne detection

A phase sensitive technique is provided by homodyne detection [Aga97]. Here a strong local oscillator, namely an additional laser beam that is phase coherent to the pumping light, is overlapped with the cavity output beam on a 50/50 beamsplitter as depicted in Figure 3.7. The amplitudes of the cavity beam α and the local oscillator $i\beta$ interfere ($|\beta|^2$=photon number per time), which leads to oscillating photon counts at the detectors $D_{1,2}$

$$\begin{aligned} N_{1,2} &= \left|\frac{1}{\sqrt{2}}\left(\alpha\sqrt{\kappa_T} \pm i\beta\right)\right|^2 \tau = \frac{1}{2}\left|\left(\alpha_0\sqrt{\kappa_T}e^{i\phi} \pm i\beta\right)\right|^2 \tau = \\ &= \frac{1}{2}\left(\alpha_0^2\kappa_T + \beta^2 \pm 2\alpha_0\sqrt{\kappa_T}\beta\sin\phi\right)\tau. \end{aligned} \tag{3.60}$$

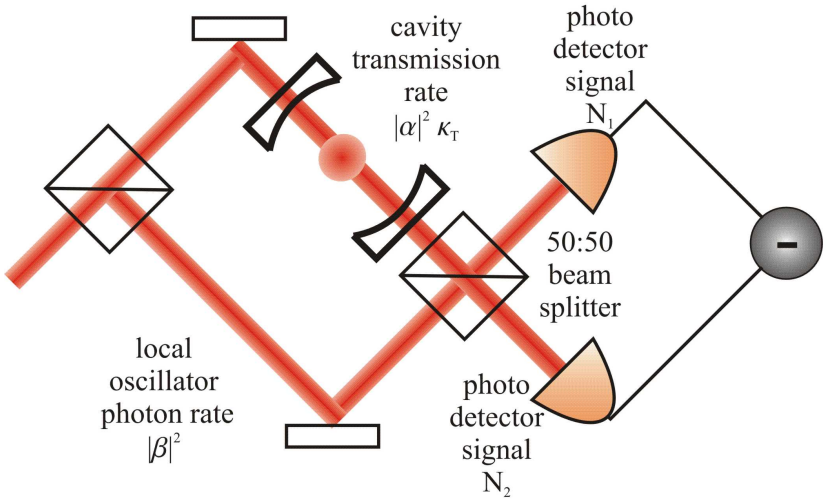

Figure 3.7: The scheme of a homodyne detector: by measuring the interference signal between two beams, the phase shift caused by an atom in the cavity in one of the arms can be detected.

If one subtracts the two detector signals under the assumption of small phase shifts ϕ, one gets

$$\Delta N = N_1 - N_2 = 2\alpha_0\sqrt{\kappa_T}\beta\tau \sin\phi \approx 2\sqrt{N_{\text{out},0}\tau}\beta\phi, \tag{3.61}$$

which is proportional to the phase shift induced by the atoms. For the signal-to-noise ratio one finds

$$S_{\text{hom}} = \frac{\Delta N}{\sqrt{N_1 + N_2}} = \frac{2\sqrt{N_{\text{out},0}\tau}\beta\phi}{\sqrt{(\alpha_0^2\kappa_T + \beta^2)\,\tau}} \approx 2\sqrt{N_{\text{out},0}}\phi. \tag{3.62}$$

This is plotted in Figure 3.8 for the same cavity parameters (g, κ_{lo}) as in the resonant case (see Figure 3.3 b), but a detuning of the pump beam of $\Delta_a = 50\Gamma$ from the atomic resonance is chosen. One finds from the plot that the maximum signal-to-noise ratio is reached at $\kappa_T \approx 6$MHz, which is equal to the cavity loss rate κ_{lo}. Again, it has been found numerically that the generalization holds: S_{hom} is maximized for $\kappa_T \approx \kappa_{\text{lo}}$, so for a given loss rate, the mirror transmission has to be larger than in the resonant case for low saturation. The value of the maximum signal-to-noise ratio is only slightly smaller than in the resonant case (see Figure 3.3).

Low atomic saturation

In the limit of low atomic saturation $(2Ng(\vec{r})^2 \ll \Gamma^2)$ the phase simplifies to $\phi = \frac{g^2}{\kappa\Delta_a}$, which makes it possible to express S_{hom} in terms of the signal to noise ratio for resonant detection (Equation 3.45)

$$S_{\text{hom}} = 2\sqrt{j_{\text{in}}\tau}\frac{\kappa_T}{\kappa}\frac{g(\vec{r})^2}{\kappa\Delta_a} = \frac{\Gamma}{\Delta_a}S. \tag{3.63}$$

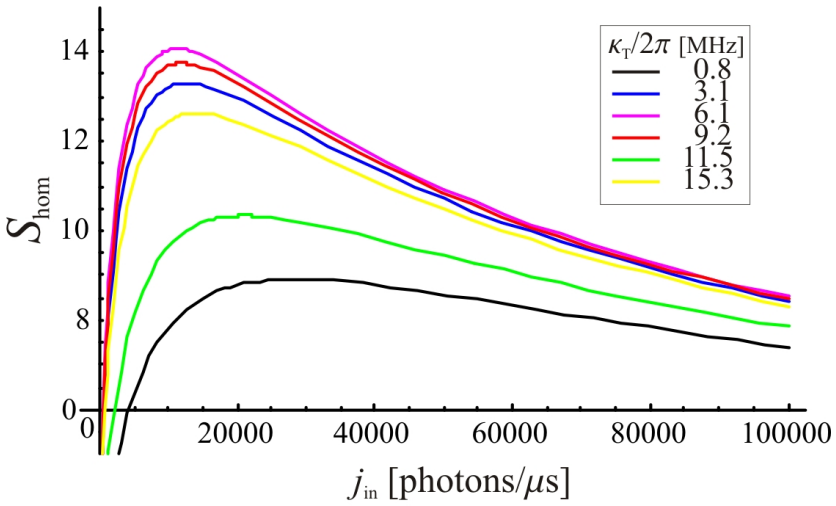

Figure 3.8: The homodyne signal-to-noise ratio as a function of the mirror transmission rate for the usual cavity parameters $(g, \kappa_{\rm lo}) = 2\pi \times (12, 6)$MHz and a pump-atom detuning $\Delta_a = 50\Gamma$. The different curves are given by different mirror transmission rates κ_T, as listed in the inset, corresponding to mirror transmissions of $(0.1, 0.4, 0.8, 1.2, 1.5, 2)\%$ (from black to yellow).

This means that the signal-to-noise ratio obtained by homodyne detection is much smaller than the signal-to-noise ratio in the resonant case for the same pumping power. But in order to chose the most appropriate detection technique, one has to compare resonant and non-resonant detection, considering the disturbance of the atom which is necessary to achieve a certain signal-to-noise ratio. This will be done in Section 3.4.2.

High atomic saturation

In the case of high atomic saturation $(2Ng(\vec{r})^2 \gg \Gamma^2)$, the phase becomes $\phi = \frac{\Delta_a}{2N_0\kappa}$. The signal-to-noise ratio can be compared again to the resonant case (Equation 3.50)

$$S_{\rm hom} = 2\sqrt{N_0\kappa_T\tau}\frac{\Delta_a}{2N_0\kappa} = \sqrt{\frac{\tau}{j_{\rm in}}}\Delta_a = \frac{\Delta_a}{\Gamma}S, \tag{3.64}$$

and is found to be larger by a factor $\frac{\Delta_a}{\Gamma}$.
A plot of the homodyne signal-to-noise ratios for different cavity loss rates is shown in Figure 3.9 (a), where the optimal ratio of the decay rates $\kappa_T = \kappa_{\rm lo}$ was chosen. All other parameters are the same as in Figure 3.8. The result looks encouraging, but the drawback in this case is that the disturbance of the atom is the same as in the resonant case, since the number of scattered photons is given by the saturation value $M_{\rm sat} = \Gamma\tau$ as in the resonant case (see Equation 3.52).
In Figure 3.11(a) the numerical result for the signal-to-noise ratio (for the standard cavity parameters and detection interval $\tau = 10\mu$s) is shown together with the two approximations for high an low atomic saturation, which agree well in the respective limit.

3.4.2 Backaction on the atom

The number of spontaneous emissions during the detection interval is again the product of decay rate, measurement time, and excited state population:

$$M = 2\Gamma\tau\rho_{11} = 2\Gamma\tau\frac{g(\vec{r})^2 N}{\Delta_a^2 + \Gamma^2 + 2g(\vec{r})^2 N}. \tag{3.65}$$

This value is plotted in Figure 3.9 (b) as a function of the pump rate. The various curves correspond to different cavity loss rates for the same parameters as in Figure 3.9 (a). As in the resonant case, zooming into these plots (see Figure 3.10), one finds

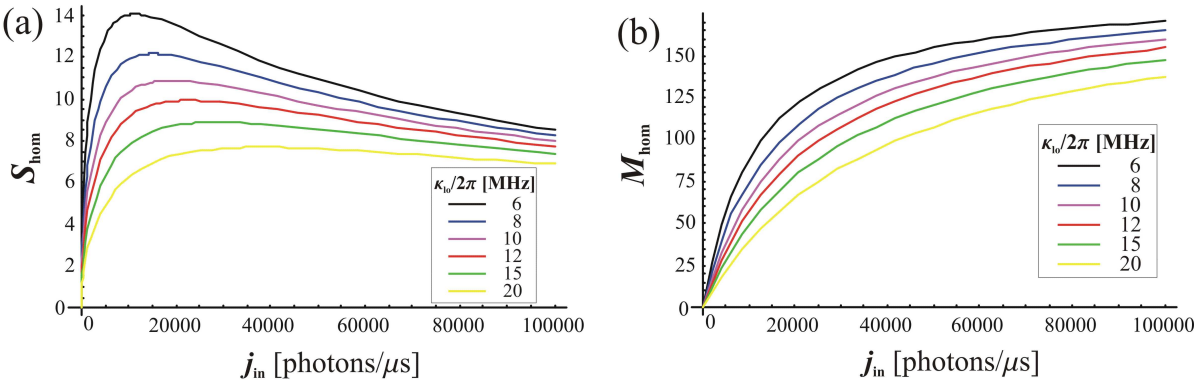

Figure 3.9: Figure (a) is showing the signal-to-noise ratios, Figure (b) the number of spontaneously emitted photons in a detection interval of $\tau = 10\mu$s. The different curves correspond to different cavity loss rates $\kappa_{\rm lo}$, as shown in the insets.

a pump intensity domain, where the number of spontaneous emissions is much smaller than unity, while the signal-to-noise ratio is larger than unity in a measurement interval of $\tau = 10\mu$s.

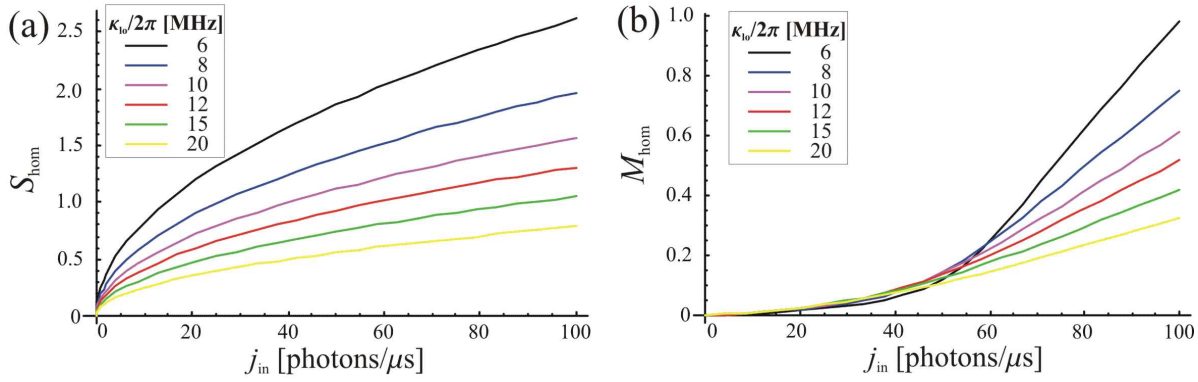

Figure 3.10: This figure shows a zoom into Figure 3.9 for small pump powers. Here disturbance of the atom during the detection process is smallest. The different cavity loss rates for the curves are listed in the insets.

This shows that also the non-resonant detection scheme is suitable for single-atom detection with low disturbance of the atom.

Low atomic saturation

This results can be approximated for the low atomic saturation case ($2Ng(\vec{r})^2 \ll \Gamma^2$). Turning to the number of scattered photons, since $\rho_{11} = \frac{g^2 N_0}{\Delta_a}$, one finds

$$M_{\mathrm{hom}} = 2\Gamma\tau\rho_{11} = 2j_{\mathrm{in}}\tau\frac{\kappa_T}{\kappa}\frac{g(\vec{r})^2}{\kappa\Delta_a}\frac{\Gamma}{\Delta_a}, \tag{3.66}$$

and expressed in terms of S_{hom}

$$M_{\mathrm{hom}} = S_{\mathrm{hom}}^2\frac{1}{2}\frac{\kappa}{\kappa_T}\left(\frac{g(\vec{r})^2}{\kappa\Gamma}\right)^{-1}. \tag{3.67}$$

This a very important result, because this relation is the same as in the weak coupling limit for the resonant case (Equation 3.54). Concerning the disturbance of the atoms, in this limit one does not gain or lose anything by detuning the pump light, since the same signal-to-noise ratio is only achieved at the same number of spontaneously scattered photons. This is because the reduced atom-photon coupling in the far detuned limit has to be compensated by a larger pump power which produces a larger number of scattered photons.
In Figure 3.11(b) the numerical result for the number of spontaneous scattered photons is shown together with the two approximations for low and high atomic saturation, which well describe the two limits. In the high atomic saturation the result is just given by the constant value M_{sat}.

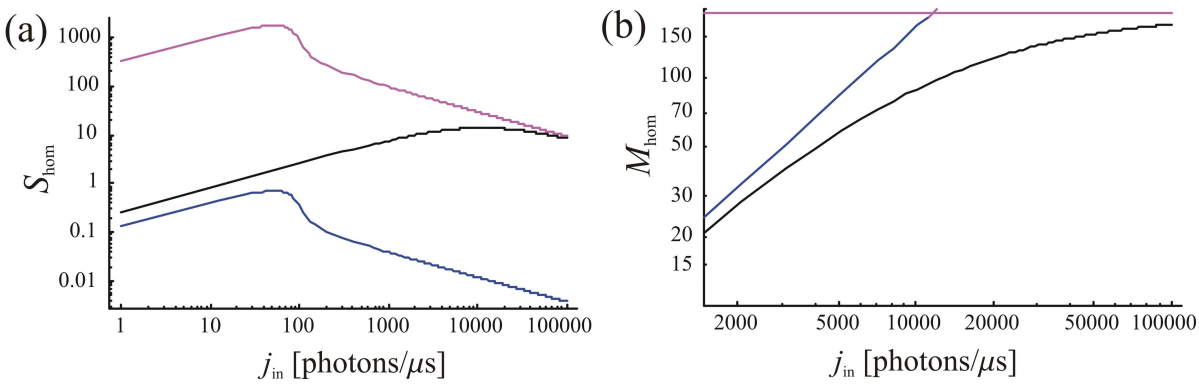

Figure 3.11: The figure shows the signal-to-noise ratio in (a) and the number of scattered photons in (b) for a typical cavity with $(g, \kappa_{\mathrm{lo}}, \kappa_T, \Delta_a) = 2\pi \times (12, 6, 6, 900))$. Beside the exact numerical calculation shown by the black curve, the two approximation for low and high atomic saturation are show in the blue and in the violet curve respectively.

Is there an advantage of using non-resonant detection? Looking at the absolute signal

level, the number of transmitted photons is found to be

$$N_{\text{out}} = N_{\text{out},0} = j_{\text{in}}\tau \left(\frac{\kappa_T}{\kappa}\right)^2 = \frac{1}{4} S_{\text{hom}}^2 \left(\frac{g(\vec{r})^2}{\kappa\Gamma}\right)^{-2} \left(\frac{\Delta_a}{\Gamma}\right)^2 \tag{3.68}$$

which is by a factor $\left(\frac{\Delta_a}{\Gamma}\right)^2$ higher than for the resonant scheme (see Equation 3.56). Thus, by varying the detuning, one can choose a preferred signal height, depending on the sensitivity of the detectors being used. This is a clear technical advantage, because even for the comparably low finesse cavities descibed it is already an issue to chose the right detector to resolve the small cavity signals.

3.5 Application to many atoms systems

So far, the detection of single atoms has been discussed. Adapting the theory to the interaction of atomic clouds with the cavity mode is principally straightforward. The two identified effects on the atoms one the cavity field, i.e. the additional decay rate γ (Equation 3.27) and the additional phase shift U (Equation 3.28) scale linearly with the number atoms. If all atoms would feel the same field and hence the same coupling g_0, the total coupling would be simply given by $N_a\, g_0$, the number of atoms times the maximum single-atom coupling constant. But problems arise, as soon as these atoms do not feel the same field. In the setup described in this thesis, where a cavity near the concentric limit is used (see Section 4.5), the intensity varies not only radially but also axially within the cavity. This, one can not assume a maximum coupling constant at all position in the trap. This problem can be solved by multiplying the term $N_a\, g_0$ with the overlap integral of atomic density and cavity mode function, in order to get an effective many-atom coupling constant.
The atomic density normalized to unity is then

$$\rho(\vec{r},t) = \frac{1}{(2\pi)^{\frac{3}{2}}\sigma_x(t)\sigma_y(t)\sigma_z(t)} \exp\left(\frac{-\left(x - x_c(t)\right)^2}{2\sigma_x(t)^2} - \frac{y^2}{2\sigma_y(t)^2} - \frac{z^2}{2\sigma_z(t)}\right), \tag{3.69}$$

where the cloud is assumed to be of Gaussian shape, with widths $\sigma_x(t)$, $\sigma_y(t)$, $\sigma_z(t)$. These parameters are time dependent since the atoms are free falling or magnetically guided through the cavity (see Section 4.4). In the free falling case the cloud expands freely according to its Maxwell-Boltzmann velocity distribution. In the guided case, this expansion is restricted to the free axis of the guide. A movement of the cloud centre $x_c(t)$ is assumed only in the direction of gravity.
The mode function normalized to the mode volume (Equation 2.25 where pure phase factors are neglected) is given by

$$\psi(\vec{r}) = \frac{w_0}{w(z)} \exp\left(-2\frac{x^2+y^2}{w(z)^2}\right) \cos(kz). \tag{3.70}$$

The atom-cavity coupling strength is given by the total atom number times the maximum coupling weighted by the overlap integral

$$\int dV\, N_{\mathrm{a}}(\vec{r},t)g(\vec{r}) = N_{\mathrm{a,max}}\, g_0 \int dV \rho(\vec{r},t)|\psi(\vec{r})|^2. \tag{3.71}$$

To analyze this overlap integral, first the integration is carried out along the x,y-directions, transversal to the cavity axis. Averaging out the intensity modulation from the standing wave packet, one gets

$$\int dV \rho(\vec{r},t)|\psi(\vec{r})|^2 = \int_{-L/2}^{L/2} dz \frac{w_0^2}{8\sqrt{2\pi}} \frac{\exp\left(-\frac{x_c(t)^2}{2\sigma_x(t)^2\left(1+\frac{w(z)^2}{(2\sigma_x(t))^2}\right)} - \frac{z^2}{2\sigma_z(t)^2}\right)}{\sigma_x(t)\sigma_y(t)\sigma_z(t)\sqrt{1+\frac{w(z)^2}{(2\sigma_x(t))^2}}\sqrt{1+\frac{w(z)^2}{(2\sigma_y(t))^2}}}. \tag{3.72}$$

Since the mode width $w(z)$ is much smaller than the transversal width of the atomic cloud $2\sigma_{x,y}$, their ratio can be neglected in comparison to 1, which simplifies the expression to

$$\int dV \rho(\vec{r},t)|\psi(\vec{r})|^2 = \int_{-L/2}^{L/2} dz \frac{w_0^2}{8\sqrt{2\pi}} \frac{\exp\left(-\frac{x_c(t)^2}{2\sigma_x(t)^2} - \frac{z^2}{2\sigma_z(t)^2}\right)}{\sigma_x(t)\sigma_y(t)\sigma_z(t)}. \tag{3.73}$$

Finally the overlap integral can be expressed in terms of the error function $\mathrm{erf}(x) = \frac{2}{\sqrt{\pi}}\int_0^x \mathrm{e}^{-u^2} du$

$$\int dV \rho(\vec{r},t)|\psi(\vec{r})|^2 = \frac{w_0^2}{8\sigma_x(t)\sigma_y(t)} \exp\left(-\frac{x_c(t)^2}{2\sigma_x(t)^2}\right) \mathrm{erf}\left(\frac{L}{2\sqrt{2}\sigma_z(t)}\right). \tag{3.74}$$

This result shows a fundamental difference from the single atom experiment. Since this overlap integral scales like the square of the mode waist, it seems favorable to increase the mode cross section. This is of course the case for a detection of atomic clouds, since the number of atoms in the high-intensity regions of the mode increases, and has to be contrasted with the best condition for single atom detection, which require a small waist for maximum cooperativity (see Equation 3.32).
Using this overlap integral another useful measure can be defined, namely an effective number of atoms in the mode volume, which is given by

$$N_{\mathrm{eff}}(t) = N_{\mathrm{a,max}} \int dV\, \rho(\vec{r},t)|\psi(\vec{r})|^2. \tag{3.75}$$

This can be interpreted as the atom number, which would have an equal effect on a cavity with the same mode volume, but a uniform field of with the maximum intensity of the Gaussian mode. For comparison, to give the same mode volume, a uniform mode would have to be of cylindrical shape with diameter w_0 and length L, which is tiny compared to the extensions of the Gaussian cavity field. So looking at the outcome of the overlap integral in Figure 3.12, it is finally not surprising that this effective atom number is very small, for example dropping a MOT of 10^7 atoms the effective atom

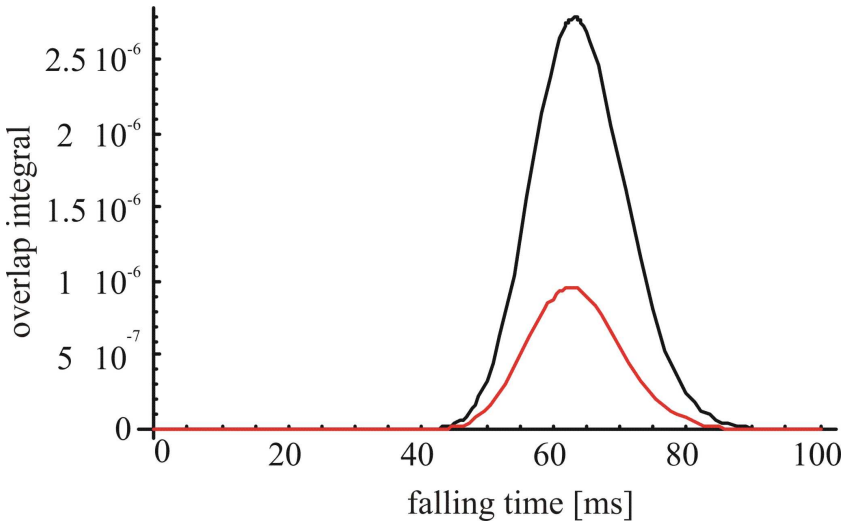

Figure 3.12: Overlap integral of the normalized atomic density and the normalized cavity mode function under typical experimental conditions: An atomic cloud of $\sigma_0 = 1.5$mm, temperature $T = 43\mu$K ($v = 65$mm/s mean thermal velocity) dropped from 2cm above the cavity with mode waist $w_0 = 12.0\mu$m. The red curve shows freely falling atoms, the black curve a cloud which is magnetically guided through the cavity.)

number in the cavity would reach $N_{\text{eff}} \approx 8$ at its maximum. This gives already a flavor of how experimentally challenging it will be, to place a single atom into the even smaller mode volume of a fibre resonator see Chapter 5.5.
Also the cooperativity parameter scales now with the effective number of atoms in the mode volume, so the new measure, wether the cavity is weakly or strongly coupled to the many-atom system is given by the quantity

$$\int dV\, N_a(\vec{r},t)\frac{g(\vec{r})}{\kappa\Gamma} = N_{\text{eff}}(t)\frac{g_0}{\kappa\Gamma} \tag{3.76}$$

being smaller or bigger than 1.
There is a further problem, when the theory has to be applied to many atom systems, caused by there is another term containing the spatial dependent coupling constant $2g(\vec{r})N$ in the denominator of γ and U (Equations 3.27 and 3.28). Here the spatial dependence can not be averaged out as easily. However, this term is negligible in the low saturation regime $2g^2N \ll \Gamma^2$, where the intra-cavity photon number remains small. Hence, in the low saturation regime all the derived formulas remain valid for many atom systems if one multiplies the single-atom coupling constant with the effective number of atoms in the mode volume. In the high saturation regime, the theory obtained by replacing the spatially dependent coupling constant in the nonlinear term $2g(\vec{r})^2N \ll \Gamma^2$ by the maximum coupling g_0 will give an upper bound for the effects produced by the atoms on the cavity field.
To quantify the power for which the saturation sets in, the Equation

$$\frac{2g^2N}{\Gamma} = 1 \tag{3.77}$$

is solved for the cavity pump power P_{in}, which is introduced into the Equation for the intra-cavity photon number 3.30 via the cavity pump rate

$$\eta^2 = \frac{P_{\text{in}}\kappa_T}{\hbar\omega}. \tag{3.78}$$

To receive a result which is comparable to the experimental data, the input power, which is never measured directly, has to be translated into a transmitted power of the empty cavity

$$P_{\text{out},0} = P_{\text{in}} \left(\frac{\kappa_T}{\kappa}\right)^2. \tag{3.79}$$

Figure 3.13 shows the resulting saturation curve as a function of the effective atom number in the mode volume. The cavity parameters are $(g_0, \kappa_T, \kappa_{\text{lo}}) = 2\pi\times(3.0, 1.2, 2.0)$MHz.

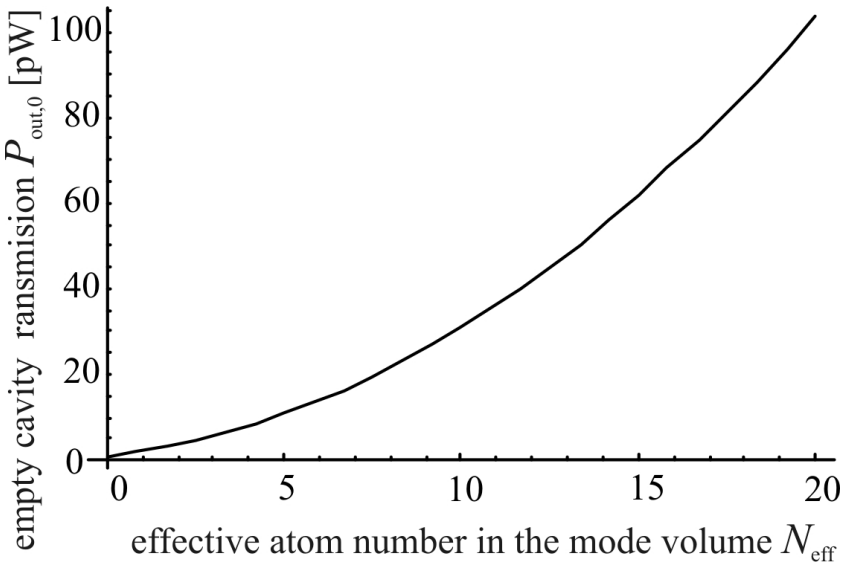

Figure 3.13: The saturation curve as a function of the effective number of atoms in the mode volume.

3.5.1 Optical bistability

Another feature of this coupled atom-cavity system is optical bistability [Dru81, Lug84, Rem91]. It sets in, when the nonlinearity between incoupled and outcoupled field becomes important,. It describes the discontinuous switching of the cavity output between two stable states depending on the intra-cavity atom number.
First off all, it has to be pointed out that the onset of bistability is depending on whether the atoms in the mode can be saturated. Because of spacial variation of the cavity waist, and atomic density, this is extremely position dependent. While in the mode waist this happens first,further out on the cavity axis the effect sets in much later. In the single-atom model this manifests itself in the spacial dependency of the coupling constant in the nonlinear term which describes saturation effects $2g(\vec{r})^2N$, where $\vec{r}$ is the position

of the atom. For the many-atom system, both atomic distribution and mode function would have to be considered. In the following the effect will be discussed qualitatively, assuming a uniform maximum coupling g_0.
To identify the regime of optical bistability, the input power will be expressed as a function of the transmitted power of the cavity. For this purpose Equation 3.30 is solved for the pump rate

$$\eta^2 = N\left[(\kappa+\gamma)^2 + (\Delta_c - U)^2\right]. \tag{3.80}$$

Expressing η again by cavity pump power and the intra-cavity photon number N in terms of the and the transmitted power

$$P_{\text{out}} = N\hbar\omega\kappa_T, \tag{3.81}$$

and by making use of the effective atom number per mode volume, introduced in Equation 3.77, one finds

$$P_{\text{in}} = \frac{P_{\text{out}}}{\kappa_T^2}\left[\left(\kappa + \frac{N_{\text{eff}}g^2\Gamma}{\Gamma^2+\Delta_a^2+2g^2\frac{P_{\text{out}}}{\hbar\omega\kappa_T}}\right)^2 + \left(\Delta_c - \frac{N_{\text{eff}}g^2\Delta_a}{\Gamma^2+\Delta_a^2+2g^2\frac{P_{\text{out}}}{\hbar\omega\kappa_T}}\right)^2\right]. \tag{3.82}$$

For a given value of P_{in} this equation has in general three solutions for P_{out}. Figure 3.14 shows these solutions as a function of the atom number in the mode volume N_{eff}. The different curves correspond to different P_{in} (here from 0.32nW for the lowest curve to 6.8nW for the highest). The figure shows that after a critical input power (here

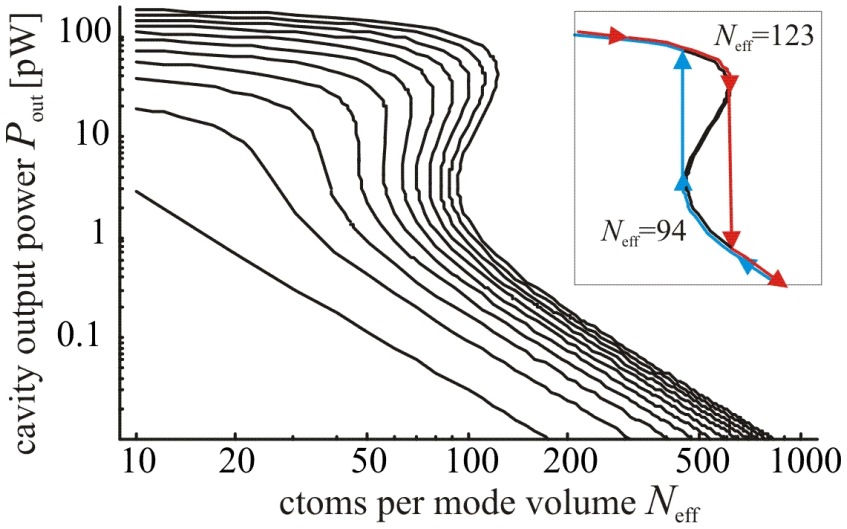

Figure 3.14: The cavity output power as a function of the atom number in the cavity mode. The different curves correspond to different input powers. For the left curve P_{in} is 0.32nW and increases to 6.8nW for the right curve in steps of 0.65nW. The inset shows the hysteresis curve of the cavity output power if the atom number increases and decreases again, as the cloud falls through the cavity. The cavity parameters are $(g_0, \kappa_T, \kappa_{\text{lo}}) = 2\pi \times (2.5, 2.1, 10.8)$MHz as for the cavity of length $L = 19.86$mm and finesse $\mathfrak{F} = 290$ described in Chapter 5.

≈ 2.2nW for the 4th curve from the left), the dependence of P_{out} from the atom number per mode N_{eff} becomes strongly nonlinear and for a certain input power range three solutions exist. In the experiment, the input power is constant, let us say 6.8 nW, as in the upper curve. Now the atoms are falling into the cavity, thus the effective atom number in the cavity mode starts to increase. At a critical atom number, in this specific case $N_{\text{eff}} = 94$, the system enters the bistabllity region, where more than one stationary solutions is possible. In this region the cavity is bistable, but as long as there are no further influences, the output power will keep following the solution in the upper part of the curve as the atom number increases. As soon as it reaches the opposite side of the instability region, at the atom number $N_{\text{eff}} = 123$, in order to follow the solution for even higher atom number, the cavity is forced to switch to much smaller intra-cavity photon number, which results in a drop of the output power by more than two orders of magnitude (as shown in the inset of Figure 3.14).
After the centre of the atom cloud has crossed the cavity mode, the effective atom number in the mode volume starts to decrease and the cavity output power is following the curve upwards. Analogous to before, entering the bistability region at $N_{\text{eff}} = 123$, the solution continues to follow the lower part of the curve. The switching happens at the end of the instability region for $N_{\text{eff}} = 94$ (as shown in the inset). Correspondingly a sudden increase in the output power is observed. Hence, the cavity output intensity follows a hysteresis curve. This effect was experimentally observed e.g. in [Rem91].

Relevance for the experiment

The influence on the cavity transmission signal would look as depicted in Figure 3.15. The cavity transmission signal is plotted as a function of falling time and maximum atom number in the mode volume. For small atom numbers the signal shows a Gaussian shaped dip, caused by the Gaussian shaped atom cloud, scattering light off the cavity field. But for higher atomic densities bistability sets in, which completely switches off the cavity output. The asymmetry between the points where the cavity switches off and on again are a signature of the hysteresis described above.
Unfortunately, it is very hard to observe bistability in the weak coupling regime, where all the experiments described in this work were in, due to the high effective atom number needed in the mode volume for the onset of the switching. As it can be seen in Figure 3.14 for typical cavity parameters the critical atom number is $N_{\text{eff}} \approx 50$, below which independently of the cavity power bistablillity does not occur.
The experiments described here were concentrated on the other side the parameter space, namely to measure the the resolution limit of the cavity (see Chapter 5). So the maximum effective atom numbers reached, were $N_{\text{eff}} \approx 10$. This is far away from entering the bistable regime, particularly because the coupling constant was far away from being maximal in the whole mode, which was assumed in the last section.

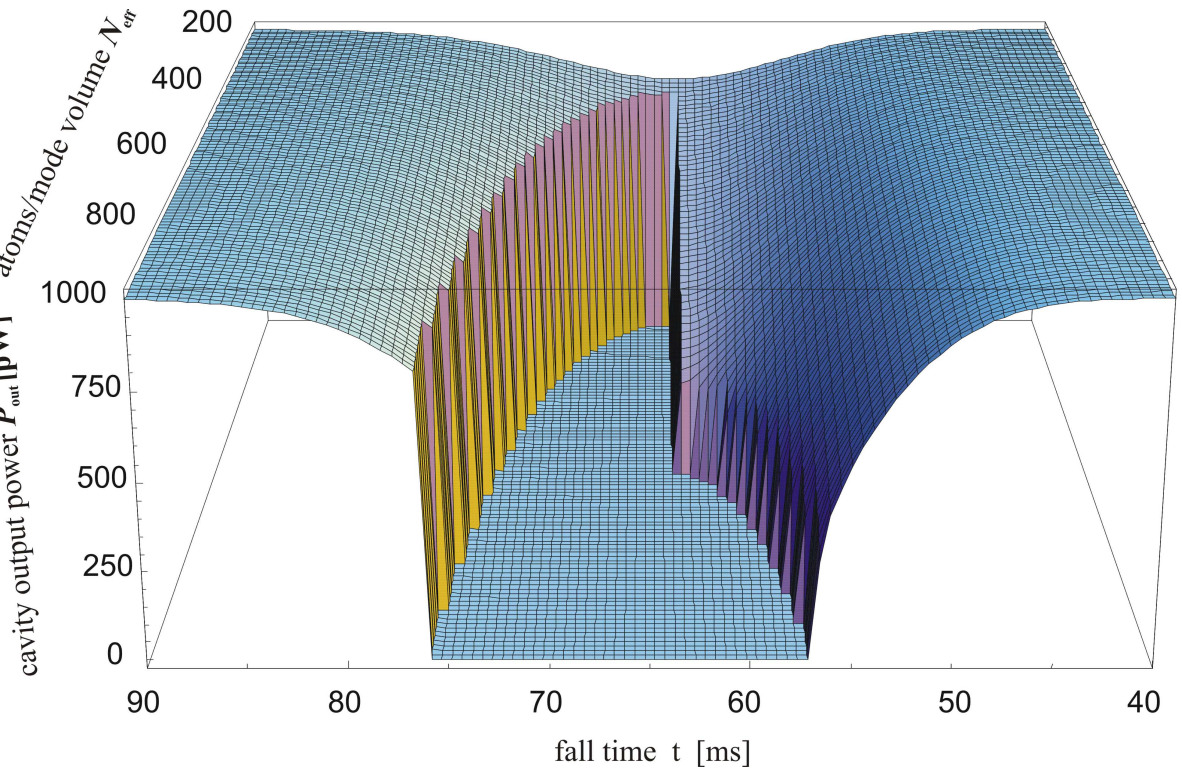

Figure 3.15: The cavity transmission signal is plotted as a function of falling time and maximum atom number in the mode volume. In the high saturation the signal is a Gaussian shaped dip. With an increasing number of atoms the system becomes bistabil which leads to a discontinuous switching of the cavity output signal.

4 Experimental setup

In this chapter the main elements of the experiment will be briefly described. The setup consists of the vacuum chamber (Section 4.1), the laser system (Section 4.2) which provides the light for a magneto-optical trap (MOT) (Section 4.3) and the cavity (Section 4.5), the magnetic guide (Section 4.4), the detectors to record the cavity transmission signal (Section 4.6), and the computer control system (Section 4.7). Furthermore, the planned experimental extensions to include an atom chip with integrated micro-cavity are described (Section 4.8).

4.1 Vacuum system and coils

The vacuum chamber (see Figure 4.1) consists of a cross with six CF63 flanges which connects the ion pump, the titanium sublimation pump, the turbo pump, gauge and a flooding valve to the main chamber. This main chamber is made from stainless steel of type 316LN (DIN 1.4429) with especially low magnetic permeability ($\mu < 1.005$). It has four small and one big viewport, made from high optical quality glass and sealed with Helicoflex gaskets. A big flange holds the cavity mounting and another one the rubidium dispensers. For the experiment described in this work, the main chamber hosted a conventional six-beam MOT (see Figure 4.1), but it was designed to be easily rebuilt into an atom chip setup (see Section 4.8).
The MOT quadrupole coils have been designed to minimize heating of the chamber, by using copper wire of 4 mm^2 cross section. This was necessary, since with the previous coils of 1 mm^2 wire a temperature increase of up to 90°C was observed, which could lead to unwanted cavity drifts. Figure 4.2 shows the chamber with mounted MOT coils and a view inside the chamber.
For the future atom chip experiments, there will be no need of external anti-Helmholtz coils. Instead a large current-carrying U-shaped copper structure below the chip, together with a homogeneous bias field will allow to create the quadrupole-like potential (see Section 4.8.3 and [Wil04], more on wire traps can be found in [Wei95, Haa01]). The required changes in the setup are sketched in Figure 4.3.

4.2 Laser system

In the experiment two main laser frequencies are involved to drive transitions between the hyperfine states $5^2S_{1/2}$ and $5^2P_{3/2}$ of rubidium [Ari77] at 780nm. This light is produced by laser diodes, two are needed for the MOT, one for cooling, one for repuming. In the

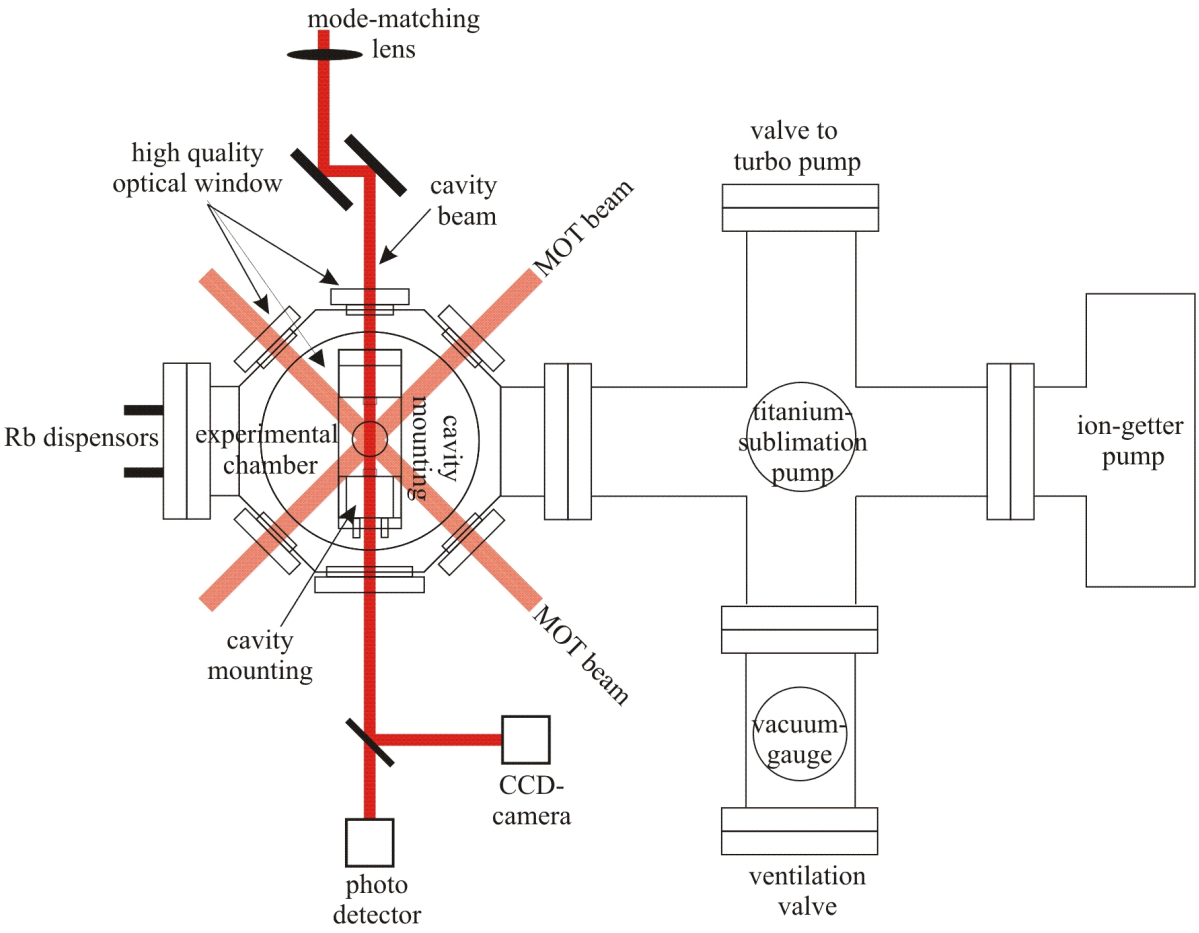

Figure 4.1: The vacuum system, consisting of an experimental chamber with universal optical access, which is connected via a six-way-cross to pumps and valves.

case of ^{85}Rb the cooling transition is $|5^2S_{1/2}, F = 3\rangle \rightarrow |5^2P_{3/2}, F = 4\rangle$. The cooling cycle is closed by repumping the atoms via the $|5^2S_{1/2}, F = 2\rangle \rightarrow |5^2P_{3/2}, F = 3\rangle$ transition (see Figure 4.4).
A third laser is resonantly driving the cavity at the cooling transition, and a fourth diode is injection-locked by the cavity laser and delivers an additional light beam for the heterodyne detection scheme (see Section 4.6).

4.2.1 Frequency stabilization

The lasers are near-infrared laser diodes, three of them, the two for the MOT and one as the cavity pump laser, are stabilized by an external cavity created by a grating in Littrow configuration [Ric95], the fourth is injection looked [Roh96] by the cavity laser (details about the latter in Section 4.6.2). For the active stabilization two different schemes are used: a frequency modulation (FM) lock [Bjo79] to achieve permanent stabilization onto the resonances of a Doppler-free saturation spectroscopy of Rb and a frequency offset lock [Sch99] to preserve tunability within a few 100 MHz around these resonances.

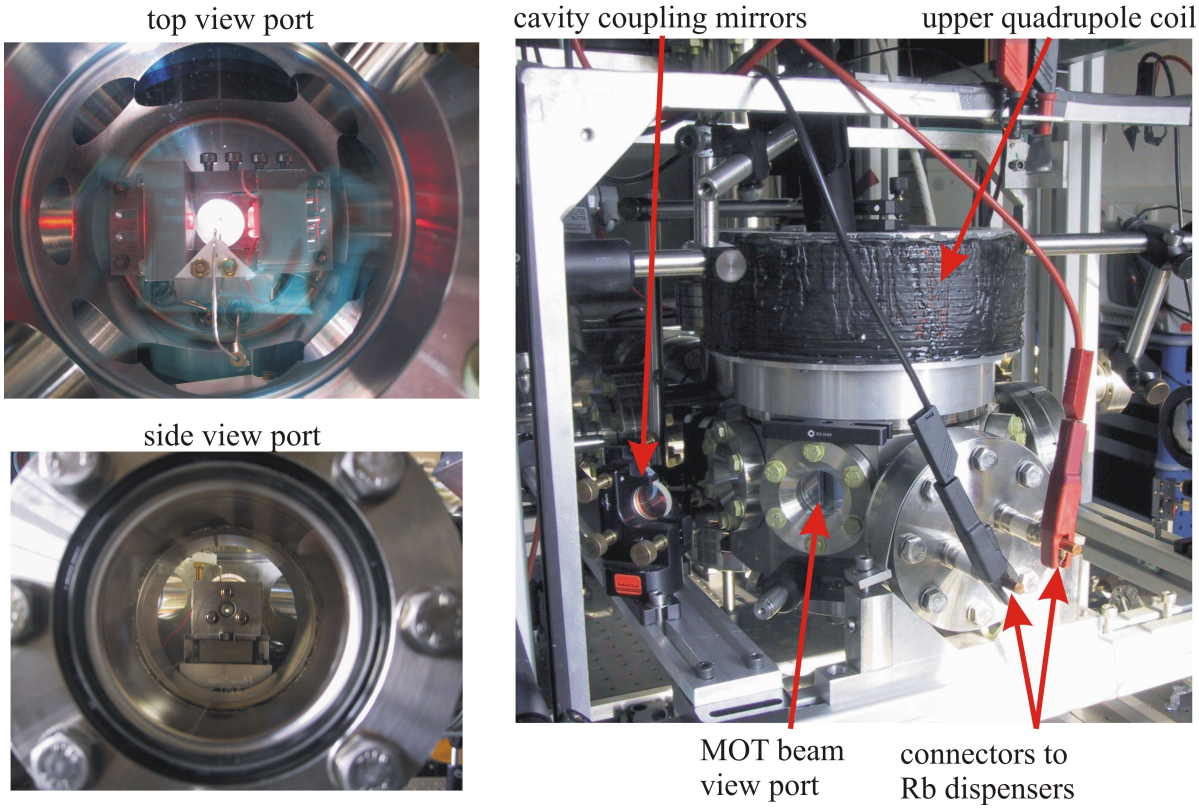

Figure 4.2: Views into the experimental chamber and a view onto the chamber with mounted MOT coils.

Frequency modulation lock

To provide the two different frequencies needed for the cavity and for the MOT repumping transitions, two lasers are locked independently using the frequency-modulation technique [Bjo79].
The scheme is sketched in Figure 4.5 and its realization in this experiment is described in detail in [Wil02]. The laser light is weakly modulated with a radio frequency from quartz oscillator, in our case 20MHz. By sending this modulated beam through a rubidium gas cell, the amplitude and the phase of carrier and side bands are changed due to absorbtion and dispersion (the pump and probe technique avoids Doppler broadening by just acting on the zero velocity atoms [Dem03]). Since the amplitude and phase changes are frequency dependent, the beating between carrier and red sideband and between carrier and blue sidebands, which normally cancels out, is now phase shifted. One detects a beat note at the modulation frequency, whose amplitude is proportional to the lasers frequency shift and thus can serve as an error signal.
For a low bandwidth stabilization, the FM error signal is fed back to a piezo crystal, which moves the laser cavity grating. This slow feedback loop is limited by the piezo resonance frequency around 8kHz. It leads to a laser linewidth reduction to 1.3MHz from a few MHz for the free running diode. A second, fast feedback loop acts on the

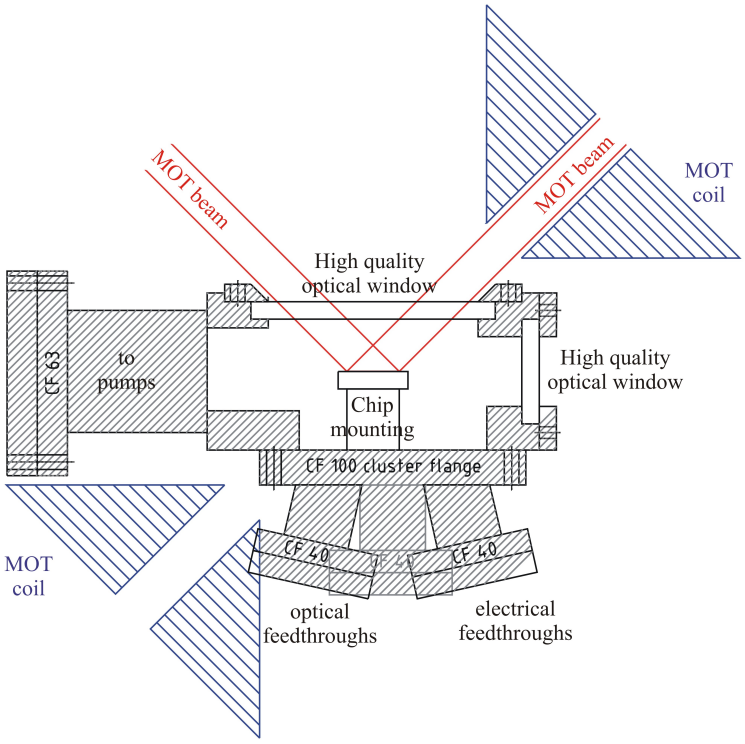

Figure 4.3: The figure shows the experimental chamber from the side. It shows, how easily the setup can be adapted to host an atom chip with the corresponding reflection MOT. Furthermore, a novel wire configuration below the chip, developed in our group [Wil04], allows to replace the big quadrupole coils, which are still depicted in this figure.

laser current with a bandwidth of 1.1MHz. This reduces the laser linewidth again to less than 500kHz [Wil02], which is good enough, since the atomic linewidth and the smallest cavity linewidth were both about 6MHz.

Frequency offset lock

A third laser has to be tunable to a certain extend, since it serves as the MOT cooling laser and is red detuned by 15 MHz with respect to the cooling transition,in the optical molasses phase it has to be even further red-detuned ($\approx$ 30 MHz), and finally it needs to be tuned back exactly to the resonance for imaging the atoms (for details see Section 4.3).
This laser is stabilized relative to another one, in this specific case the cavity laser, with a variable radio frequency offset [Sch99]. As depicted in Figure 4.6, a small part of the light from the two lasers is overlapped and the beat note is measured with an avalanche photodiode (APD). The amplified APD signal is mixed with a radio-frequency from a voltage-controlled oscillator (VCO). A low pass filter transmits only the difference frequency, which is then split and, after a delay line in one arm, recombined at a phase detector. The phase shift, acquired during the splitting, is proportional to the detuning between VCO and laser beating frequency. Thus the output amplitude of the phase

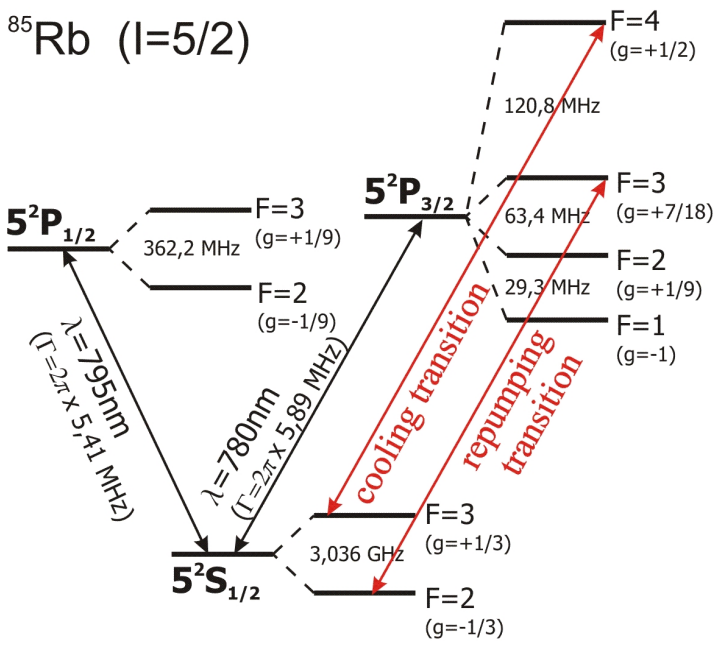

Figure 4.4: The level scheme of ^{85}Rb, the level spacing of the hyperfine structure is shown together with the Landé-factors g, which become important for magnetical trapping (see Section 4.4). The MOT is operated on the 780nm D2-line, as marked in red.

detector varies as the cosine of this phase shift. This creates an appropriate error signal proportional to the cosine of the laser frequency difference (cooling laser-cavity laser) minus the offset frequency. The limit to this offset frequency is the bandwidth of the phase detector, which causes an envelope function on top of the error signal. The bandwidth was chosen to be 100 MHz in this experiment. Working again with two feedback circuits, a slow one acting on the piezo and a fast one for the laser current, a linewidth reduction to < 1 MHz was achieved [Wil02].

4.2.2 Optical path

After laser stabilization, the available intensity is $\approx$ 15mW in each laser beam. The optical path is depicted in Figure 4.7. To switch the MOT beam intensities, the laser beams are sent through acousto-optical modulators (AOM) where about 85% of the intensity is coupled into the first order. In the case of the repumper, which is locked to the flank of the spectroscopy signal, the AOM frequency of 110MHz shifts the laser frequency back to the atomic resonance. The cooling beam is shifted by 80MHz, which is compensated by the offset locking scheme discussed above. After passing the AOMs, both MOT beams are overlapped on a polarizing beam splitter cube (PBS) after their polarizations have been adjusted properly by $\lambda/2$-plates. The beam waist is expanded by a telescope to about 15mm, and the beams are split again by $\lambda/2$-plates and PBS into three equally intense beams of $\approx$ 3mW, which are sent through the vacuum chamber

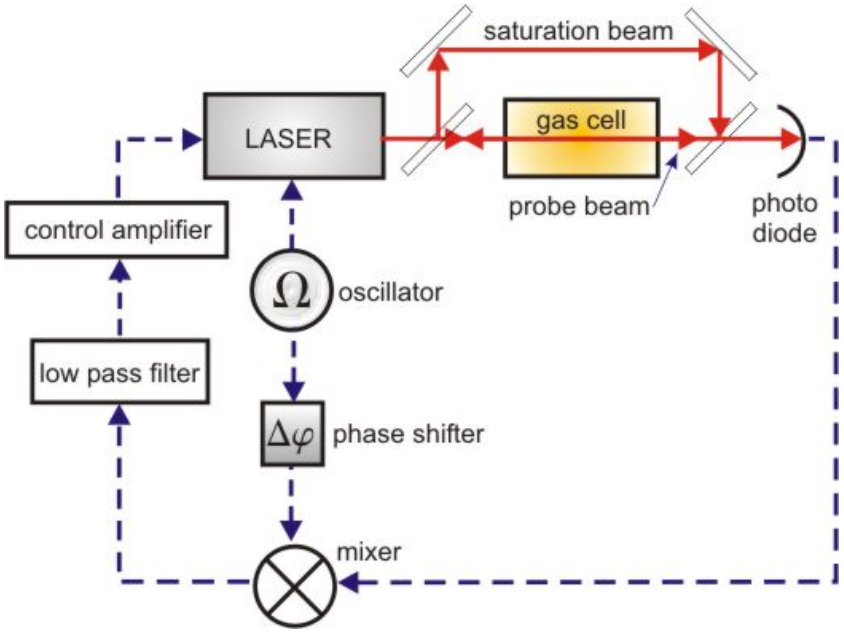

Figure 4.5: FM lock scheme, for technical details see [Wil02]. The VCO modulates the laser. Mixing it with the spectroscopy light allows to detect a beat node at this modulation frequency. A low pass filter eliminates higher order terms and the phase shifter allows to switch between absorptive and dispersive signal.

along orthogonal directions, after their polarizations have been changed to left, respectively right circular as required for the MOT [Raa87]. The two horizontal beams are crossing just above the cavity mounting, at a distance of 2mm from the cavity axis. The third vertical beam is sent through a hole in the cavity mounting (see Figure 4.2). After having crossed the chamber, the polarizations are rotated by 90° and the three beams are retro-reflected, which in total provides the 6 MOT beams.
The cavity beam is sent through an AOM twice, in order to even stronger attenuate its amplitude. Since the cavity laser is locked to the crossover peaks of the Doppler-free saturation spectroscopy (between $|5^2S_{1/2}, F = 3\rangle \rightarrow |5^2P_{3/2}, F = 2\rangle / |5^2P_{3/2}, F = 3\rangle$), which is 152.5MHz away from the cooling transition, the AOM radio frequency is tuned to 76.3MHz, which after the double passage exactly shifts the laser back to the cooling transition resonance. The beam is then focussed by a lens and two mirrors into the cavity inside the camber. By choosing the right focal length and lens distance, the beam waist and the wave front curvature are matched to the cavity mode (see Section 2.3).

4.3 Cold Atom Source

The magneto-optical trap produces a cloud of cold rubidium atoms just above the cavity mounting. The MOT is limited by the laser power of ≈ 1.2mW per beam and a beam diameter of ca. 15mm. It was optimized to produce atom numbers of up to 10^8, which were measured by focussing the fluorescence signal onto a calibrated photodiode. A

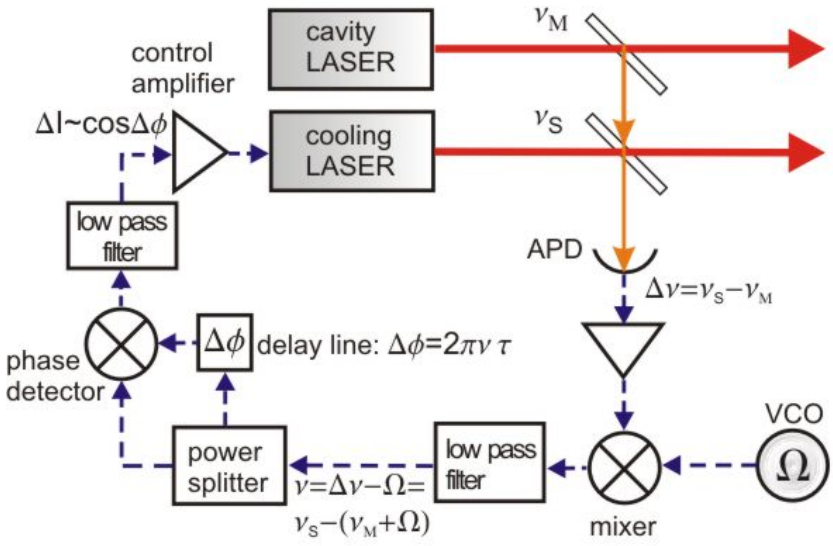

Figure 4.6: Frequency offset locking scheme, for technical details see [Wil02]. After mixing the beating signal with a radio frequency, the signal difference is extracted by a low-pass filter, is split and recombined after a delay line introduced a phase shift in one arm. After the phase detector, and after higher order contributions are eliminated by another low pass, the signal is proportional to the cosine of the phase shift, which is proportional to the frequency difference of cooling laser and cavity laser plus offset.

maximum atom number was found for a cooling beam detuning of 14MHz to the red, and a magnetic field gradient of 14 G/cm [Wil02].
The temperature of the atoms was determined by time of flight imaging using a CCD camera and by measuring analyzing the temporal width of the cavity signal (see Section 5.2.1). For freely expanding clouds temperatures of down to $T \approx 30\mu$K have been measured, which is far below the Doppler temperature of 141μK. This has been achieved by polarization gradient cooling in the MOT and a following 20ms molasses phase, after the magnetic quadrupole field has been switched off and the cooling laser detuning was raised to 23MHz [Mat02].
The MOT can be shifted in all three directions by short ramps of homogeneous magnetic offset fields, to find the best position for dropping the atoms into the cavity or to overlap them with the minimum of the magnetic potential, which can be used to guide the atoms through the cavity [Den99].

4.4 Magnetic guide

Besides dropping the atoms and letting them pass through the cavity in free fall, a magnetic wire guide can be used to guide and compress the cloud. This has the advantage that the crossing position can be chosen more precisely and the atomic cloud density and size can be determined by the potential parameters [Haa01].
The magnetic trapping is based on the interaction of the magnetic dipole of the atom

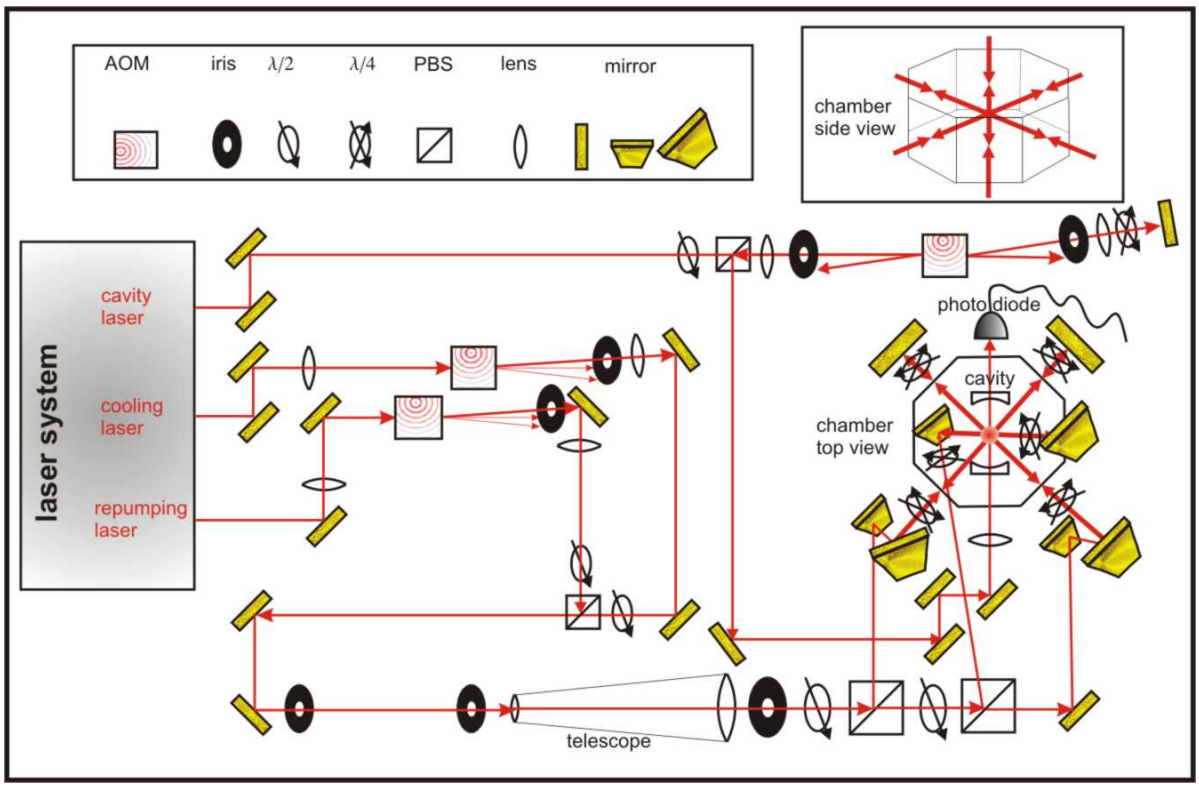

Figure 4.7: The optical beam path providing light for the MOT and the cavity, AOMs are switching the beam intensities.

with an external magnetic field. The interaction energy is given by

$$E_{pot} = -\vec{\mu} \cdot \vec{B} = \mu_B \, m_F \, g_F \, B, \tag{4.1}$$

where μ_B is the Bohr magneton, m_F the magnetic quantum number, g_F the Landé factor of the hyperfine state F. Since in free space magnetic maxima cannot be formed by static fields [Ear42], only atoms in states attracted to magnetic field minima, the so-called low-field-seeking states are trappable. In the case of ^{85}Rb atoms these are the states $|F = 3, m_F = 1, 2, 3\rangle$, $|F = 2, m_F = -1, -2, \rangle$, since their Landé factors are $g_{F=3} = 1/3$ and $g_{F=2} = -1/3$.
The necessary magnetic field geometry is created by a current carrying wire structure and an external homogeneous magnetic bias field along the cavity axis [Den99]. This potential is created by a wire current $I_{\text{wire}} = 33\text{A}$ and a bias field $B_{\text{bias}} = 10\text{G}$ which were found to be the optimal values for loading the guide from the MOT (see Section 5.3.1). Ideally this potential should be quadrupole-like close to the minimum. Due to the the non-perfect homogeneity of the bias field, which is produced by coils not in the ideal Helmholtz-configuration, and due to a magnetic field contribution from the wire leads it deviates from this quadrupole-shape. The field is for example non-zero at the potential minimum, which is an advantage because it prevents non-adiabatic spin flips [Maj32] into untrapped states which are lost from the trap. The results of realistic

potential calculations are shown in Figure 4.8. Figure (a) and (b) show contour plots of the potential perpendicular (a) and parallel (b) to the wire, the darkest area indicates the potential minimum. Figure (c) and (d) are potential plot in the horizontal plane at the position of this minimum. The trap trap depth at the MOT loading position slightly below the upper bent of the wire was found to be $T = 580\mu$K.

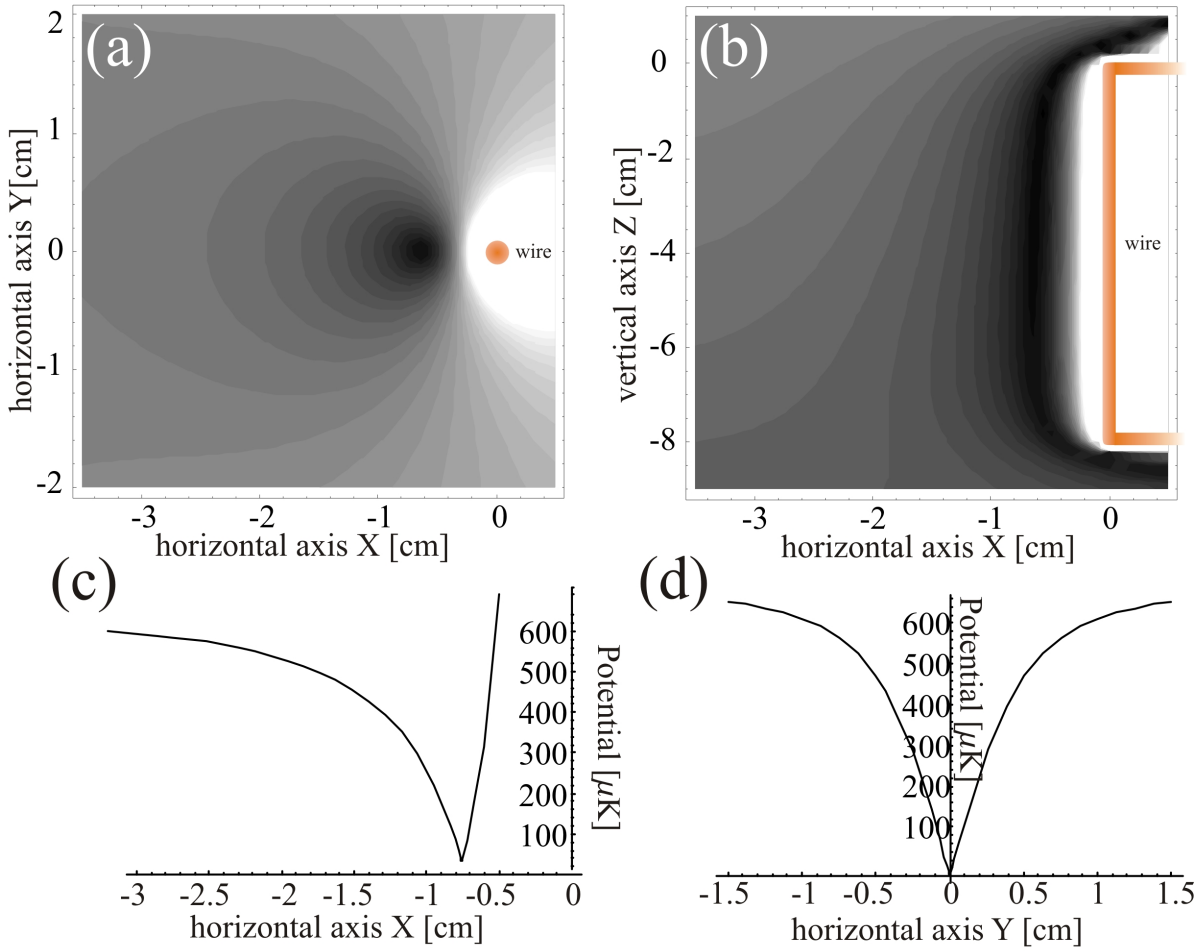

Figure 4.8: The magnetic potential created by the bent wire structure is shown in the horizontal plane containing the cavity axis in Figure (a) and in a central plane perpendicular to the cavity axis in Figure (b). The potential increases from black to white. The trap parameter are wire current $I_{\text{wire}} = 33$A and bias field $B_{\text{bias}} = 10$G.

The wire structure of 1mm diameter is attached to the cavity mounting via two Marcor holders as shown in Figure 4.9. In the experiment it was possible to transfer 20% of the atoms to the wire guide, which is about 50% of those in magnetically trappable states. This could be increased by optically pumping [Ben65] all the atoms into the low-field-seeking state which experiences the strongest trapping potential, i.e. $|F = 3, m_F = 3\rangle$.

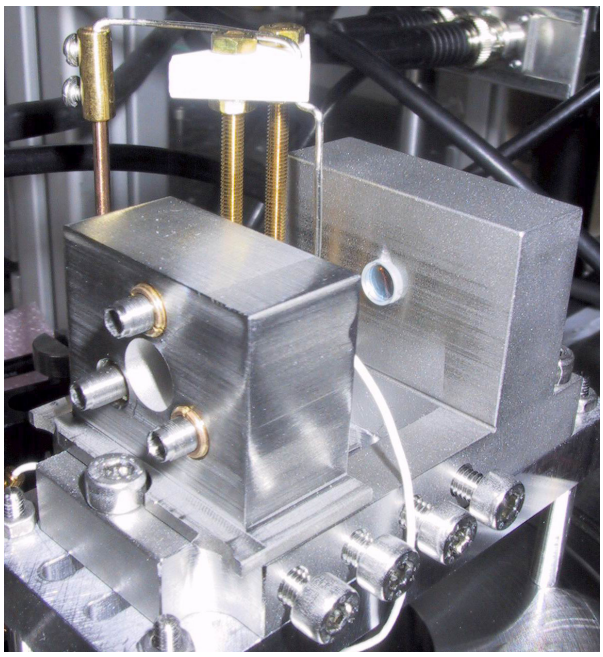

Figure 4.9: Picture of the cavity mounting. The silver wire which creates the magnetic guiding potential, is attached to the mounting by two Marcor holders.

4.5 Cavity setup

The cavity is designed to work at the quasi concentric limit at 20mm, since both mirrors have a radius of curvature of $R = 10$mm. It was possible to increase the cavity length up to 19.93mm (see Section 4.5.1). The mirrors have a diameter of 6mm and their transmission was measured to be $T = (0.9 \pm 0.1) \times 10^{-3}$ (see Section 5.1.3), which is in good agreement with the specification of $T = 1 \times 10^{-3}$. This leads to a transmission rate $\kappa_T = 2\pi \times 1.1$MHz. According to Equation 2.32 this can maximally give a cavity finesse of $\mathfrak{F} = 3500$, if all other losses are suppressed. The measured finesse was $\mathfrak{F} = 1150$. It could be shown that this originates from imperfections and dirt on the mirrors, which become become the dominating loss mechanism close to the concentric point since the area on the mirrors which is covered by the beam becomes extremely large (see Section 5.1.3). This results in a loss rate of $\kappa_{lo} = 2\pi \times 2.2$MHz.
This relatively low mirror quality, in comparison to present high finesse cavity experiments [McK04, Mau04], where mirror transmissions of $T = 4 \times 10^{-6}$ lead to finesses of 5×10^5 [Hoo01], was chosen on purpose, in order to reproduce a situation similar to the one of the first on-chip fibre cavity experiment to come. In fact, the first fibre cavities will not have better mirrors than this, if one follows the theoretical argument in Section 3.3.1, in which for an optimal detection resolution, a mirror transmission rate κ_T not higher than the cavity loss rates κ_{lo} is required. First experiences in fibre cavity fabrication [Sch04] have shown that a loss rate below $\kappa_T = 2\pi \times 1.2$MHz is not realistic in the near future.
The cavity mounting can be seen as a construction drawing in Figure 4.10 (a) and as

a photograph in Figure 4.10 (b). The mirrors are mounted on two massive aluminum blocks. One of them can be moved like a sledge with respect to the other to roughly adjust the cavity length. Fine tuning is done by three micrometer screws which also allow to align the mirror angle. During the experiment the cavity length is stabilized by a piezo below one of the mirrors. This work is described in detail in [Hoc03].

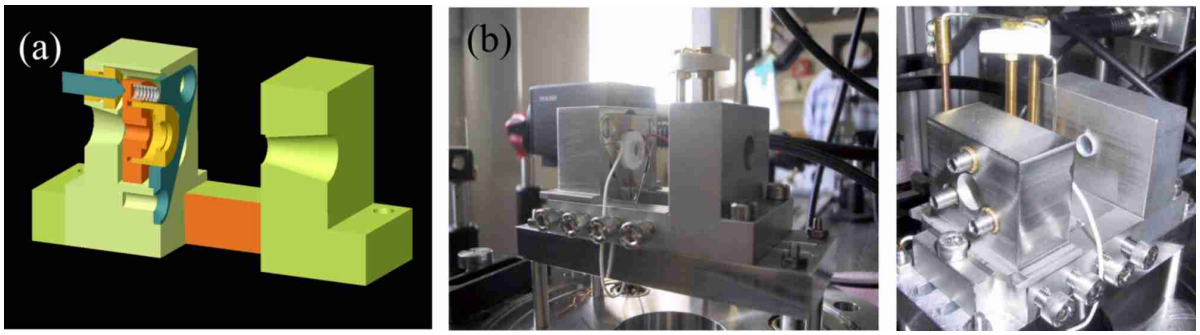

Figure 4.10: Cavity mounting, as a construction drawing in (a), and as a photograph in (b). One of the mirrors is mounted to a piezo, which accounts for the axial stabilization, the angular alignment is done by three micrometer screws

4.5.1 Stability

The operation point was chosen to be as close to the concentric point of 20mm as the alignment methods allowed (see Section 2.4.4). Stable modes could be reached up to a length of $L = 19.93$mm. The required alignment sensitivity (calculated according to Equation 2.55 and 2.56) at this point can be seen in Figure 4.11. The red curve shows the shift of the beam position on the mirror due to axial misalignment of one of the micrometer screws, causing a mirror tilt. The black curve shows the response on a transversal offset between the two mirrors.
This figure shows that the alignment accuracy and long time stability in all directions has to be on the order of 1μm. Therefore the design of the mirror mounting structures was chosen to be as robust as possible. Still the long time stability turned out to be insufficient. It was noticeable that on long time scale even the switching of the MOT coils led to a cavity misaligned. This could be due to the microsprings pressing the mirror mount against the micrometer screws. Since these screws where slightly magnetic, they moved by tiny amounts during the switching processes, which caused a misaligned to be corrected every few weeks. This realignment was quite a complicated procedure since the vacuum chamber had to be opened every time. To improve this situation a second cavity mounting was developed where the second mirror sat on a ring-piezo consisting of six sectors with six electrodes attached to them. By applying different voltages to these electrodes the piezo could be tilted. Applying a voltage difference of up to 400V between single sectors causes a displacement of $\approx 2.5\mu$m, which tilts the cavity mirror by $\approx 0.01°$. The tilting directions could be precisely chosen by addressing the electrodes individually. This was sufficient to compensate for the instability effects and allowed for

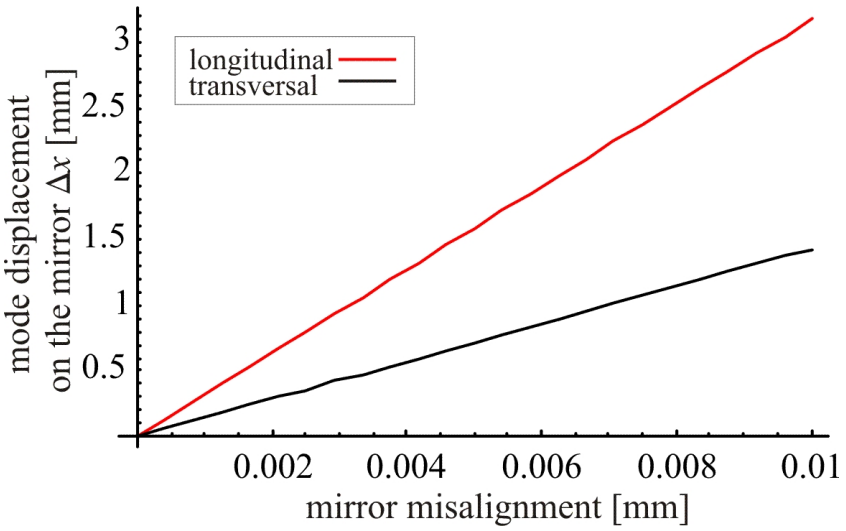

Figure 4.11: The cavity sensitivity versus mirror misalignment: the red curve shows the effect of an axial misalignment of one of the micrometer-screws, which causes a mirror tilt (2.5μm$\hat{=}0.01°$), the black curve shows the effect of a tangential offset between the two mirrors.

an in-situ realigning of the cavity axis without opening the chamber. Fears that adding another piezo would degrade the cavity stability proved to be unmotivated.

4.5.2 Locking scheme

Beside the long term stability of the cavity axis, the cavity resonance frequency has to be stabilized to the pump frequency. This is done by a technique similar to the frequency modulation lock of the laser, the Pound-Drever-Hall method (PDH)[Dre83]. As for the FM lock, the cavity pump light has to be modulated by a radio frequency. In the experiment, the modulation from the laser lock can indeed be used again. The light intensity reflected by the cavity is recorded by an APD. The frequency dependence of the cavity transmission introduces an asymmetry in the beat node between the carrier frequency and the side bands if the cavity and the pump light frequency are out of resonance. A beat note at the modulation frequency arises, whose amplitude is proportional to this frequency shift. This provides an error signal which is fed back to the piezo to control the cavity length. For details on this method see [Bla01] and for the experimental realization in this setup see [Hoc03]. A schematic picture is shown in Figure 4.12. Additionally, the locking electronics have a TTL-input which allows to break the feedback circuit and set the error signal constantly to zero as long as the TTL-input is high. This allows to leave the cavity free running during the experiment and recapture it into the lock after the experimental cycle, which typically lasts a few 100ms.

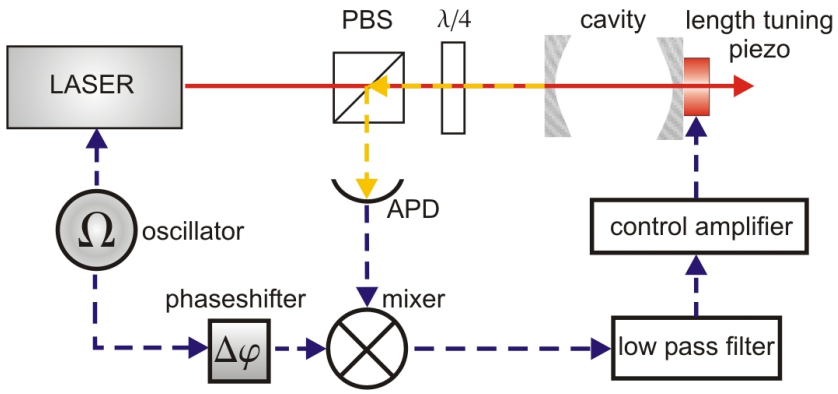

Figure 4.12: PDH lock scheme, for technical details see [Hoc03]. a quartz oscillator modulates the laser with $\nu = 20$MHz. Mixing it with the reflected light from the cavity allows to detect a beat node at the modulation frequency. A low pass filter eliminates higher order terms and the phase shifter allows to switch between absorptive and dispersive signal.

4.6 Photo detectors

The experiments with the macroscopic cavity have been used to test various detection schemes for their suitability to detect the changes in the cavity signal induced by atoms inside the mode. If one drops the maximum atom number from the MOT through the cavity, in a typical experiment the best signal-to-noise ratio can be detected when the atoms in the cavity are saturated (see Section 3.3.1). In the experiments described here this saturation happens at a transmitted powers of $\approx$ 100pW or equivalently at a photon number of $\approx 0.4 \times 10^9$ per second (see Figure 3.13). Single photon counting devices with the required time resolution to manage these numbers are still far from being commercially available [Gol01]. The situation changes as soon as the experimental sensitivity reaches the single atom level. To saturate a single atom, in the same cavity it takes $\approx$ 2pW corresponding to $\approx 8.0 \times 10^6$ photons per second. At this point single-photon counting starts to become feasible. Until then, a method has to be found to detect this amount of light without saturating, but still offering a low enough noise level at a reasonable detection bandwidth. In the following, methods that have been tested in the experiment will be briefly described.

4.6.1 Amplified Photodiode

First experiments have been performed using a fast photodiode and amplifying the photocurrent electronically. Using a gain of 10^9(V/A), for experiments with many atoms, this method offers a high enough sensitivity of $\approx$ 10pW, but limits the detection bandwidth to a few 100Hz. In order to see smaller numbers of atoms, the pump intensity has to be drastically reduced, and sensitivity as well as time resolution are insufficient, since the passage time of a single atom through a cavity of waist $w_0 = 12\mu$m is $\approx 40\mu$s and the transmission signal from a saturated atom is $\approx$ 4pW.

4.6.2 Homodyning/Heterodyning

A technique to optically amplify the signal and thus to maintain the full bandwidth is the homodyne/heterodyne detection [Aga97], already sketched in Section 3.4. In the experiment a heterodyne detector was realized as depicted in Figure 4.13.

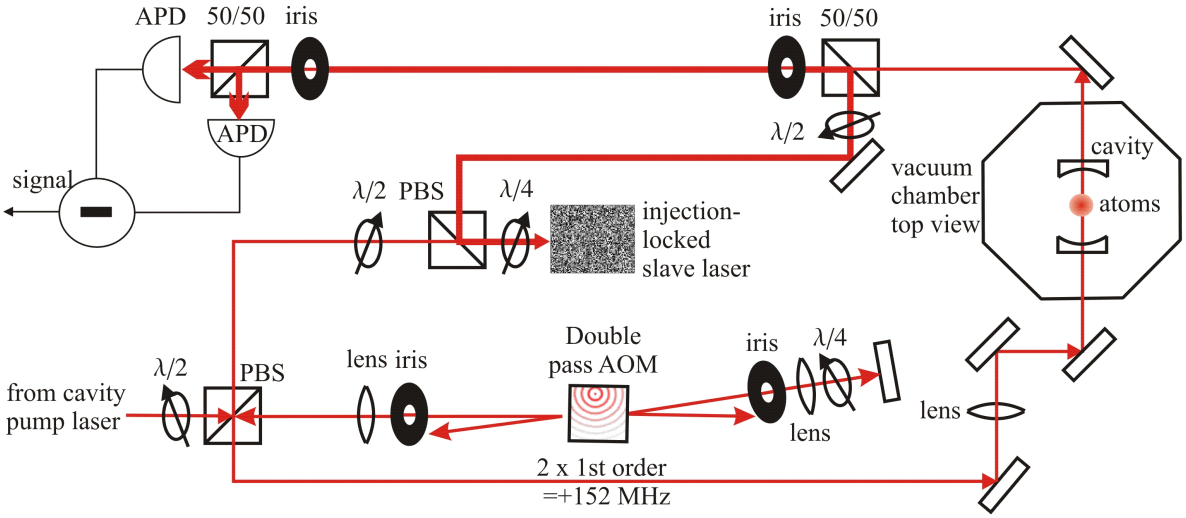

Figure 4.13: The heterodyne detection setup. A strong local oscillator, here a slave laser, is overlapped with the weak signal. Their beating signal is detected via two fast avalanche photodiodes (APD).

A small part of the pump beam is split off before the double pass AOM and is used to injection-lock a slave laser, playing the role of the strong local oscillator. Due to the double-pass AOM, there is a frequency offset of 152 MHz between slave-laser frequency and cavity pump laser. The slave laser is overlapped with the cavity transmission signal, so that a beat node at this offset frequency can be detected, from which amplitude and phase change of the light within the cavity can be extracted. Because of the offset frequency, this is rather a heterodyne detector, while for homodyning one would overlap two signals of the same frequency. To detect the phase difference between cavity transmission beam and the beam from the slave laser, the beat note is split at a 50/50 beam splitter and the light in both arms is detected using fast avalanche photodiodes (APD). Since for an off-resonant cavity the phase difference is small, by subtracting the APD signals one gets a signal proportional to the phase change induced by the atoms in the cavity. Thus the cavity transmission signal is amplified by the high amplitude of the local oscillator (see Section 3.4.1). In the case of a resonant cavity, the atom's effect on the transmission amplitude is much stronger and will overshadow the phase change. But this amplitude change can still be detected with this setup by measuring the envelope function of the beating signal. This can be realized using a simple envelope detector (see Figure 4.14), which supplies a signal proportional to the amplitude of the high-frequency beat node. One again profits from the optical amplification by the strong slave laser. This detection scheme is limited in bandwidth only by the envelope detector, which can be designed to cut off only at a few 100kHz.

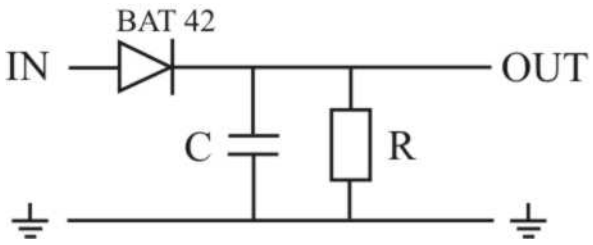

Figure 4.14: The circuit diagram of a simple realization of an envelope detector. A Schottky-diode BAT42 was used, and $R = 8\text{k}\Omega$, $C = 1.2\text{nF}$ yielded a bandwidth (given by $1/RC$) of 100kHz, which gives the envelope of the 76MHz beating signal.

Since the extraction of the signal envelope can not be done arbitrarily cleanly, the heterodyne detection is not the best method for resonant atom detection. As soon as one wants to minimize the back-action onto the atoms by detuning the cavity from the atomic resonance, however, it is the only way to detect a change in the transmission signal, since the presence of atoms will rather have an influence on the phase than on the amplitude of the light (compare Section 3.4).

4.6.3 Photomultiplier

Another possibility of low-noise amplification of optical signals is the use of a photomultiplier. In this experiment we have tested a photomultiplier tube (PMT) [1] with a quantum efficiency of $\approx 8-9\%$ at 780nm and a measured gain of 7.6×10^4. In our case this is the best choice on the way to smaller atom numbers and single atoms, since the sensitivity was below 1pW (see Section 5.4.1).

Since this device is very sensitive against any kind of stray light, the setup had to be refined in the following way (see Figure 4.15): the transmitted light was sent into a 30cm optically opaque tube, closed by a shutter. Inside it was focussed into a pinhole, made from a closed iris, and then expanded to a beam diameter of 3mm, the width of the photocathode. The PMT supply voltage of 1250V was automatically cut as soon as the cavity pump laser exceeded a certain threshold intensity.

So far, the PMT signals are quite noisy (see Section 5.4.1), but the main noise sources could be identified. Acoustic noise from the shutter, which protects the PMT from the MOT light, is acting on the focussing optics in front of the PMT. This produces a damped oscillation on top of the signal. The 70ms the atoms are falling after the MOT is switched off are not sufficient to damp out this oscillations. But this can be fixed by reducing the shutter size and by better isolating it from the optical setup. Noise directly from the PMT can be combated by shieling it against magnetic fields, which are known noise source for photomultipliers [Pay01].

[1] Hamamatsu R636-10

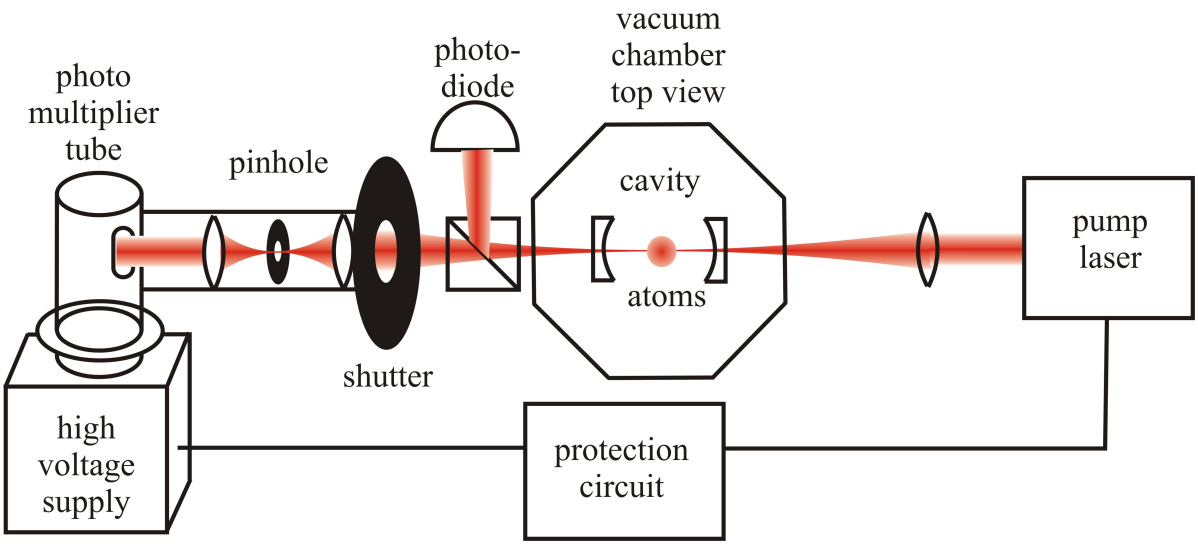

Figure 4.15: Adapted setup for the Photomultiplier: The photomultiplier was protected against stray light by a 30cm opaque tube, with a pinhole inside. A protection circuit cuts off the PMT supply voltage as soon as the cavity laser exceeded a certain saturation power.

4.7 Experimental control

The experiment is controlled by a system based on the software LabVIEW. An operation platform controls two PCI output cards, a National Instruments 6713 with 8 analogue voltage outputs @12bit, and a National Instruments 6602 with 8 digital outputs @32bit and a PCI input card (National Instruments 6035-E) with 16 analogue input channels @16bit. These channels are connected via buffers and opto-couplers (to prevent ground loops) to the experiment (for details see [Wil02]). Input and output cards are synchronized by a master pulse. The other automatically controlled experimental parameters are

Analouge	Digital
Intensity cooling beam	Masterpulse
Detuning cooling beam	Switch quadrupole coil current
Intensity repumping beam	Shutter MOT beams
Intensity cavity beam	Shutter cavity beam
Current guiding wire	Switch guiding wire
Current bias coil	Switch bias coils
Current compensation coils up/down	Cavity lock break
Current compensation east/west	Camera trigger

For different experiments, time dependent parameter sequences are saved in so-called frames. For further automation, e.g. temperature measurements, frame series can be launched. The change of global parameters has been automatized by the definition of variables that are used in various output channels at the same time. A typical control computer screen shot is depicted in Figure 4.16.

Figure 4.16: LabVIEW operation platform: The window to the left, contains all global parameters and allows to save and load settings and acquired data, the central window shows an input channel , which is analyzed in the window to the upper right to calculate the atom number from the fluorescence signal. The window to the lower right allows to edit the analog and digital output sequences.

The operation platform records one of the analog channel during the experimental cycle. During the time of alignment and optimization this is usually a calibrated photodiode looking at the MOT. From this data the atom number is calculated automatically. During the cavity experiments, the transmission signal is recorded with a bandwidth of 400 kHz, coming from one of the detectors described above. Additionally two CCD cameras [2] are detecting the atomic fluorescence from the top and from the side, just above the cavity mount. They are connected via a frame grabber to a camera computer, where a graphical interface [Ums99] allows to automatically save the picture series as bitmaps. Picture analysis is done automatically by MatLab scripts.

[2] Pulnix TM620

4.7.1 Experimental cycle

A typical experimental cycle starts with a 3s MOT-loading phase, followed by 20ms molasses phase, after the quadrupole field has been switched-off by a fast switch. Already during this MOT phase the power supply for the bias field coils is ramped up, but still disconnected by another switch. After the lasers are turned off, this switch allows to quickly ramp up the bias field and the wire current to create the magnetic guiding potential. After a guide loading phase of typically 20ms, the magnetic fields can be ramped to different values to overlap the guide with the cavity mode. To protect the atoms from stray light during the guiding phase, the cavity laser is locked to the smallest possible power. Shortly before the guided atoms reach the cavity region, the cavity laser lock is switched off, so the laser is free running during the actual experiment. Additionally, the lasers intensity is set to the desired value. After the atoms have passed through the cavity, a fluorescence image of the cloud is taken using a CCD camera and the MOT beams at resonance. After this experimental cycle, the cavity laser is recaptured by the lock and the MOT-beams and fields are switched on again.

4.8 Fibre cavity chip

While the experiments with the macroscopic cavity were performed to test the laser and cavity locking schemes and to find an optimal detection scheme, the atom chip setup with micro-optical elements was designed and fabricated. In the following the fabrication of the first fibre cavity chip will be quickly sketched.

4.8.1 Chip production

The atom chip consists of μm-sized gold wire structures and electrodes which produce magnetic and electrostatic potentials for atom manipulation. The heart of the chip production process is the lithography mask, which is structured by an e^--beam machine. All the structure information is transferred to the chip via the mask. After the mask is fabricated, a photoresist covered Si or GaAs chip is exposed to UV light through the mask. After a standard development procedure, photoresist remains only a the position of the future gaps defining the wire structures. Then gold is evaporated onto the chip and finally, remaining photoresist structures are removed by a lift-off process, which creates the small gaps between the structures. Further details about the chip fabrication process can be found in [Gro04].

4.8.2 Chip mask

The lithography mask for the first chip containing fibre-optical elements is shown in Figure 4.17.
The chip design was kept as simple as possible. In the center there is a loading section, a big Z-structure (500μm wide) with an additional U-structure (200μm-wide) on eigther

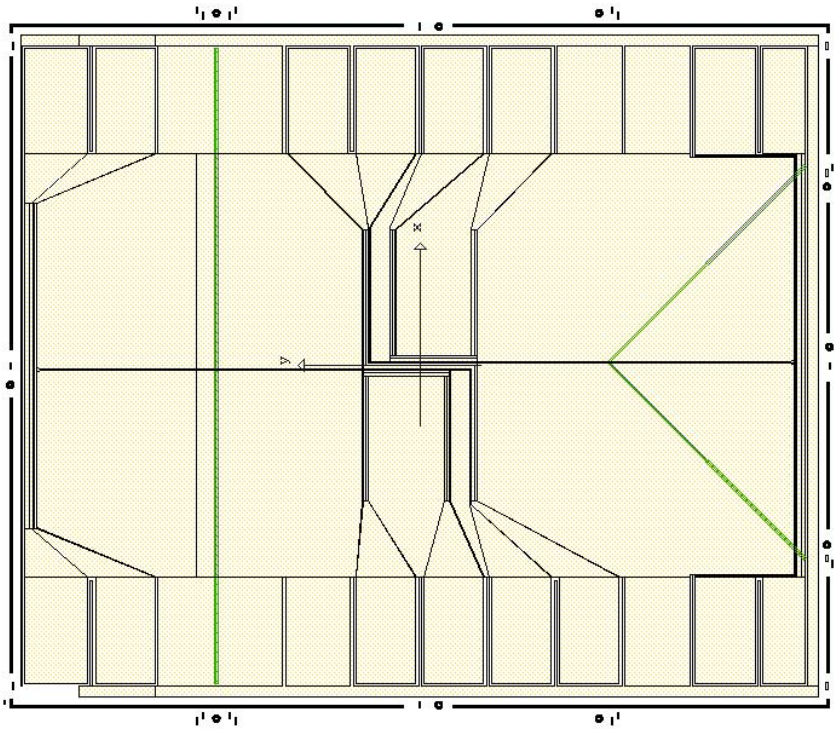

Figure 4.17: Chip mask design: from a central loading zone the atoms will be guided to the detection zones to the left and right, where the fibre optical elements are integrated

side. This allows to form Ioffe-Pritchard-like potentials with a wide range of trap parameters, including the option to strongly compress and cool the atoms into a phase space regime, where Bose-Einstein condensation can be achieved [Hof04, Kru04].
From the loading zones there are two plain 5μm-wide wire guides leading to the chip's outer ends. They will be used to transport the atoms to two detection zones to the left and to the right from the centre, where the fibre-optical elements are placed. The green lines mark these detection zones. The left side the fibre cavity setup is placed on as described in Section 4.8.4, on the right side two fibres are placed under an 90° angle for fluorescence detection (see Section 4.8.6). In the detection region no additional traps were designed in order to avoid very cold atoms being reflected by small potential variations. Such small potential distortions are unavoidably created by transversal connections to the guiding wire [Sch03]. This will be no longer a problem for future multi-layer chips, where transversal structures can lead below the guiding wire, which then should allow to retrap atoms in the detection zones.

4.8.3 Chip mounting

The chip mounting is based on a standard design developed during the 5 years since the first atom chip experiment has been performed [Fol00]. The mounting adapted to this experiment is shown in Figure 4.18.A Marcor body is placed on top of the mounting sits

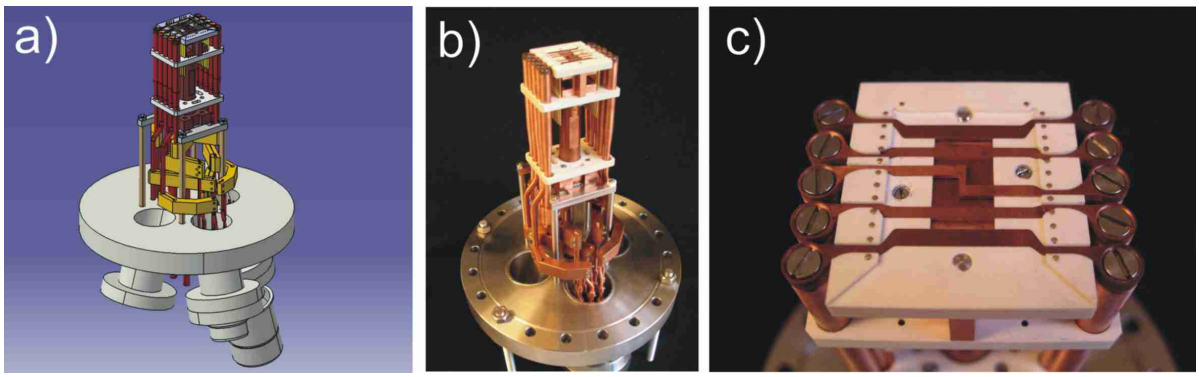

Figure 4.18: Chip mounting schematic (a), on the flange (b), the underlying copper structures (c) to create the MOT and the magnetic trap fields

, which will hold the atom chip. Copper structures in U- and H-shape are imbedded, so that the fields for a chip-MOT [Wil04] and for quadrupole- and Ioffe-Pritchard-like magnetic traps [Haa01] can be created. Big cooper rods connect these structures to high-current vacuum feedthroughs in a CF160 cluster flange, which opens up into three tubes, each closed by a CF40 flange.

The chip is glued to the marcor body, its outer electrodes are wire-bonded to pin contacts, which are connected to a 36-pin feedthrough on one of the CF40-flanges. The optical fibres attached to the chip are brought into the chamber by Swagelock Teflon feedthroughs following [Abr98], placed in the other CF40-flanges. Further details can be found in [Wil20].

4.8.4 Fibre cavities

The fibre cavities have been produced according to the concepts in Section 2.5, namely the mirrors which form the cavity are implanted into the fibres. First attempts to write these mirrors directly into the fibre in the form of Bragg reflectors have been made by shining a strong UV excimer laser through a phase grating and thus induce an index of refraction modulation [Don93, Arc93]. The mirrors produced in this way have been far too lossy, among other reasons presumably due to the fact that the grating had a 1.5μm periodicity which created second order mirrors for the 780nm light. A more successful technique was to splice the fibre, to polish both ends, to bring a dielectric layer onto one end by a transfer coating technique, and to glue the second end back to it. Two of these fibres are then mounted face to face to form a cavity. The cavity quality is optimized by successively renewing one or the other mirror until the cavity linewidth is no longer decreasing. This process is described in detail in [Sch04]. The parameters achieved for the first fibre cavity on an atom chip are shown in the following table (measured and calculated according to Section 2.5.2)

Cavity length L	12 cm	Fibre ind. of refra. n	1.5
Mode waist w_0	2.92 μm	Mode volume V_m	8.0×10^{-4} mm^3
Gap size d	6.4 μm	Add. loss κ_{lo}	$2\pi \times 9.0$ MHz
Mirror transm. T	0.01	Transm. rate κ_T	$2\pi \times 1.3$ MHz
Cavity decay r. κ	$2\pi \times 10.3$ MHz	FSR	$2\pi \times 1.3$ GHz
Finesse $\mathfrak{F}$	60	Coupling const. g_0	$2\pi \times 4.4$ MHz

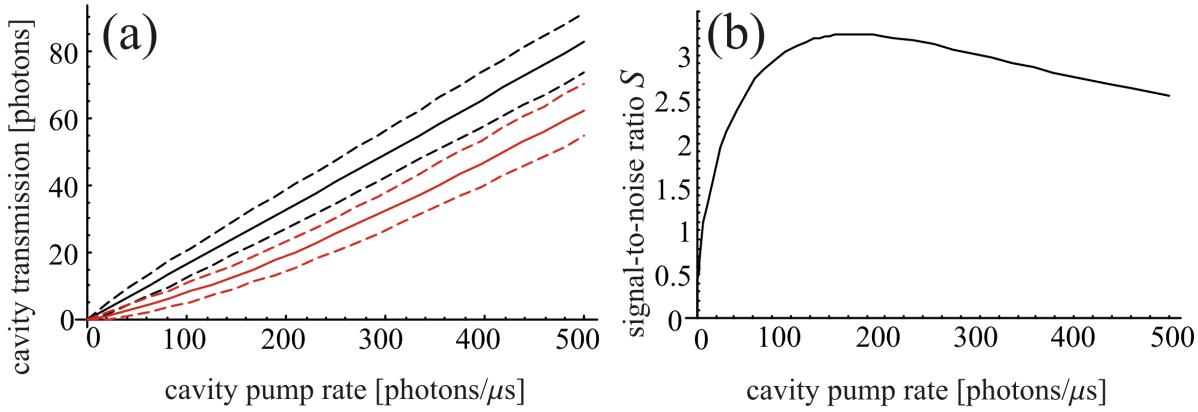

Figure 4.19: Effects of a single atoms on the cavity. Figure (a) shows the transmitted photon number within $\tau = 10\mu$s for the empty cavity (black curve) and with an atom in the cavity (red curve) as a function of the cavity pump rate. The dashed lines mark the shot noise. Figure (b) shows the resulting signal-to-noise ratio for the detection of this photon number difference as a function of the pump rate

The cavity finesse is limited by the loss rate κ_{lo}, which is much higher than the loss caused by the pure mode mismatch in the gap ($\kappa_{gap} = 2\pi \times 1.3$MHz). This can be attributed to losses in the mirrors, which are caused by the epoxy layers in between the cavity fibre and the mirror coating. To avoid this problem in next generation cavities, the transfer coating technique has to be replaced by direct mirror evaporation or by a different attempt to write Bragg grating into the fibres,e.g. by using a grating for 780nm.
Nevertheless, the theory from Chapter 3 makes a promising prediction for a cavity with parameters as in the table above. A single atoms should be resolvable with a resolution of 3σ. Figure 4.19 (a) shows the expected cavity transmission signal within an integration time $\tau = 10\mu$s of the empty cavity (black curve) and with an atom present in the mode centre (red curve). Figure (b) shows the resulting signal-to-noise ratio.

4.8.5 Fibre alignment

First ideas how to place the fibre cavity on an atom chip, led, together with the company MiLaSys [Mil05], to the development of vacuum fibre grippers. These devices hold the fibre only from above, in order to allow the fibre alignment on the chip surface (see Figure 4.20). This would have allowed to actively align one fibre with respect to the

other, monitoring the light coupled from one to the other and instantaneously gluing them to the surface.

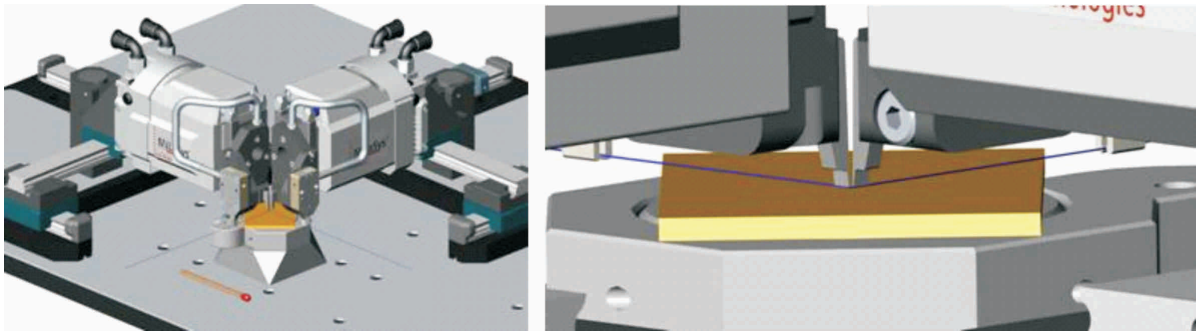

Figure 4.20: Nanopositioning motors with vacuum fiber grippers, developed together with the company MiLaSys. They hold the fibres only from above, which allows active alignment on the chip

Finally another much more elegant technique was developed. It was developed in cooperation with the University of Mannheim [Liu05]. The fibres are now passively aligned in U-shaped grooves in a photoresist layer on top of the gold surface. The atom chip with the ready-structured gold surface is spin-coated with a photoresist called SU8, which allows for very thick layers, in our case up to 100μm. This photoresist is developed through a mask patterned by optical lithography. After a lift-off procedure, U-shaped grooves, which exactly fit to the fibre size, remain on the chip. An usually unwanted imperfection even improves the alignment, since the fabrication does not produce straight walls but a small undercut, as shown in Figure 4.21.

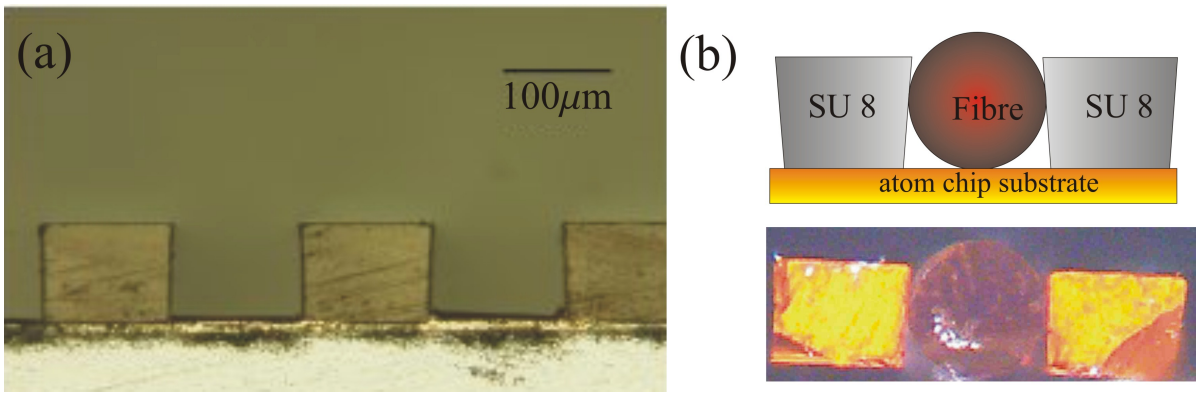

Figure 4.21: Figure (a) shows a microscope image of the fibre mounting structures, Figure (b) shows a fibre inside one of the grooves held by the undercut.

Once the fibres are pressed into the grooves, they are locked there. Extensive tests have shown that the passive alignment achieved in this way has a higher accuracy than an active alignment using a commercial nano-positioning unit. These results are shown in Figure 4.22, where the fibre cavity finesse is plotted as a function of the gap size between the two fibres.

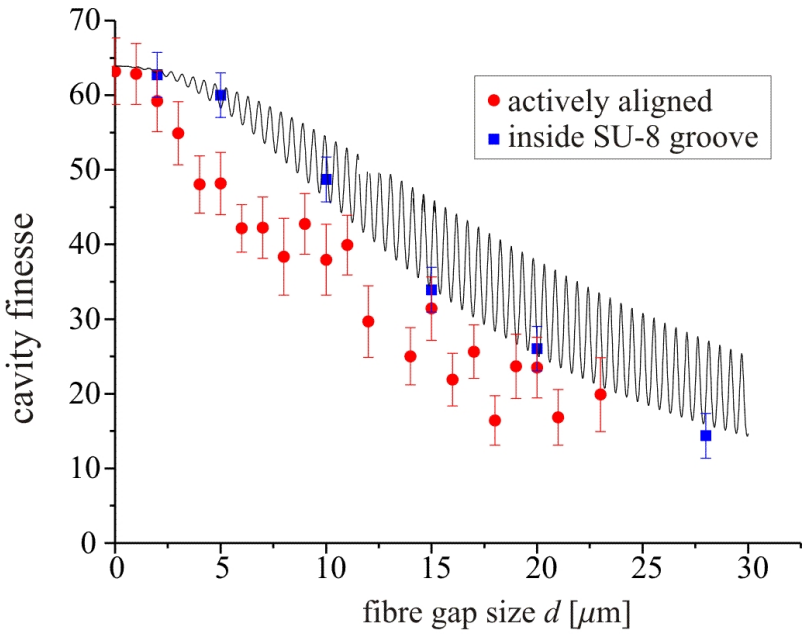

Figure 4.22: Measured cavity finesse as a function of the gap width. The red points show an actively aligned cavity, the blue points a cavity where the fibres are sitting in the alignment grooves. The theoretical curve is calculated from the model in Section 2.5.2

The red points correspond to an actively aligned cavity, the blue points to a cavity, where the fibres are located in the alignment grooves. The theoretical curve is calculated from the model in section 2.5. The oscillations reflects the geometry of the fibre cavity, where boundary conditions have to be matched at the cavity mirrors and the fibre endcaps (see Section 2.5.2).

4.8.6 Other fibre optical elements

Besides this fibre cavity setup, two other experiments are planed to be performed with the first fibre chip. At the same detection zone as the cavity (see Figure 4.17) a tapered and lensed single-mode fibre is placed into an alignment groove. It produces a focus at 40μm with a waist of 2.5μm. Its focal point is overlapped with the centre above the guiding wire, so that is allows to excite traversing atoms very efficiently. The light is collected by a second, multi-mode fibre in an alignment groove one the other side of the wire (see Figure 4.23 (a)). In this way it should be possible to detect an absorbtion signal of atoms, which scatter light from the excitation beam.

Another tapered and lensed fibre of the same kind is placed in one of the angled grooves at the other detection zone. It is used to resonantly excite the guided atoms. Now the fluorescence light is collected by a second, multi-mode fibre placed under a 90° angle in a groove at the other side of the guiding wire. This angle between excitation and detection fibre avoids direct illumination by the excitation beam.

The completely mounted chip with the integrated fibre optical elements described above

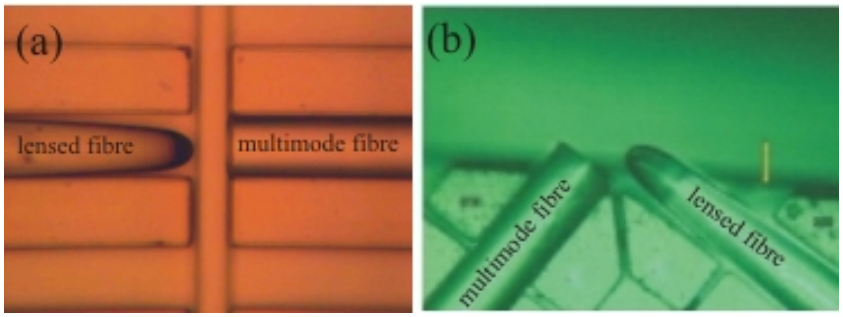

Figure 4.23: Beside the fibre cavity, two other fibre experiments are placed on the chip. Figure (a) shows a microscope image of an absorbtion detection setup, Figure (b) the fibres for fluorescence detection.

can be seen in Figure 4.24. The fibre mounting structures can be identified by their light scattering in comparison to the otherwise perfectly reflecting gold surface.

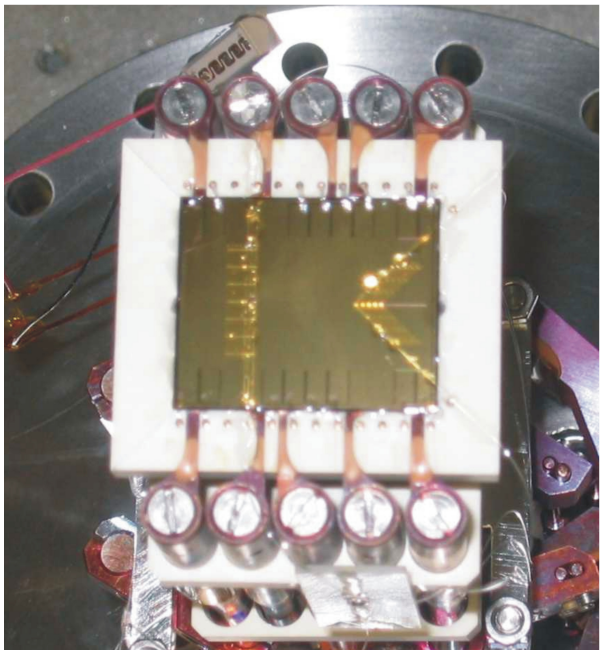

Figure 4.24: The completely mounted chip with integrated fibre optical elements.

5 Cavity signals

In this chapter the experimental results will be presented. Section 5.1 describes methods to precisely determine the cavity parameters, in Section 5.2 the cavity is used to determine the properties of the free falling atom clouds and the detection sensitivity of the cavity is explored. In Section 5.3the detection of magnetically guided atoms is reported and the guiding potential is used to align the position of the atoms with respect to the cavity mode. In Section 5.4 various methods to detect the cavity transmission signal are compared.

5.1 Cavity characterization

When the cavity was assembled, two important quantities had to be measured accurately to decide whether it is suitable for experiments with cold atoms. The first is the cavity length, which has to be extremely well known, especially close to the concentric point, as the single-atom coupling constant critically depends on it 2.4.4. Secondly the finesse as a measure of the cavity loss rate is important, since for optimal atom detection conditions the theory has predicted constraints on these loss rates (see Section 3.3.1).

5.1.1 Length measurement

The length of the cavity was determined by the following method: the mode matching optics was slightly misaligned in one spatial direction, which leads to an increase of the higher order transversal modes (in this direction) in the spectrum (see Figure Figure 5.1 (a)). For a perfectly mode matched pump beam these modes are strongly suppressed. In this way the cavity length can be quantified by measuring the relative positions of higher-order transversal resonances of different axial mode numbers (the index j in Equation 2.29) and by comparing them, using the resonance condition in Equation 2.29. A measurement with MHz accuracy corresponds to a spatial precision of micrometers. Close to the concentric point, the spectrum becomes very clear. The modes with the same axial mode numbers j now unravel and string in the right order next to the ground mode as shown in Figure 5.1 (b). This simplifies the identification of the modes, furthermore it is now possible to determine the cavity length with micrometer precision by simply counting the number of higher order modes within one free spectral range (between two ground modes). In Figure 5.1 (a) there are 27 mode within one FSR which translates to a cavity length of 19.934 ± 0.002mm.

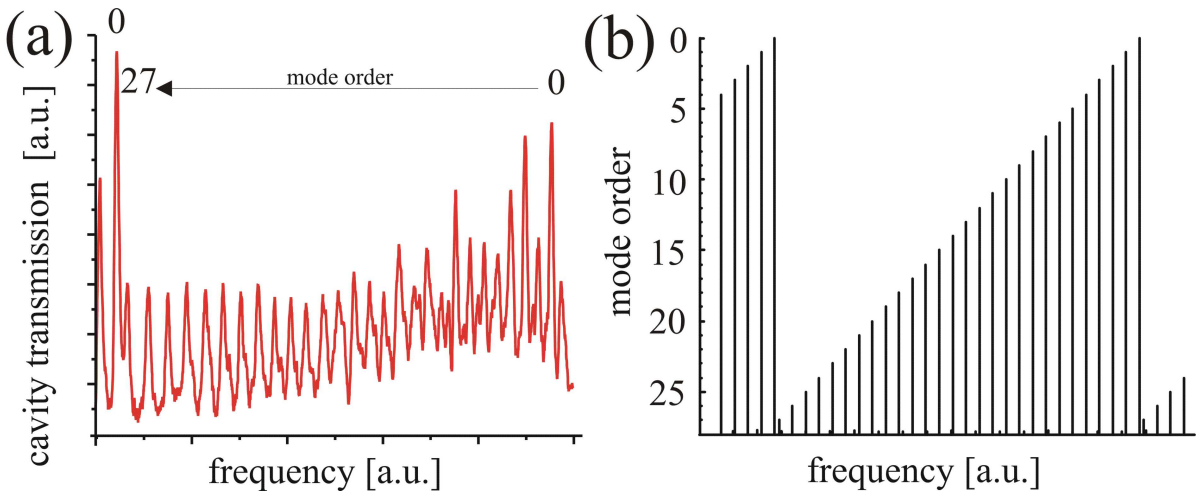

Figure 5.1: The cavity spectrum used to determine the length: Figure (a) shows the measured spectrum over one full spectral range, Figure (b) shows the calculated resonance frequencies.

5.1.2 Finesse measurements

To measure the finesse of a cavity, a well established method is the so-called ring-down measurement [Kee88, Rem92], where the decay of the cavity field is monitored after switching of the pump beam. This allows to directly measure the decay rate κ, which, given the free spectral range, determines the finesse

$$\mathfrak{F} = \frac{FSR\pi}{\kappa} = \frac{c}{2L}\frac{\pi}{\kappa}. \tag{5.1}$$

In our case the decay rate is quite high, on the order of a few MHz. These measurements would require a high time resolution. Thus it is more convenient to use an alternative method: By tuning the cavity length over the pump laser resonance the resonance linewidth can be measured. The necessary frequency calibration is done by using the rf-sidebands as frequency markers. The sidebands are modulated on the pump beam for the laser and cavity lock (see Section 4.2.1). By increasing the rf-modulation depth on the laser, the sidebands become visible in the cavity length scan as shown in Figure 5.2. The modulation frequency can be precisely measured on a spectrum analyser, which allows to calibrate the frequency axis in the scan. In Figure 5.2 the cavity length was $L = 19.93$mm. The full width at half maximum $\Delta\nu$ of the fitted Gaussian curve determines the loss rate κ:

$$\frac{\kappa}{\pi} = \Delta\nu = 6.5\text{MHz}, \tag{5.2}$$

which yields a cavity finesse of $\mathfrak{F} = 1160$.

5.1.3 Finding an appropriate cavity length

Since an experimental goal was to minimize the cavity mode waist and thereby increase the atom-light coupling, in order to simulate the conditions in a fibre resonator, the

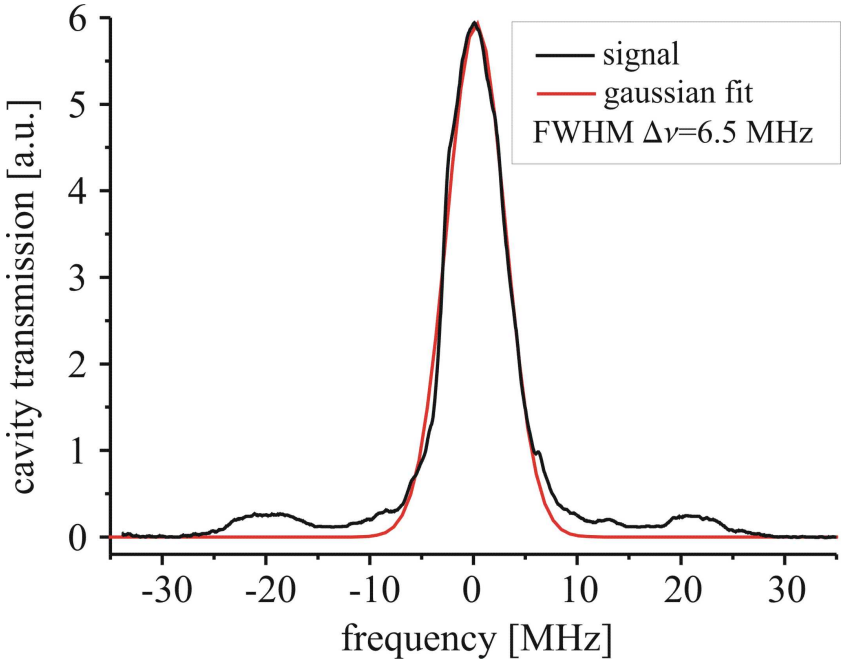

Figure 5.2: Cavity finesse measurement by evaluating the linewidth of the resonance curve. The rf-sidebands at ±20.2MHz serve for frequency calibration.

cavity operation point had to be chosen as close as possible to the concentric limit (see Section 2.4.4). On the other hand, a stable operation is necessary, with a loss rate not much larger than the mirror transmission rate, as required for optimal atom detection (see Section 3.3.1). Therefore, the finesse was measured repeatedly, as the cavity length was increased. The results are shown in Figure 5.3.
Beyond a certain cavity length, the finesse starts to drastically drop. To analyse the origin of this drop, the data points have been fitted by a finesse function with a cavity loss factor which is proportional to the beam cross section on the mirror compared to the confocal case $(w_\mathrm{m}/w_\mathrm{m,conf})^2$:

$$\mathfrak{F} = \frac{2\pi FSR}{2(\kappa_T + \kappa_{lo})} = \frac{\pi}{T + lo\left(\frac{w_\mathrm{m}}{w_\mathrm{m,conf}}\right)^2} = \frac{\pi}{T + \frac{lo}{\sqrt{1-g^2}}}, \tag{5.3}$$

with the cavity parameter $g = 1 - L/R$. The maximum finesse is reached at the confocal point ($L = R$). For perfectly reflecting mirrors (T=0), one finds

$$\mathfrak{F}_\mathrm{max} = \frac{\pi}{lo}. \tag{5.4}$$

Expressing the finesse in terms of T and $\mathfrak{F}_\mathrm{max}$ will gives the function that is fitted to the data points in Figure 5.3

$$\mathfrak{F} = \frac{\mathfrak{F}_\mathrm{max}}{\mathfrak{F}_\mathrm{max}\frac{T}{\pi} + \left[1 - \left(1 - \frac{L}{R}\right)^2\right]^{-1}}. \tag{5.5}$$

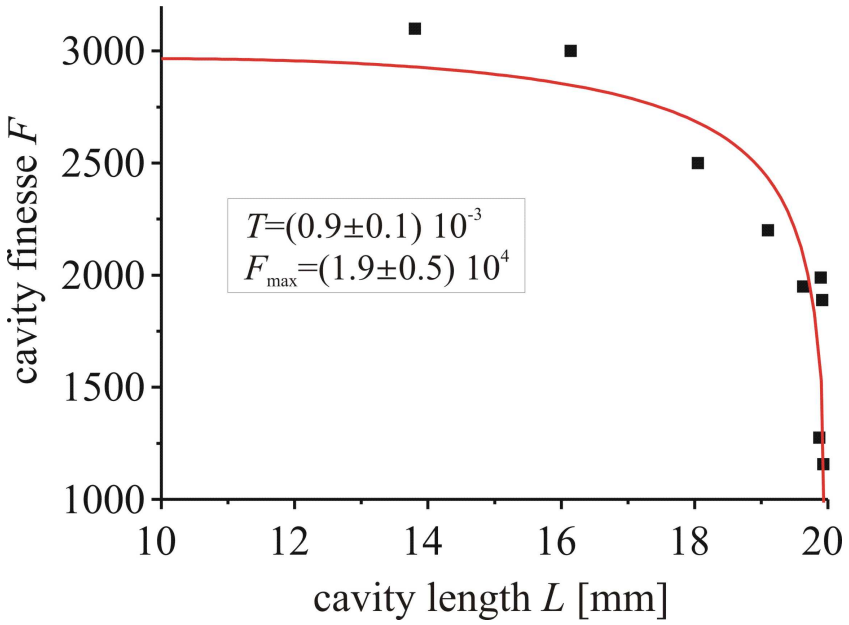

Figure 5.3: The figure shows finesse measurements for different cavity lengths. A finesse function with a loss factor proportional to the beam cross section on the mirror is fitted to the data. The mirror transmission is determined from the fit to be $T = 0.9 \times 10^{-3}$.

Figure 5.3 shows that this function fits the data fairly well, which leads to the conclusion that the losses are dominated by an effect which scales like the spot size on the mirrors. This can be effects due to surface roughness. Such roughness gives rise to small angle divergences for the backreflected light, which causes a mode mismatch and therefore losses.

The mirror transmission, which was left as a fitting parameter was found to be $(T = 0.9 \pm 0.1) \times 10^{-3}$. This is in perfect agreement with the specification of the manufacturer of $T = 10^{-3}$. The cavity mirror transmission rate then results in $\kappa_T = 2\pi \times 1.2\text{MHz}$.

A direct way to determine the mirror transmission, is described in [Hoo01]. It involves measuring both, reflected and transmitted signal of the cavity. For our purposes the result of the extrapolation is sufficient.

As the cavity operation point, the length $L = 19.93\text{mm}$ was chosen, just before the finesse breaks down. At this length, a finesse $\mathfrak{F} = 1160$ was measured. Taking the mirror transmission rate into account, this amounts to an additional loss rate $\kappa_{lo} = 2\pi \times 2.0\text{MHz}$. The maximum coupling constant of such a cavity according to Equation 3.38 results in $g_0 = 2\pi \times 3.0\text{MHz}$. The mode waist at the chosen cavity length is $w_0 = 12.1\mu\text{m}$ and the overall mode volume becomes $V_m = 2.3 \times 10^{-3}\text{mm}^3$. This is the limit of this macroscopic setup. Still, the expected mode waist of a fibre cavity as described in Section 2.5.2 will be $2.9\mu\text{m}$, which would yield gain factor of 4 in the single atom cooperativity parameter, determining the single atom detection efficiency (see Section 3.3.1).

Early experiments described in this work have been performed with another cavity mirror charge, where the equivalent measurements gave a mirror transmission of $T = 1.8 \times$

10^{-3} as described in [Hoc03]. The cavity length was then chosen to be $L = 19.86$mm, corresponding to a waist of $w_0 = 14.4\mu$m. At this length a finesse of $\mathfrak{F} = 410$ was measured. The cavity parameters were $(g, \kappa_T, \kappa_{lo}) = 2\pi \times (2.5, 1.1, 7.1)$MHz. For some of the measurements presented here the finesse dropped even below a value of 410 due to long time instabilities as described in Section 4.5.1. Nevertheless, as predicted in Chapter 3 even these cavity parameters should still allow for single atom detection, if one could position an atom into the centre of the mode where the coupling constant is maximal. But with a system of many atoms, where the single atomic positions are not controllable to that extent, one has to drop a fairly high number of atoms ($\approx 10^6$) to reach an effective atom number of 1 in the cavity mode, as discussed in Section 3.5.

5.2 Free falling atoms

First experiments have been carried out with free-falling atoms. The atoms have been loaded and cooled in a MOT, which finally was shifted to the right position above the cavity to drop the cloud. The time needed by free falling atoms to traverse the distance of $\approx$ 2cm to the cavity was $\approx$ 65ms. The first detected signals from atoms falling through the cavity are shown in Figure 5.4. The red curve shows the gaussian shaped dip, the black curve, for comparison, shows the same experimental cycle, but with the quadrupole coils switched off, which inhibits the loading of a MOT.

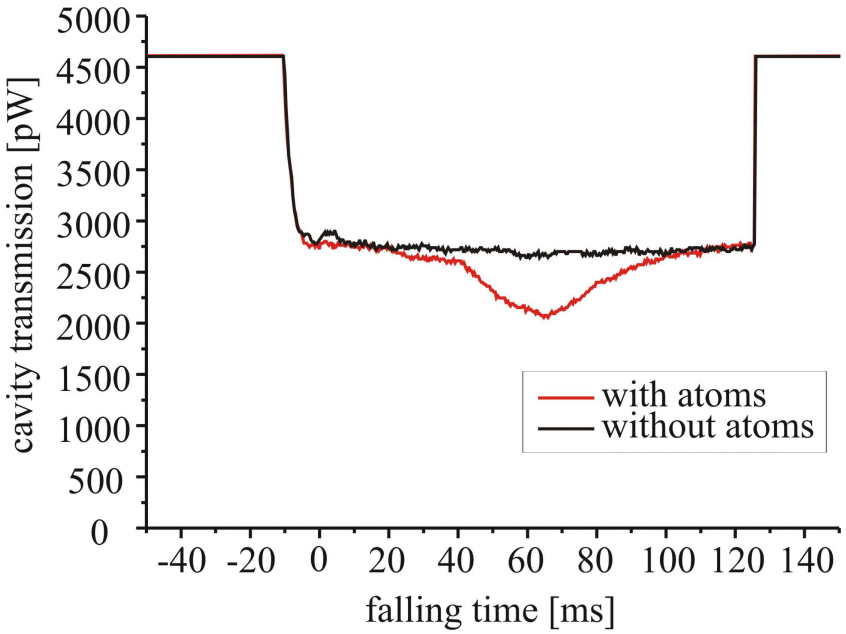

Figure 5.4: First signal from an atomic cloud passing the cavity, when the atoms are dropped at $t = 0$ the cavity is switched to the desired pump intensity, the passing atoms produce a gaussian dip in the signal (red curve). The black curve shows for comparison the same experiment when the MOT fields stay off, i.e. the cavity transmission signal in absence of atoms.

In the experiment shown in Figure 5.4 a cloud of 2.3×10^6 atoms was dropped from

a MOT into a cavity of $L = 19.86$mm and $\mathfrak{F} = 410$. After a free fall of 64ms, the cloud, which has ballistically expanded to a width $\sigma \approx 4.3$mm, reaches the cavity mode. Following the method in Section 3.5, the overlap integral between atomic distribution and cavity mode function can be calculated to determine the effective atom number in the mode, corresponding to the atom number that couples with the maximum rate of $g_0 = 2\pi \times 2.5$MHz to the cavity field. For the given parameters this was $N_{eff} \approx 2$.

5.2.1 Temperature

The cavity signal can be used to analyse the distribution of the falling atoms, e.g. to determine their temperature.

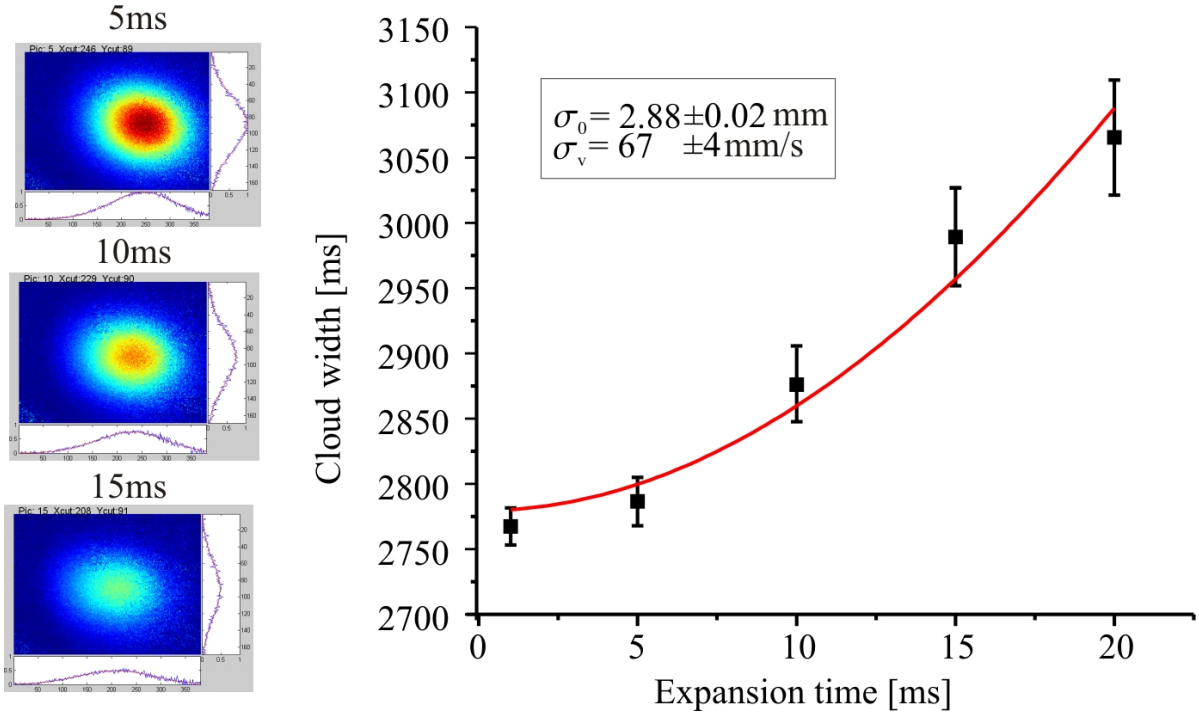

Figure 5.5: A typical temperature measurement: the freely expanding atoms are imaged by a CCD camera and the function 5.6 is fitted to the cloud. The temperature is given by the mean thermal expansion velocity, in this case $\sigma_v = 62$mm/s, which corresponds to $T = 39\mu$K

.

The conventional method to measure the atomic temperature is time-of-flight imaging of the atomic cloud using a CCD camera. The atom's velocities obey a Maxwell-Bolzmann distribution which in the quasi-harmonic potential of the MOT can be described by Gaussian functions in real space as well as in velocity space. The atoms released from the MOT are then expanding according to

$$\sigma(t) = \sqrt{\sigma_0^2 + \sigma_v^2 t^2}. \tag{5.6}$$

Here σ_0 is the initial width of the cloud and σ_v the width of the velocity distribution. The cloud's temperature is given by

$$T = \frac{M\sigma_v^2}{k_\mathrm{B}}, \tag{5.7}$$

with k_B the Boltzmann constant and M the atomic mass.
The result can now be compared with a method, in which the cavity signal is used to determine the width of the atomic distribution. Assuming that the atoms fall freely in the gravitational field, the cloud centre moves according to $x_c(t) = \frac{g}{2}t^2$. The two times, when the two flanks of the cloud are passing the cavity, can be translated into a cloud width. This allows to calculate the thermal velocity of the atoms. The width of the velocity distribution is given by

$$\sigma_v = \frac{\sqrt{(gt_c\sigma_t)^2 - (\sigma_0)^2}}{t_c - \sigma_t}, \tag{5.8}$$

where σ_0 is the initial width of the cloud, t_c the time the cloud centre passes the cavity, and σ_t the width of the cavity signal on the time axis. This measurement has been

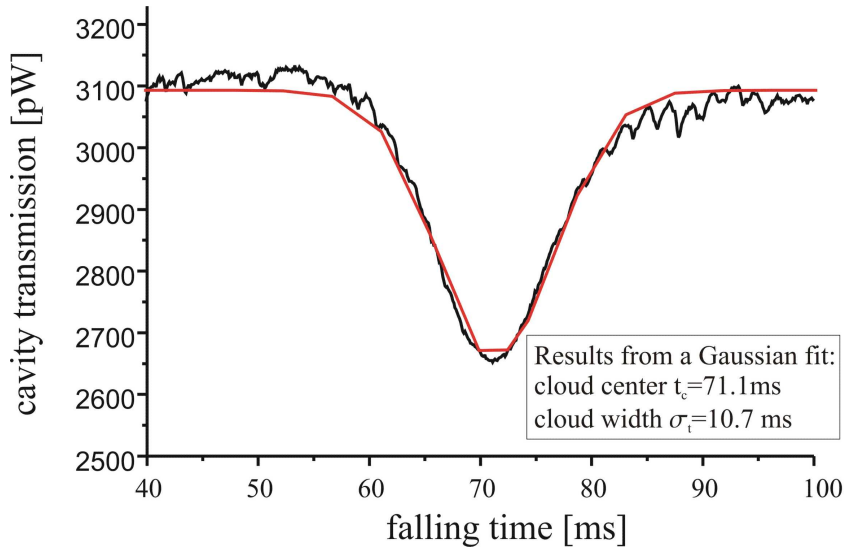

Figure 5.6: A Gaussian fit to the time-dependent cavity signal allows to calculate the temperature of the falling cloud, in this case it $\sigma_v = 0.051$mm/s corresponding to 27 μK

performed in parallel to the measurements in Figure 5.5. From a Gaussian fit to the atomic dip in the cavity absorption signal as shown in Figure 5.6, the mean velocity was determined to be $\sigma_v = 0.051$mm/s, which agrees sufficiently well with the width of the velocity distribution $\sigma_v = 0.062$mm/s, obtained by time of flight imaging.

5.2.2 Atom number

Another goal of the experiments was to determine the absolute number of atoms interacting. Measurements of the cavity transmission have been performed for varied cavity

pump power. A typical result is shown in Figure 5.7. Figure 5.7 (a) shows the low saturation regime measured with a photomultiplier, Figure 5.7 (b) shows the high saturation curves measured with a photodiode.In this experiment a MOT containing 1.5×10^7 atoms at a temperature $T = 60\mu$K was dropped into a cavity of $L = 19.93$mm.

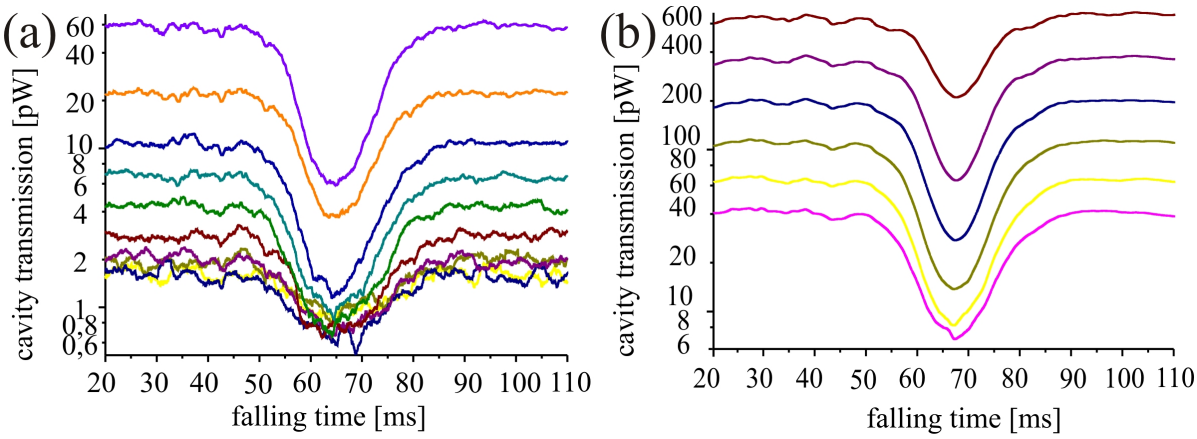

Figure 5.7: The plots show the change of the cavity transmission signal induced by a MOT of 1.5×10^7 atoms being dropped into the cavity. Figure (a) shows the low intensity measurements with the photomultiplier. The background level was determined from measurements with a closed shutter to be on average 0.7pW. Figure (b) shows measurements at higher intensities with a photodiode, the relatively high background (respectively amplifier offset) of 80pW has already been subtracted.

The measurements have been performed in two pump power regimes. For the regime, where the empty cavity transmission signals were below 10pW, the photomultiplier described in Section 4.6.3 was used. Further details about this detection method can be found in Section 5.4.1. Above the saturation limit of the photomultiplier, with $P_{out} = 10 - 500$pW an amplified photodiode was used. Both devices have been calibrated, but to make sure that the two measurements can be compared to each other and with the theory, the relative drop of the transmission signal must be considered.
Before being able to compare the predictions of the theory to the measured signal, an important adaptation has to be made. The generalization of the theory for many atoms as performed in Section 3.5 was restricted to the low saturation regime. For pump powers around 10pW, the atomic transitions start to saturate (compare Figure 3.13). This means that the non-linear term $2g(\vec{r})^2N$ in the equation for the intra-cavity photon number 3.30 is no longer negligible compared to the atomic decay rate Γ. Since the coupling constant $g(\vec{r})$ cannot be assumed to be constant for all atoms, an effective coupling constant will be introduced. It is the maximum coupling constant reduced by a constant factor: $g_{\text{eff}} = p\, g_0$. The more the atomic cloud is spread, over regions far away from the cavity waist, where the cavity field strength is low, the smaller p becomes. This adaptation provides an empirical improvement to the theory. The effective coupling constant g_{eff} is obtained from a fit to the experimental data and is basically determind by the cavity intensity for which saturation sets in. This manifests itself in a drop in the relative absorption signal height.

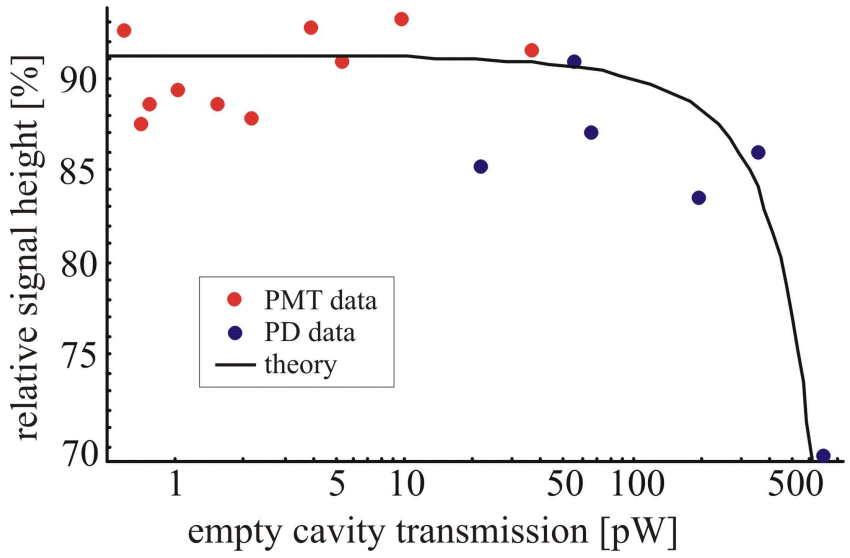

Figure 5.8: The Figure shows the relative drop in the cavity transmission signal due to the atoms in the cavity. The theory was fitted to the experimental data with atom number and effective coupling constant as fit parameters.

The relative drop in the cavity transmission is evaluated for different cavity pump power. Figure 5.8 shows the result, the red data points correspond to the low saturation measurements with the photomultiplier, the blue points to the high saturation measurements performed with the photodiode. By fitting the theoretical model to this data, the effective coupling constant is determined to be $g_{\text{eff}} = 0.1g_0$. The only other free parameter in this fit is the total atom number in the cloud, which yields $N_a = 4\times10^6$ in this case. This number is a factor of 4 away from what was measured in the MOT $N_{MOT} = 1.5 \times 10^7$. The apparent losses occur most likely during the fall of the cloud. These numbers result in an effective atom number in the mode of $N_{\text{eff}} = 2.5$.
The theoretical transmission curves calculated with these parameters are shown in Figure 5.9. The pump powers in Figure 5.9 (a) and (b) correspond to those in Figure 5.7 (a) and (b). The comparison of these figures shows that the experimental results and the theoretical predictions present very similar time variations.

5.2.3 Sensitivity of the cavity

One of the key experiments was to determine the minimum number of atoms the cavity could resolve. Therefore the MOT atom number was reduced, by decreasing the Rb-dispenser current.
A cloud containing 1.7×10^6 atoms was dropped under the same experimental conditions as above. Figure 5.10 shows the cavity transmission signals for different pump powers, again the low power regime in Figure (a) and the high power regime in Figure 5.10 (b). A theoretical curve is fitted to the maximum relative signal as shown in Figure 5.11. The fit gives a total atom number of $N_a = 0.94 \times 10^6$, which is again comparable with

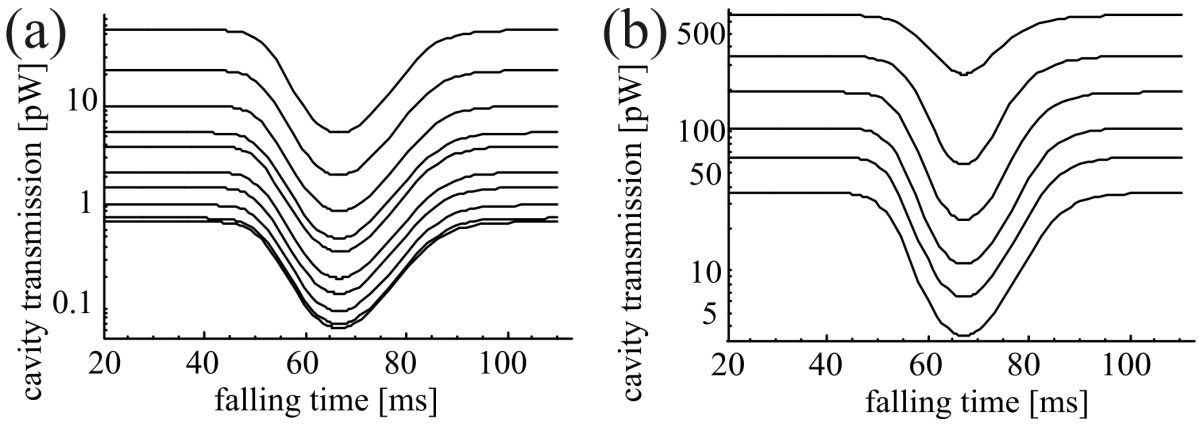

Figure 5.9: Cavity transmission signals which are predicted by the theory for pump intensities corresponding to those in Figure 5.7 for the PMT measurements in (a) and the PD measurements in (b).

the estimate from the fluorescence detection within the MOT, if one assumes about 50% losses during the fall. The effective coupling constant was found to be $g_{\text{eff}} = 0.22g_0$, which is by a factor of 2 higher than in the previous case. This reflects the fact that the saturation sets in at smaller intensities. One possible explanation could be that the cloud size was smaller so that a higher percentage of the atoms is concentrated in regions with strong coupling close to the cavity mode waist. Due to the rather long falling time this would be possible, only if the atoms were colder. The effective atom number in the mode is found to be $N_{\text{eff}} = 0.64$.
Figure 5.12 shows the transmission signal calculated from this fit parameters which again agrees well with the experimental data in Figure 5.10 as long as the latter are above the noise level.
Another attempt was made to further reduce the atom number in the MOT to 3.5×10^5. The results are shown in Figure 5.13 (a). In the photomultiplier measurements for most of the pump intensities the atom number is masked by the signal fluctuations. Only over a very small region of pump powers the signal can be resolved by extremely smoothing the data (adjacent averaging over 10ms time intervals). This means one can clearly state that the sensitivity limit was reached.
The attempt to fit a theoretical curve to the strongly fluctuating relative signal heights shown in Figure 5.14 gives a total atom number in the cloud of $N_a = 1.1 \times 10^5$ which is not too far of from what was measured in the MOT. The effective coupling constant was found to be $g_{\text{eff}} = 0.63g_0$ which is again higher than the ones previously found. This results in an effective atom number in the mode of $N_{\text{eff}} = 0.07$.
The fit parameters are based on very small signals and thus not as exact as the ones for higher atom numbers, but the mere fact that one can identify a drop in the cavity signal when the atomic cloud is passing, justifies the statement that the sensitivity limit of the cavity was found. The corresponding effective atom number in the mode is less than 0.1.
In conclusion, a fibre cavity of the same parameters would clearly be suitable as a single

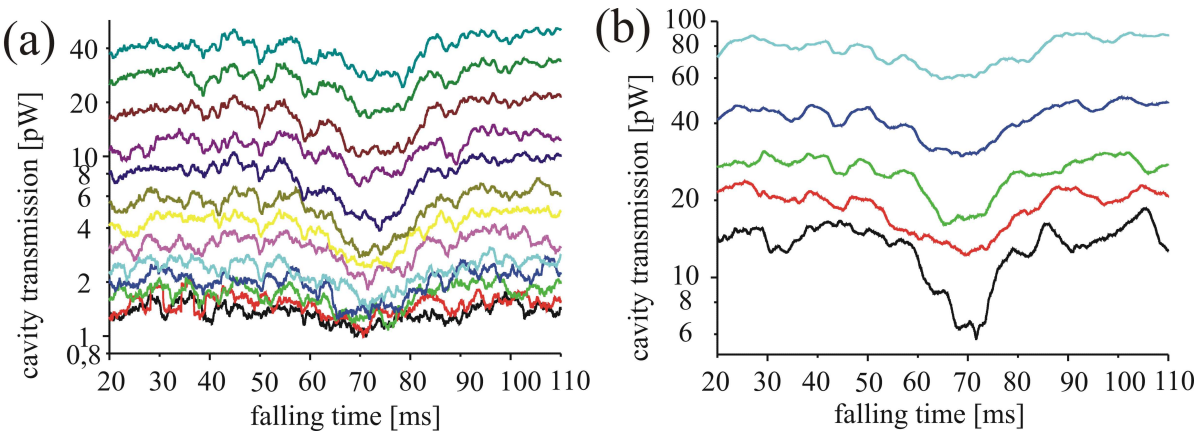

Figure 5.10: Cavity transmission signal from a cloud of 1.7×10^6 atoms being dropped into the cavity. Figure (a) shows the photomultiplier measurement for low intensities. The background level was determined from measurements with a closed shutter to be on average 1.0pW. Figure (b) shows measurements at higher intensities with a photodiode, the relatively high background (respectively amplifier offset) of 81pW has already been subtracted.

atom detector. This holds, if one manages to place one atom into the waist of the mode, where the coupling constant is maximal (see Section 5.6). If a system allows to place the atoms there deterministically one by one, also step-like changes in the transmission signal should be observable. This was not possible in this experiment, since there was no way to control the atom positions and the atomic density to this extend. Here, the signal arises from many weakly coupled atoms, which have the same influence on the cavity field as 0.1 atoms in the mode waist would have.

5.3 Magnetically guided atoms

A more controllable way to bring the atoms towards the centre of the cavity mode is loading them into the magnetic guide, which was part of the setup (see Section 4.4).

5.3.1 Guide loading

After switching off the MOT light, the guide is loaded by ramping up the current in the guiding wire together with a homogeneous bias field. This creates a quadrupole-like potential for the low-field seeking atomic states, which can be guided through the cavity mode (see Section 4.4). The optimal loading parameters have been found at the maximum achievable bias field of $B_{\text{bias}} \approx 10$G, produced by a bias coil current of 7.5A, and the maximum achievable wire current of 33A.
In a wire guide, the trap depth is ideally given by the magnetic moment times the magnetic field μB_{bias} [Den99]. But in reality, the measured trap depth for the state with strongest magnetic dipole moment $|F = 3, m_F = 3\rangle$, given in terms of an atomic temperature of $T_{trap} = 580\mu$K, slightly deviates from the value given by the bias field,

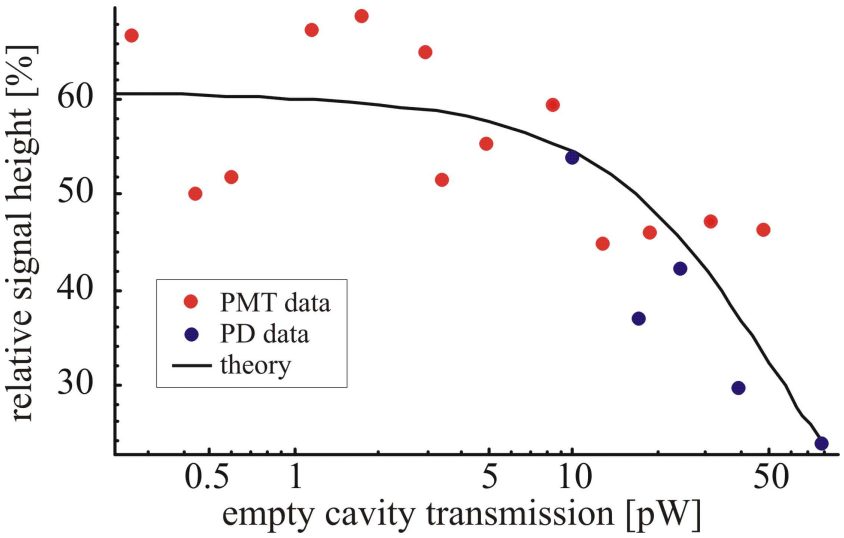

Figure 5.11: Relative drop in the cavity transmission signal due to the atoms. The theory was fitted to the experimental data with atom number and effective coupling constant as fit parameters.

as discussed in Section 4.4. The trap position is given by the position of the potential minimum

$$r_{min} = \frac{\mu_0}{2\pi}\frac{I_{wire}}{B_{\text{bias}}} = 6.4\text{mm}. \tag{5.9}$$

The fact that the best loading is obtained by the maximizing bias field and wire current is reasonable, since these parameters provide the largest possible trapped phase space volume. Furthermore, it is favourable for matching the magnetic trap to the MOT, which is operated as far as possible away from the shadows, the wire and its mounting cast in the laser beams (see Figure 4.9).

The picture series in Figure 5.15 shows the loading of the magnetic guide. At $t = 0$ the MOT beams are switched of and the magnetic fields are ramped up, which quickly repels the high-field seeking atoms. After 15ms one starts to see the slow splitting of the remaining atoms into a free-falling fraction in the magnetic-field insensitive $m_F = 0$ states and the magnetically guided atoms in the low-field seeking states. After 65ms the guided cloud reaches the cavity mode. The intensity of the first picture cannot directly be compared to the others, since there the atoms are still imaged with all the six MOT beams on, while after 5ms the atoms move into the shadow of the cavity mounting, which blocks the 4 horizontal beams.

From Gaussian fits to the free falling atoms and to the magnetically trapped cloud a loading efficiency of 20% of the atoms from the MOT is measured. This is about 50% of the fraction of atoms in the low-field seeking states, which would theoretically be magnetically trappable. For experiments where a large atom number is of importance, this theoretical limitation could be overcome by optical pumping all atoms into the highest low-field seeking state [Ben65].

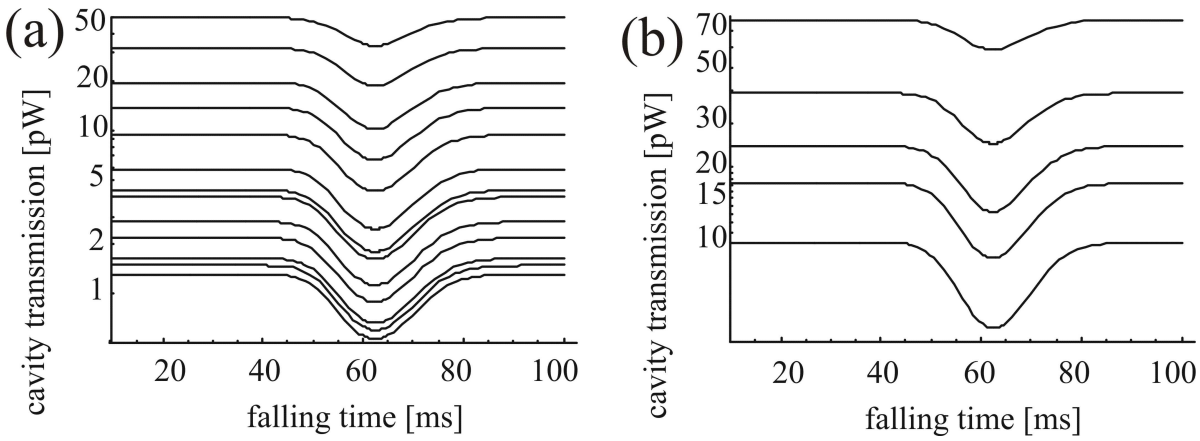

Figure 5.12: Cavity transmission signals predicted by the theory for pump intensities corresponding to those in Figure 5.10 for the PMT measurements in (a) and the PD measurements in (b).

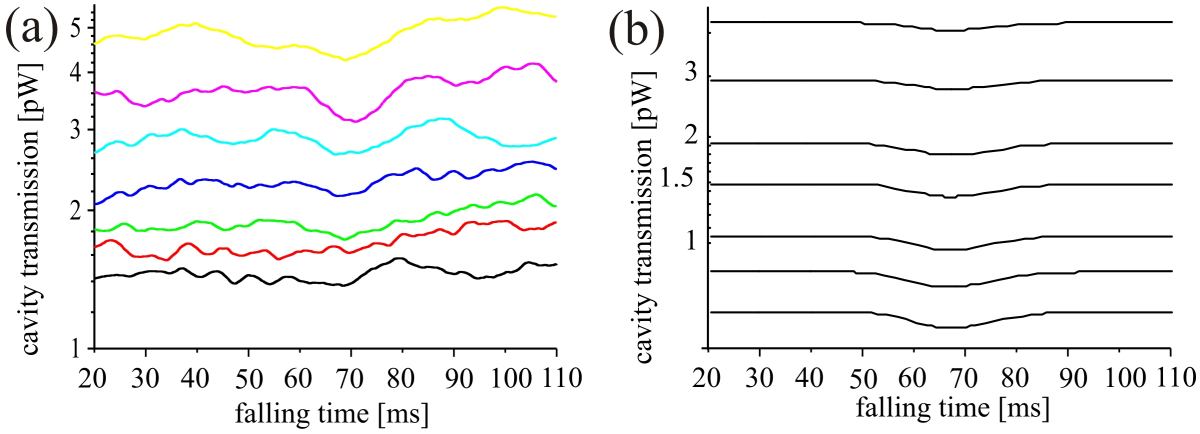

Figure 5.13: Cavity transmission signal from a MOT of 3.5×10^5 atoms being dropped into the cavity. Figure (a) shows the photomultiplier signals. The background level was determined f to be 0.87pW. Figure (b) the theoretical curves, obtained by fitting the relative signal for the maximum absorbtion.

5.3.2 Signals from magnetically guided atoms

Figure 5.16 shows the first signals produced by magnetically guided atoms. The peak signal of the guided atoms is about 60% of the signal from the free falling atoms. Since the guide loading efficiency was measured to be 20%, the overlap integral of atomic density distribution and cavity mode function (see Section 3.5) must have increased by a factor of ≈ 2.8 thanks to the better localization into the cavity mode provided by the magnetic guide. The theoretical results shown in Figure 3.12 yields a factor of 3.1, which confirms the experimental result.

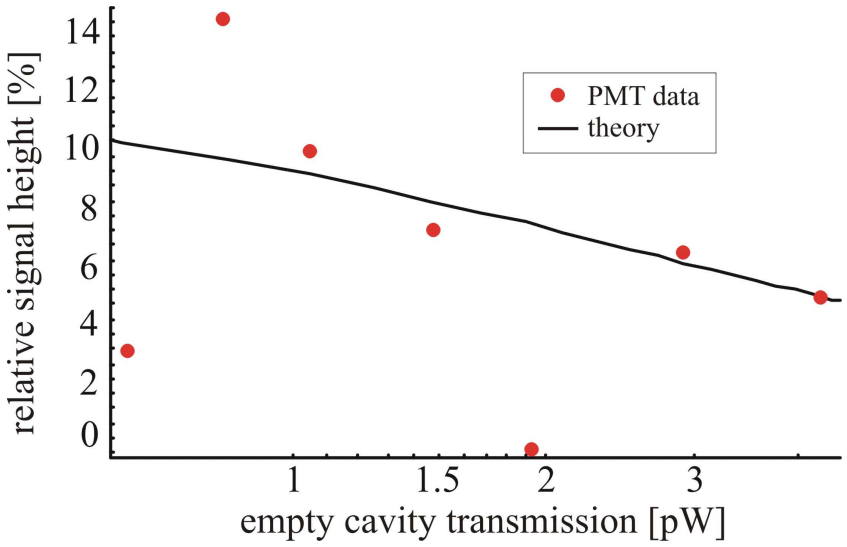

Figure 5.14: The Figure shows the relative drop in the cavity transmission signal due to the atoms. The theory was fitted to the experimental data with atom number and effective coupling constant as fit parameters.

5.3.3 Matching potential parameter

To optimally benefit from the increase in atomic density offered by the guiding potential, one has to match the position of the potential minimum to that of the cavity mode. This is done by varying the wire current while keeping the magnetic bias field constant. According to Equation 5.9, the guide position is changes linearly with the current. A change in the wire current of 12A causes the potential minimum to shift by 2mm. The bias field is kept constant to ensure a constant trap depth.
How the radial guiding potential shape changes is shown in Figure 5.17. The experiment has been performed by loading the atoms into the magnetic guide at the optimal position for the MOT and by afterwards ramping down the wire current within 20ms to the different values. The results are shown in Figure 5.18, where the cavity transmission signal is plotted as a function of time and wire current. The absorption signal is highest at a wire current of 24A. This means that the cavity is located at a distance of 4.3mm from the wire centre. Because of the width of the atomic cloud, and because the signal starts to saturate for the best overlap, the resolution is not better than 1A which corresponds to 200μm.
Having found the position for the best overlap one can now further compress the trap . This is possible, without changing the minimum position, since the gradient of a wire guide scales as

$$\frac{dB}{dx} \propto \frac{I_{\text{wire}}}{r_{\text{min}}^2} \propto \frac{B_{\text{bias}}^2}{I_{\text{wire}}}. \tag{5.10}$$

If the wire current and the bias field are increased by the same factor, the gradient is increased by this factor, while the trap position stays constant. In the actual experiment this was not possible, since the cavity was already quite far from the wire and the wire

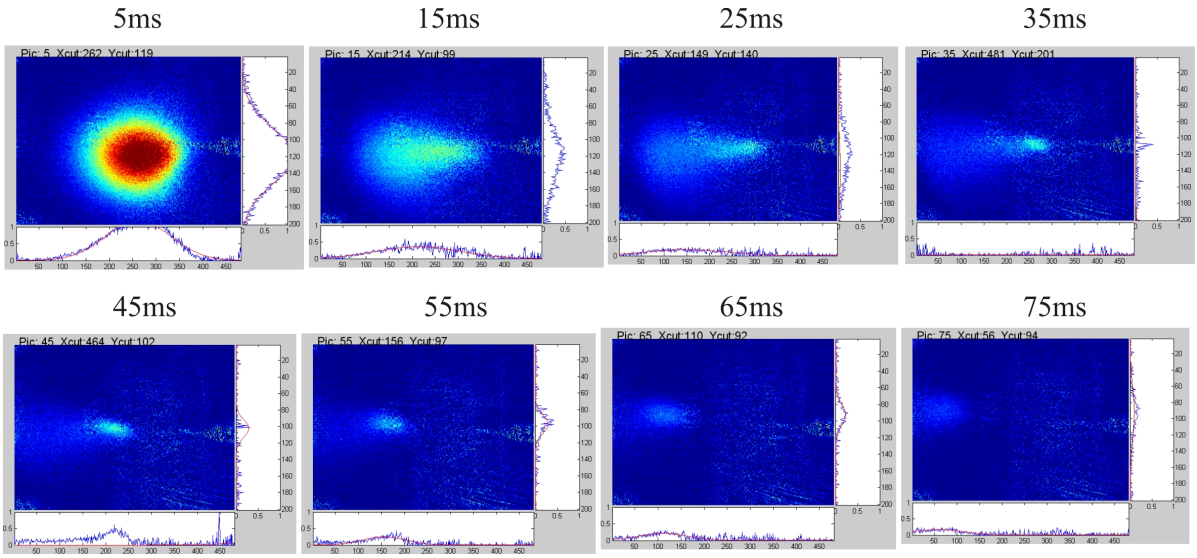

Figure 5.15: Picture series of the trap loading: The atoms are released from the MOT at $t = 0$ and the high-field seekers are quickly repelled. The picture series shows the slow splitting between the free-falling $m_F = 0$ states and trapped low-field seekers. At $t = 65$ms the guided atoms are passing the cavity mode. The camera is looking from the top under a small angle so the atoms are falling slightly to the left.

current and the bias field needed to bring the magnetic potential minimum to the cavity mode were already close to the technical limit.

A compression of the magnetic guide has to be applied in the future chip experiments, where the guiding potential created by micrometer-size wires have to be matched to the even smaller mode waist ($\approx 3\mu$m) of the fibre cavity (see Section 4.8). To achieve a reasonable probability to place single atoms into this mode waist, the magnetic potentials have to be compressed to a size of the same order as the cavity waist. This requires a much higher accuracy than what is currently needed to overlap guiding potential and cavity mode.

5.4 Detector test

Another aspect in these experiments was to test several methods to detect the small changes in the cavity transmission signals when a small number of atoms interacts with a low-finesse, small-mode volume cavity. Some of the experiments have been performed in the high saturation regime, where the cavity transmission signal was detected by a strongly amplified photodiode (see Section 4.6.1). But as soon as smaller atom numbers had to be resolved, the cavity field had to be reduced, since the best detection efficiency was found to be at an intensity at which the atomic transition was just saturated (see Section 3.3.1). The limits of this detection method have been reached in intensity as well as in time resolution.

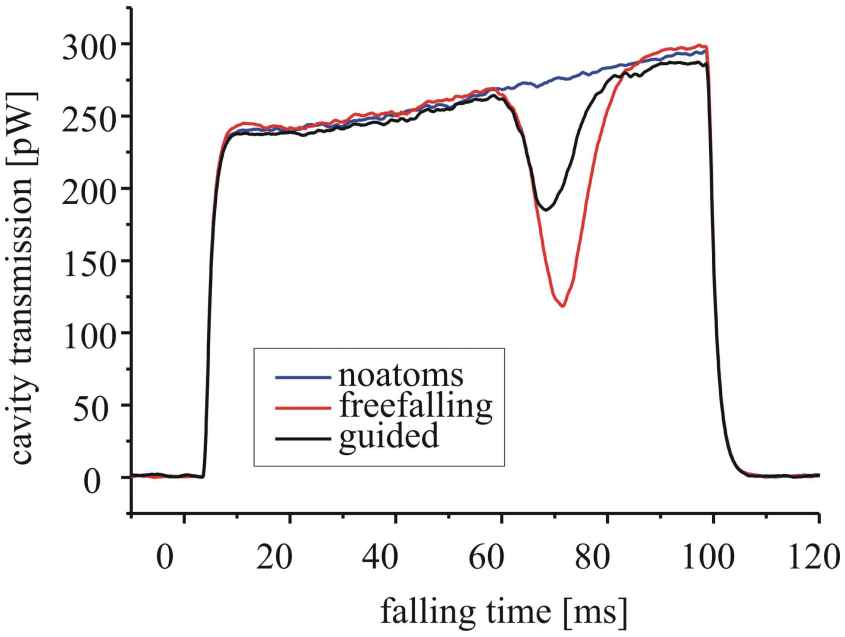

Figure 5.16: The figure shows the first signal from magnetically guided atoms (black curve) in comparison to free-falling atoms (red curve) and no atoms in the cavity (blue curve). The gain in atomic density for the guided atoms almost compensates the guide loading efficiency of only 20%. The general rise of the background signal is due to experimental instabilities, which cause a frequency drift of the cavity after it is released from the lock (see Section 4.5.2).

5.4.1 Photomultiplier

Alternatively a photomultiplier tube (PMT) was used to detect the low intensity transmission signals. In this case, the PMT had a relatively high quantum efficiency of $8-9\%$, which is still poor compared to other devices like avalanche photodiodes. But the big advantage of photomultiplier tubes over these other systems is the intrinsic noise-free amplification, due to the electron multiplication at the multiple dynodes. A gain of 7.6×10^4 was measured for a supply voltage of 1250V.

The PMT was integrated into the experimental setup together with security devices protecting it from being overexposed (see Section 4.6.3). An example of acquired data using the PMT is shown in Figure 5.19. Besides the raw data from a single experimental cycle in Figure 5.19 (a), the smoothed signal which was used for data analysis is shown in Figure 5.19 (b). This smoothing was done by adjacent averaging over 2.5 ms. This averaging makes the PMT signal fluctuations comparable to those of the photodiode, since the latter has a time resolution of only 5ms due to the strong amplification.

The PMT signal was additionally amplified by a current amplifier with a gain of 10^7V/A, which restricted the bandwidth to 20kHz. The noise on the data can be attributed to two sources. The slow damped oscillations are due to acoustic noise by the shutter, which protects the PMT from the MOT-light, acting on the PMT focussing optics. Furthermore, there is a uniform intrinsic noise coming directly from the amplified photomultiplier. This was verified by illuminating the PMT directly, without further noise

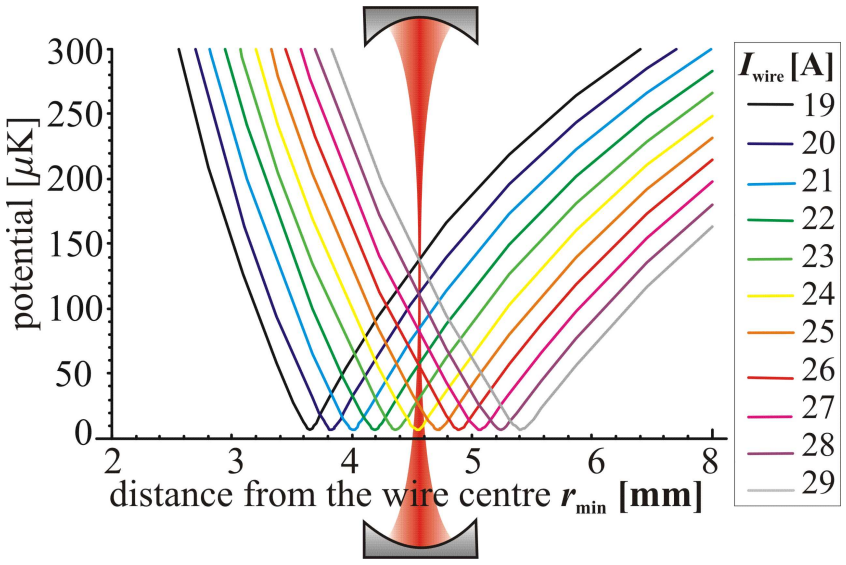

Figure 5.17: The change of the radial guiding potential is shown if the wire current is scanned at a constant magnetic bias field.

sources involved. By Fourier-analyzing this data, no characteristic frequencies have been found, it was basically white noise, whose amplitude increases as the square root of the signal intensity, as show in Figure 5.20 in a log-log-plot. This corresponds exactly to the scaling of Poissonian noise. The theoretical shot noise curve, calculated from the specified values for the PMT quantum efficiency and its gain and from the amplifiers gain and bandwidth is about a factor of two below the measured noise level. This could be deviations of the properties of PMT and amplifier from the specified values.

5.4.2 Heterodyning

Furthermore, a heterodyne detector has been set up (see Section 4.6.2), mainly to access the phase information imprinted on the cavity transmission signal by the atom, as suggested in Section 3.4.1. Since so far only experiments with resonant cavities have been performed, where the phase change due to the intra-cavity atoms is masked by a large amplitude change, the heterodyne detection setup was used to extract also this amplitude signal. A simple envelope detector extracted the amplitude change of the 152MHz beating between the cavity signal and a local oscillator (an injection locked slave laser). With the heterodyne detection scheme the cavity transmission signal is optically amplified, which has the advantage of producing a signal which is in principle only shot noise limited and preserving the signal bandwidth. The detection resolution is therefore only restricted by the cut-off frequency of the envelope detector, which was chosen to be 100kHz (see Section 4.6.2). As a prove of principle, we have detected atomic signals with this setup, which are shown in Figure 5.21. Figure 5.21 (a) shows the experimental data at the full bandwidth, Figure 5.21 (b) the smoothed signal by adjacent averaging over 2.5ms. It is obvious that the extraction of the amplitude, from

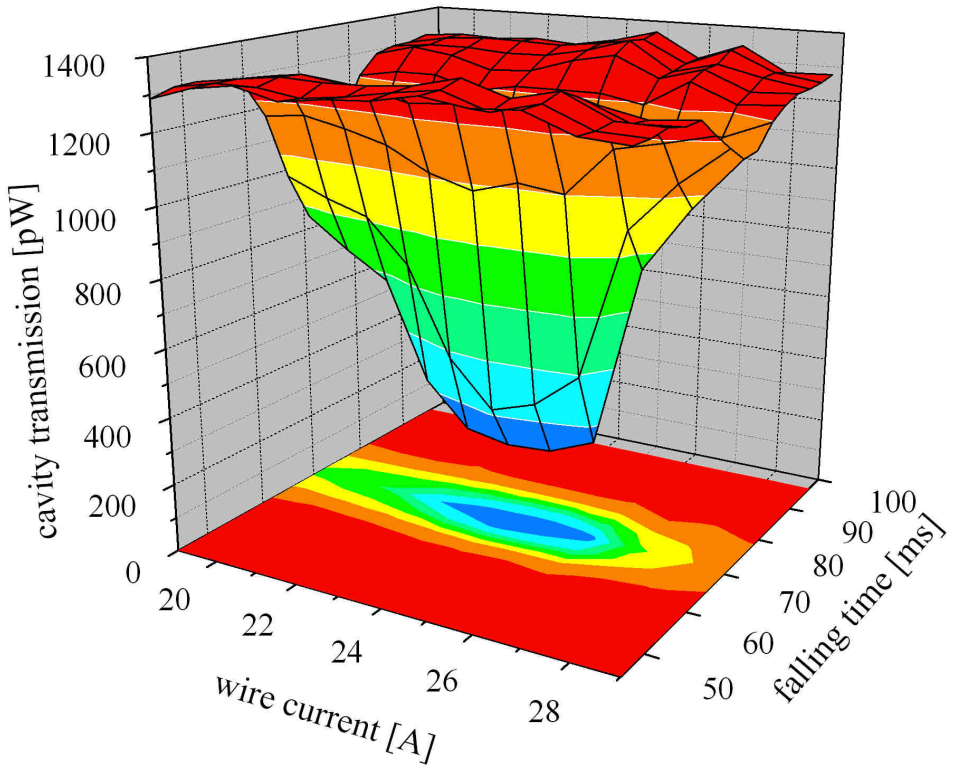

Figure 5.18: Experimental data from the wire current scan. The cavity position can be identified from the point of highest absorption at $I_{\text{wire}} = 24\text{A}$ to be at a distance of 4.3mm from the wire centre.

the oscillating signal, did not succeed perfectly well, but the atomic signal can clearly be extracted. Analysing these data, it was found that the strong, damped oscillations on top of the signal are mainly caused by vibrations of the chamber due to the switching of the big quadrupole coils and by the opening of the shutter before the measurements. Both seem to cause vibrations of the cavity beam with respect to the beam from the slave laser, which influences the interference pattern. It will be crucial to overcome this problem if this setup is used for phase detection, since the detection of a small relative phase between both signals will even more sensitive.

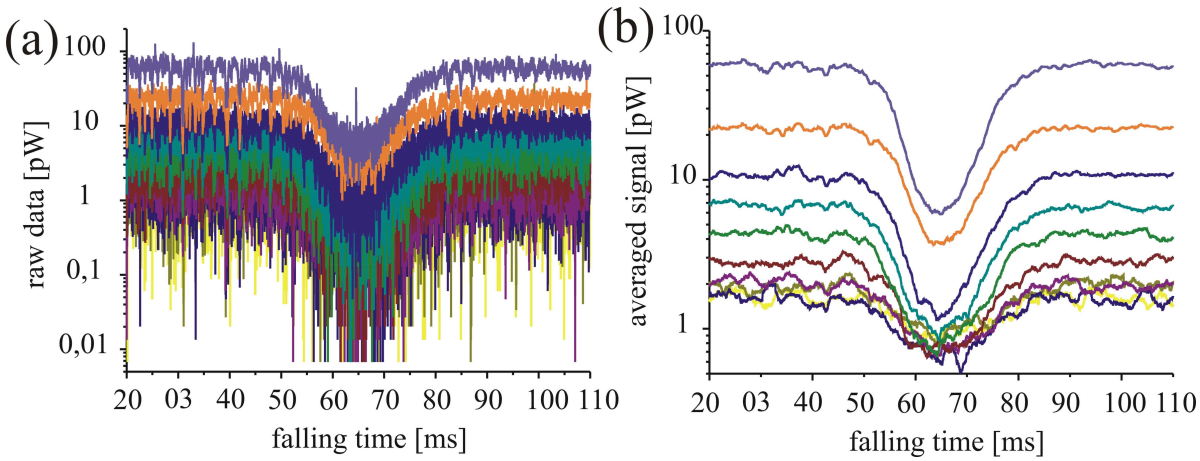

Figure 5.19: The signal from the photomultiplier amplified with 20kHz bandwidth in (a) and averaged over 2.5ms in (b).

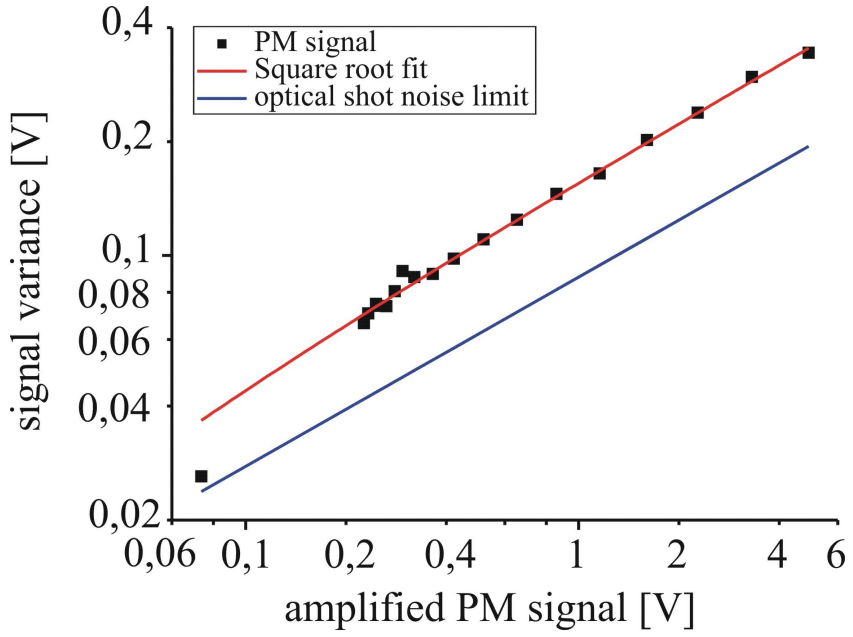

Figure 5.20: Noise level of the Photomultiplier under direct illumination from an attenuated, locked laser. The signal was amplified by a current amplifier with a gain of 10^7, The curve is fitted by a square root function which reflects the Poissonian statistics. The theoretical shot noise level, which is added to the plot, was calculated from the specified detector sensitivity and the amplifier bandwidth.

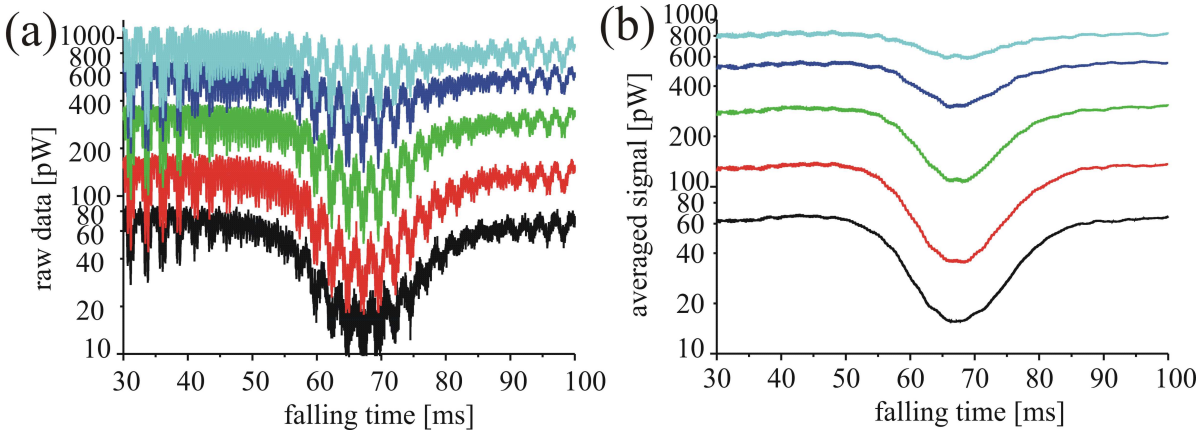

Figure 5.21: Figure (a) shows the raw signal from the envelope detector in the heterodyne setup with a bandwidth of 100kHz. Figure (b) shows the data after adjacent averaging over 2.5ms. The intensity calibration has been done by measuring the background intensity with a calibrated photodiode.

5.5 Results

In this thesis an experiment was designed and set up, with the goal of studying the interaction of cold Rubidium atoms with strongly focussed light fields produced by micro-optical elements, like fibre-cavities and fibre lenses. The philosophy behind these experiments is to miniaturize the optics and thus the light fields they produce to such a degree that the beam diameters approach the order of magnitude of the atomic scattering cross section ($\approx 0.3\mu\text{m}^2$). This strongly enhances the interaction strength between single atoms and these fields (see Section 3.1). The microoptical devices will then be integrated on atom chips, where so far magnetic and electrostatic fields created by current and charge carrying micro-structures are used to manipulate cold neutral atoms [Fol00]. Among the applications for integrated microoptics on atom chips, one of the most pressing is the task of single atom detection. Thus the experiment, which was set up is mainly focussing on the implementation of an on-chip single atom detector.
The central feature of the designed detection scheme was a fibre-optical resonator as described in Section 2.5. In parallel to the development of fabrication techniques for the fibre cavities on atom chips (see Section 4.8.4), a test resonator was build from macroscopic mirrors. This setup allowed to simulate the basic properties of a fibre cavities, i.e. a small waist and relatively low quality mirror, resulting in a low finesse (see Section 4.5). This was implemented by increasing the cavity length as close as possible to the concentric limit of the stability region (see Section 2.4.4), to strongly focus the cavity mode. In this experiment a mode waist of $w_0 = 12\mu\text{m}$ was reached, which is only a factor of 4 larger than the waist of a fibre cavity (see Section 2.5). The mirror quality was chosen to be comparable to those used for fibre cavity. This choise led to a cavity finesses on the order of 1000 (see Section 5.1.3).
Even though this is more than 3 orders of magnitude below the values that are used in CQED experiments with single atoms, the plan to build a single atom detector from such devices is supported by a theory which was developed in the framework of this thesis (see Chapter 3). The theory predicts that the low resonator quality is to some extend compensated by the small mode cross section of the cavity, which enhances the atom-light coupling (see Section 3.2.5). To quantify this prediction, even for the first on-chip fibre cavities which have been produced in our labs (see Section 4.8.4), having a finesse of only $\mathfrak{F} = 60$, in a single-atom detection experiment a signal-to-noise ratio of $S = 3$ can be expected with an integration time $\tau = 10\mu\text{s}$ (see Figure 4.19).
The experiments, which have been performed with the macroscopic test cavity finesse but has verified this theoretical prediction. Measurements with a cavity of waist of $w_0 = 12\mu\text{m}$ and a finesse of $\mathfrak{F} = 1200$ could resolve an average effective atom numbers of $N_{\text{eff}} < 0.1$ within the cavity mode (see Section 5.2.3).
Beside testing the sensitivity of the cavity, experiments have been performed, where atoms were guided to the cavity in a magnetic potential created by a current carrying wire and an external bias field. This allowed to increase the atomic density within the cavity mode (see Section 5.3) and allowed position matching of the atomic cloud and the fibre mode. Thus, first elements of the atom chip technology have been employed.
All these experiments have been used to extensively test the experimental components

under the aspect of their suitability for future atom chip experiments. Special attention was devoted to the issue of detecting the small changes in the cavity transmission. Therefore different detection schemes have been setup and tested (see Section 5.4).
Most of the results can be directly applied to the upcoming experiments with a fibre cavity integrated on an atom-chip.

5.6 Future experimental challenges

Even though the experiments performed in this work were using a macroscopic cavity and macroscopic wire structures to create the magnetic guiding potentials, some of the biggest experimental challenges which will arise when the setup is rebuild into an atom chip experiments could be identified. The main topic will be briefly discussed here. These are the maintenance of a high enough atomic density during the transport to the cavity and the interaction of the atom with stray light, before the cavity mode is reached.

5.6.1 Atomic transport

The experimental results clearly verify the prediction of the theory that single atom detection is possible even with low finesse cavities, due to the increased coupling because of the small cavity mode waist. In a fibre cavity, the mode width is almost constant along the axis in the detection gap (see Section 2.5). So, in contrast to the experiments with near-concentric resonators performed in this thesis, the atom-light coupling does not depend on the position along the cavity axis. The remaining challenge is to place an atom into the cavity mode. A mode volume in the gap of only $43\mu\text{m}^3$ requires an atomic density of $2 \times 10^{10}\text{cm}^{-3}$ at the position of the cavity, in order to find on average one atom in the mode. This is very hard to achieve due the fact that the fibre chip cavity is more than 1cm away from the loading region. So far a simple wire guide, confining only in the two radial directions is intended to guide the atoms there. To be able to also bring a high-density Bose-Einstein condensate to the detection zone, conveyer-belt structures either created by dynamically switched magnetic fields [Hae01], or by moving optical potentials [Kuh03] should be considered for next generation atom chips.
A further difficulty is the guidance of the atoms within the fibre gap, since the fibre diameter is 125μm and the gap is only 6μm wide. This requires an extremely tight confining potential to avoid the atoms being affected by the fibre endfaces. Additionally, the vertical position of the atomic guide has to be matched to the position of the fibre core with μm-accuracy. All together, a precise control of all involved magnetic fields is required.

5.6.2 Stray light

A further experimental difficulty will be the problem of stray light. While the atoms are magnetically guided, complete darkness is needed. On the other hand, the fibre cavity

has to be frequency locked, which so far has been done with the same light beam as the detection. This lock scheme requires constantly a certain amount of light. At every cavity round trip a certain amount of this light is lost from the cavity mode due to the imperfect mode matching of both fibres (see Section 2.5). This light will be scattered into the fibre gap. So very likely, some light will hit the atoms before they reach the cavity mode, which will cause strong losses from the magnetic guide.
There are two strategies to overcome this problem. Firstly one can add a strong second laser, far detuned from the detection light to lock the cavity. The advantage would be that this locking beam could additionally be used to form an intra-cavity dipole trap holding the atoms in cavity mode [Mau05]. The experimental difficulty arising then would be the complete spatially separate the strong locking beam from the weak signal beam before the detection.
A second possibility would be to use a single frequency for cavity lock and detection, but detune it by a few atomic linewidths from the atomic resonance. Regarding the non-disturbance of the atoms in the detection process, this would allow to use a high enough laser power for the lock without influencing the atoms to much before they reach the cavity mode. But off-resonant pumping would require to detect the atoms via the phase shift they imprint onto the cavity signal, which could be done by the heterodyne detector, which was setup within this work (see Section 3.4.1 and 4.6.2).

5.7 Resonator geometries

Besides the fibre cavity setup which is realized now, there are a few alternative geometies, which could be considered in future setups. A present problem is the imperfect mode matching within the fibre gap due to the divergence of the mode outcoupled from a fibre (see Section 2.5). A big improvement would be to introduce focussing elements. The fabrication of concave mirror structures onto the fibre endfaces has already been achieved in our labs as presented in [Sch04].
If one implemented this at both fibre endfaces, a resonator would be formed inside the gap with a much higher finesse of up to $\mathfrak{F} = 1000$ [Sch04], not only because the mode mismatch is eliminated, but also because the epoxy layers between fibres and mirror coating, which are inside the cavity mirrors in the current setup and cause additional losses, would then only be needed outside the cavity. On the other hand, a new difficulty would be the tuning of this gap resonator. In the current this is done by stretching one of the fibres. A compromise could be a resonator created by a concave mirror on one side and a plane uncoated fibre on the other side, where the mirror is implanted in the fibre, which allows to tune the cavity length by a fibre stretcher. More details can be found in [Sch04].
Totally different approaches have followed in other groups working on the same subject. Some of them are very promising, since they seem to be compatible with the atom chip concept. Those will be briefly mentioned in the following. Besides Figure 5.22 (d), which shows a Fabry-Pérot micropost, where the light is emitted vertically [Ger98], the other resonator geometries in Figure 5.22 (a)-(c) are taking advantage the fact that in perfectly

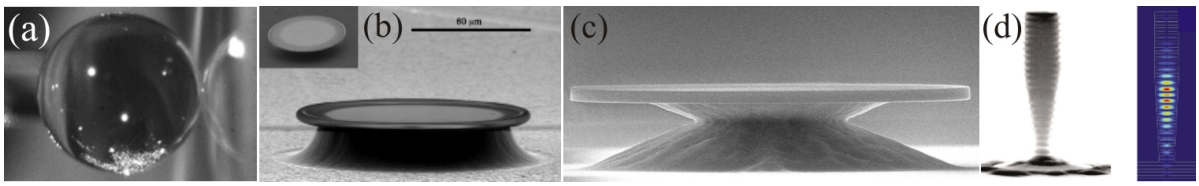

Figure 5.22: The figure shows various microresonator geometries: a microsphere [Ver98] in (a), a microtoroid [Arm03]in (b), a microdisc [Gay99] in (c), and a micropost [Ger98] in (d).

round 2- or 3-dimensional structures light is circling in so-called whispering gallery modes with extremely small loss rates. Figure 5.22 (a)-(c) shows in this order a microsphere [Ver98], a microtoroid [Arm03], and a microdisc [Gay99]. For some of the devices their feasibility for single-atom detection has already been estimated. Mircospheres were studied in [Lon03] and microdiscs in [Ros04].
The resonator geometries in Figure 5.22 (b)-(d) are especially suited for an integration on atom chips, since they could be grown directly onto the chip substrate. The biggest experimental difficulty, if one wants atoms to interact with these resonators, arises from the fact that the resonator modes are not directly accessible, since they travel inside the substrates. The only way to couple atoms to these modes is via the evanescent field, which is leaking out of the resonators. But since this evanescent field is decaying exponentially fast on the scale of the light wavelength, an atom has to be brought as close as $\approx$ 100nm to the surface for the atom-light coupling to be sufficiently strong. To achieve this even in a system with extremely strong control on the atomic position as the atom chip, this is very ambitious.

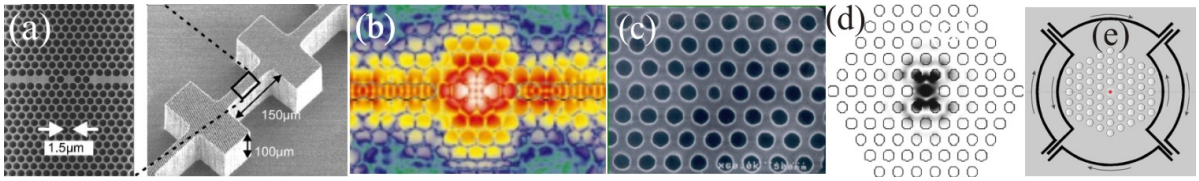

Figure 5.23: The figures shows two photonic bandgap resonators. In (a) the resonator is created by a waveguide interrupted by two mirrors [Kra01]. Figure (b)shows the corresponding intensity pattern. The crystal structure in (c) is optimized to achieve strong coupling to atoms which are dropped into the central hole of the structure [Vuc01], Figure (d) shows the calculated intensities and Figure (e) a possible wire configuration to trap the atoms.

Another interesting class of devices are photonic crystal resonators. These photonic crystals are periodically structured materials (e.g by holes in a dielectric material). The resulting modulation of the index of refraction affects the propagation of light inside these materials. Photonic band gaps [Yab87, Saj87] are created in the same way as electronic energy bands are formed in semiconductor crystals. This has strong effects on the propagation of light. By introducing crystal defect structures, light propagation in certain direction becomes possible again, which allows to create all kinds of optical structures, like waveguides, mirrors, and resonators. Figure 5.23 shows two photonic

crystal resonator geometries. In Figure 5.23 (a), a defect line(the one without holes) creates a linear waveguide, which is interrupted by two holes at each side of the centre, which form the resonator mirrors [Kra01]. The resulting intensity pattern is shown in Figure 5.23 (b). Figure 5.23 (c) shows a resonator which is designed to achieve strong coupling to single atoms dropped into the central hole [Vuc01]. Figure 5.23 (d) shows the calculated intensity pattern and Figure 5.23 (e) shows the photonic crystal together with a wire structure in a Weinstein-Libbrecht configuration [Wei95], which allows to trap atoms just above the central hole [Lev03]. The feasibility of using these resonators for single atom detection is discussed in [Lev04, Mab01].
The big advantage of the photonic crystal resonators is their extremely small mode volume, which can be decreased to the order of λ^3. Concerning the integration on atom chips photonic crystals seem to be very promising. So far, the semiconductor atom-chip substrate serves only for carrying electrical wire structures and optical fibres. If one integrated photonic bandgap structures into this substrate, it would be possible to couple light directly from a fibre into one point at the side of the chip, and to distribute it by waveguide and beamsplitter structures [Bay00, Yu03] to local interaction region. Furthermore, one could think of pushing the integration even further, by fabricating semiconductor laser sources directly into the chip and similarly by integrating semiconductor photo detectors. This would move the complete detection setup into the atom chip.

5.8 Applications

5.8.1 Quantum information processing

Throughout this whole work, the use of small mode volume cavities for single atom detection was discussed. A direct application for such a detector can be found in the field of quantum information processing and computation (QIPC). A state-selective measurement device is one of the five basic requirements for the implementation of quantum computation listed by David Di Vincenzo [DiV00]. If the qubit is encoded in the two hyperfine ground states of a Rubidium atom, two cavities, each in resonance with an optical transition from one or the other hyperfine state, would represent such a device. As shown in Section 3.4.2 a non-destructive detection is not far from being realized with the microcavities discussed in this work.
Beside the use for detection, there is a variety proposals for applications of cavities in quantum computation and quantum communication. In [Cir97, Mab01] quantum networks based on cavity quantum electrodynamics are proposed. The cavities allow to perform the transformation between storage/processing qubits, encoded in the long-living internal states of trapped atoms, and flying qubits, implemented by optical photons. This allows to exchange information and distribute entanglement between the different storage, processing, and detection units.
Finally, there are several universal two qubit gate proposals involving entanglement between an atom and a cavity mode [Dom95, Rau99], between two distant atoms in

cavities [Sor03], between two cavities [Gio00], or between two different modes[Zub03] of one cavity, mediated by an atom.

5.8.2 Sensors, switches, etc.

Besides the field of quantum information, there are other applications for matter interacting with microcavities, which start to be implemented. The field of biochemical microsensors, where cavities are used to enhance the sensitivity of all kinds of spectroscopic techniques and where completely new methods based on cavities have been developed, e.g. the cavity-ring-down-spectroscopy [OKe88], is rapidly growing. Also in this field there exists the trend towards miniaturized and integrated devices [Kri02a, Kri02b]. This is summarized under the keyword lab-on-a-chip. Finally, microcavities play a more and more important role in the field of telecommunication, where complete photonic circuits are integrated on chips. In this context, one recent result was the implementation of an all-optical switch based on a micro-resonator [Alm04].

A Acknowledgment

This work would not have been possible without the support of certain people. But more importantly, I would not have had such a good time during this work without the company of many more people. All of them I would like to thank here. First of all, I thank Chiara for things that words cannot express. I would like to thank Jörg for guiding me through this exciting field of physics and to the steepest powder slopes of Tyrol. I thank Peter for the company during 11 exciting years on the axis Berlin-Innsbruck-Heidelberg. Furthermore, I would like to thank all the people who I met as colleagues and with whom I ended up as friends: alex, Alex, Andreas, Barbara, Berth, Birdy, Björn, Christian, dem Tijor, der Ente, Florian, Jesko, Julian, Ron, Stephan, Thomas, Thorst...Finally, I thank my family.

Bibliography

[Abr98] E.R.I. Abraham and E.A. Cornell. Teflon feedthrough for coupling optical fibers into ultrahigh vacuum systems. *Appl. Opt.*, **37**, (1998).

[Aga97] G.P. Agarwal. *Fibre Optic Communication System.* John Wiley and Sons, New York, (1997).

[Alm04] V. R. Almeida, C. A. Barrios, R. R. Panepucci, and M. Lipson. Biochemical sensors based on polymer microrings with sharp asymmetrical resonance. *Nature*, **431**, 1081, (2004).

[Arc93] J-L. Archambault, L. Reekie, and P.St.J. Russell. High reflectivity and narrow bandwidth fibre gratings written by a single excimer pulse. *Elec. Lett.*, **29**, (1993).

[Ari77] E. Arimondo, M. Inguscio, and P. Violino. Experimental determinations of the hyperfine structure in the alkali atoms. *Rev. Mod. Phys.*, **49**, 31, (1977).

[Arm03] D. Armani, T. Kippenberg, S. Spillane, and K. Vahala. Ultra-high-Q toroid microcavity on a chip. *Nature*, **421**, 925, (2003).

[Bar70] G. Barton. Quantum electrodynamics of spinless particles between conducting plates. *Proc. Roy. Soc. Lond.*, **320**, 251, (1970).

[Bay00] M. Bayindir, B. Temelkuran, and E. Ozbay. Photonic-crystal-based beam splitters. *Appl. Phys. Lett.*, **77**, 3902, (2000).

[Ben65] R. Benumof. Optical pumping theory and experiment. *Am. J. Phys.*, **33**, 151, (1965).

[Ben92] C. H. Bennett, F. Bessette, G. Brassard, L. Salvail, and J. Smolin. Experimental quantum cryptography. *J. Cryptol.*, **1**, 3, (1992).

[Ber94] P.R. Berman (ed.). *Cavity Quantum Electrodynamics.* Academic press, San Diego, (1994).

[Bjo79] G.C. Bjorklund. Frequency-modulation spectroscopy: a new method for measuring weak absorptions and dispersions. *Opt. Lett.*, **5**, 15, (1979).

[Bla01] E. Black. An introduction to Pound-Drever-Hall laser frequency stabalization. *Am. J. Phys.*, **69**, (2001).

[Cas00] D. Cassettari, B. Hessmo, R. Folman, T. Maier, and J. Schmiedmayer. Beam splitter for guided atoms. *Phys. Rev. Lett.*, **85**, 5483, (2000).

[Cir97] J. I. Cirac, P. Zoller, H. J. Kimble, and H. Mabuchi. Quantum state transfer and entanglement distribution among distant nodes in a quantum network. *Phys. Rev. Lett.*, **78**, 3221, (1997).

[Col60] S.A. Collins. Lens-system diffraction integral written in terms of matrix optics. *J. Opt. Soc. Am.*, **60**, 1168, (1960).

[DeM87] F. De Martini, G. Innocenti, G.R. Jacobovitz, and P. Mataloni. Anomalous spontaneous emission time in a microscopic optical cavity. *Phys. Rev. Lett.*, **59**, 2955, (1987).

[Dem03] W. Demtröder. *Laser Spectroscopy.* Springer, Heidelberg, 3 edition, (2003).

[Den99] J. Denschlag, D. Cassettari, and J. Schmiedmayer. Guiding neutral atoms with a wire. *Phys. Rev. Lett.*, **82**, 2014, (1999).

[Dex74] K.H. Drexhage. Interaction of light with monomolecular dye layers. *Prog. Opt.*, **12**, 165, (1974).

[DiV00] D. P. Di Vincenzo. The physical implementation of quantum computation. *Forts. der Physik*, **48**, 771, (2000).

[Dom02] P. Domokos, P. Horak, and H. Ritsch. Quantum description of light-pulse scattering on a single atom in waveguides. *Phys. Rev. A*, **65**, 033832, (2002).

[Dom95] P. Domokos, J. M. Raimond, M. Brune, and S. Haroche. Simple cavity-QED two-bit universal quantum logic gate: The principle and expected performances. *Phys. Rev. A*, **52**, 3554, (1995).

[Don93] L. Dong, J-L. Archambault, L.Reekie, P.St.J.Russell, and D.N.Payne. Bragg gratings in Ce^{3+}-doped fibres written by a single excimer pulse. *Opt. Lett.*, **18**, (1993).

[Dre83] R.W.P. Drever, J.L. Hall, F.V. Kowalski, J.Hough, G.M. Ford, A.J. Munley, and H. Ward. Laser Phase and Frequency Stabalization Using an Optical Resonator. *Appl. Phys. B*, **31**, 97, (1983).

[Dru81] P.D. Drummond. Optical bistablility in a radially varying mode. *IEEE J. Quant. Electr.*, **17**, (1981).

[Ear42] S. Earnshaw. On the nature of the molecular forces which regulate the constitution of the luminferous ether. *Trans. Camb. Phil. Soc.*, **7**, 97, (1842).

[Ein05] A. Einstein. über einen die Erzeugung und Verwandlung des Lichtes betreffenden heuristischen Gesichtspunkt. *Annalen der Physik*, **17**, 132, (1905).

[Ein17] A. Einstein. Zur Quantentheorie der Strahlung. *Phys. Zs.*, **18**, 121, (1917).

[Fol00] R. Folman, P. Krüger, D. Cassettari, B. Hessmo, T. Maier, and J. Schmiedmayer. Controlling cold atoms using nanofabricated surfaces: Atom chips. *Phys. Rev. Lett.*, **84**, 4749, (2000).

[Fol02] R. Folman, P. Krüger, J. Schmiedmayer, J. Denschlag, and C. Henkel. Microscopic atom optics. *Adv. At. Mol. Phys.*, **48**, 263, (2002).

[Gay99] B. Gayral, J. M. Gerard, A. Lemaitre, C. Dupuis, L. Manin, and J. L. Pelouard. High-Q wet-etched gaas microdisks containing inas quantum boxes. *Appl. Phys. Lett.*, **75**, 1908, (1999).

[Ger98] J. M. Gerard, B. Sermage, B. Gayral, B. Legrand, E. Costard, and V. Thierry-Mieg. Enhanced spontaneous emission by quantum boxes in a monolithic optical microcavity. *Phys. Rev. Lett.*, **81**, 1110, (1998).

[Gio00] V. Giovannetti, D. Vitali, P. Tombesi, and A. Ekert. Scalable quantum computation with cavity QED systems. *Phys. Rev. A*, **62**, 032306, (2000).

[Gol01] G.N. Gol'tsman, O. Okunev, G. Chulkova, A. Lipatov, A. Semenov, K. Smirnov, B. Voronov, A. Dzardanov, C. Williams, and R. Sobolewski. Picosecond superconducting single-photon optical detector. *Appl. Phys. Lett.*, **79**, 705, (2001).

[Goy83] P. Goy, J.M. Raimond, M. Gross, and S. Haroche. Observation of cavity-enhanced single-atom spontaneous emission. *Phys. Rev. Lett.*, **50**, 1903, (1983).

[Gro04] S. Groth, P. Krüger, S. Wildermuth, R. Folman, T. Fernholz, D. Mahalu, I. Bar-Joseph, and J. Schmiedmayer. Atom chips: Fabrication and thermal properties. *Appl. Phys. Lett.*, **85**, 2980, (2004).

[Guo90] G. Guoy. Sur une propreite nouvelle des ondes lumineuases. *Compt. Rendue Acad. Sci. (Paris)*, **110**, 1251, (1890).

[Haa01] A. Haase, D. Cassettari, B. Hessmo, and J. Schmiedmayer. Trapping neutral atoms with a wire. *Phys. Rev. A*, **64**, 043305, (2001).

[Hae01] W. Hänsel, P. Hommelhoff, T.W. Hänsch, and J. Reichel. Bose-Einstein condensation on a microelectronic chip. *Nature*, **413**, 498, (2001).

[Hae75] E.L. Raab, M. Prentiss, A. Cable, S. Chu, and D.E. Pritchard. Cooling of gases by laser radiation. *Opt. Comm.*, **13**, 68, (1975).

[Hei87a] D.J. Heinzen, J.J. Childs, J.E. Thomas, and M.S. Feld. Enhanced and inhibited visible spontaneous emission by atoms in a confocal resonator. *Phys. Rev. Lett.*, **58**, 1320, (1987).

[Hei87b] D. J. Heinzen and M. S. Feld. Vacuum radiative level shift and spontaneous-emission linewidth of an atom in an optical resonator. *Phys. Rev. Lett.*, **59**, 2623, (1987).

[Hoc03] C. Hock. Aufbau und Charakterisierung eines Resonators zur Detektion einzelner Atome. Diploma Thesis, University of Heidelberg, (2003).

[Hof04] S. Hofferberth. Experiments with ultracold atoms and Bose-Einstein condensates in microtraps near surfaces. Diploma thesis, University of Heidelberg, (2004).

[Hoo00] C.J. Hood, T.W. Lynn, A.C. Doherty, A.S. Parkins, and H.J. Kimble. The atom-cavity microscope: Single atoms bound in orbit by single photons. *Science*, **287**, 1457, (2000).

[Hoo01] C. Hood, H.J. Kimble, and J. Ye. Characterization of high-finesse mirrors: Loss, phase shift, and mode structure in an optical cavity. *Phys. Rev. A*, **64**, 033804, (2001).

[Hoo98] C.J. Hood, M. S. Chapman, T.W. Lynn, and H.J. Kimble. Real-time cavity QED with single atoms. *Phys. Rev. Lett.*, **80**, 4157, (1998).

[Hor03] P. Horak, B. G. Klappauf, A. Haase, R. Folman, J. Schmiedmayer, P. Domokos, and E. A. Hinds. Possibillity of single-atom detection on a chip. *Phys. Rev. A*, **67**, 043806, (2003).

[Hul85] R.G. Hulet, E.S. Hilfer, and D. Kleppner. Inhibited spontaneous emission by a Rydberg atom. *Phys. Rev. Lett.*, **55**, 2137, (1985).

[Jac99] J.D.Jackson. *Classical electrodynamics*. Wiley, New York, (1999).

[Jay63] E.T. Jaynes and F.W. Cummings. Comparison of quantum and semiclassical radiation theories with application to the beam maser. *IEEE*, **51**, 89, (1963).

[Jhe87] W. Jhe, A. Anderson, E.A. Hinds, D. Meschede, L. Moi, and S. Haroche. Suppression of spontaneous decay at optical frequencies: Test of vacuum-field anisotropy in confined space. *Phys. Rev. Lett.*, **58**, 666, (1987).

[Kee88] A. O'Keefe and D. A.G. Deacon. Cavity ring-down optical spectrometer for absorption measurements using pulsed laser sources. *Rev. Sci. Inst.*, **59**, 2544, (1988).

[Kle81] D. Kleppner. Inhibited spontaneous emission. *Phys. Rev. Lett.*, **47**, 233, (1981).

[Kra01] P. Kramper, A. Birner, M. Agio, C. M. Soukoulis, F. Mu ller, U. Gösele, J. Mlynek, and V. Sandoghdar. Direct spectroscopy of a deep two-dimensional photonic crystal microresonator. *Phys. Rev. B*, **64**, 233102, (2001).

[Kri02a] E. Krioukov, D. J. W. Klunder, A. Driessen, J. Greve, and C. Otto. Integrated optical microcavities for enhanced evanescent-wave spectroscopy. *Opt. Lett.*, **27**, 1504, (2002).

[Kri02b] E. Krioukov, D. J. W. Klunder, A. Driessen, J. Greve, and C. Otto. Sensor based on an integrated optical microcavity. *Opt. Lett.*, **27**, 512, (2002).

[Kru03] P. Krüger, X. Luo, M.W. Klein, K. Brugger, A. Haase, S. Wildermuth, S. Groth, I. Bar-Joseph, R. Folman, and J. Schmiedmayer. Trapping and manipulating neutral atoms with electrostatic fields. *Phys. Rev. Lett.*, **91**, 233201, (2003).

[Kru04] P. Krüger. *Coherent matter waves near surfaces.* PhD thesis, University of Heidelberg, (2004).

[Kuh02] A. Kuhn, M. Hennrich, and G. Rempe. Deterministic single-photon source for distributed quantum networking. *Phys. Rev. Lett.*, **89**, 067901, (2002).

[Kuh03] S. Kuhr, W. Alt, D. Schrader, I. Dotsenko, Y. Miroshnychenko, W. Rosenfeld, M. Khudaverdyan, V. Gomer, A. Rauschenbeutel, and D. Meschede. Coherence properties and quantum state transportation in an optical conveyor belt. *Phys. Rev. Lett.*, **91**, 213002, (2003).

[Lea02] A.E. Leanhardt, A.P. Chikkatur, D. Kielpinski, Y. Shin, T. L. Gustavsonand W. Ketterle, and D.E. Pritchard. Propagation of bose-Einstein condensates in a magnetic waveguide. *Phys. Rev. Lett.*, **89**, 040401, (2002).

[Lev03] B. Lev. Fabrication of micro-magnetic traps for cold neutral atoms. *Quantum Information and Computation,* Special Issue on Implementation of Quantum Computation, **3**, 450, (2001).

[Lev04] B. Lev, K. Srinivasan, P. Barclay, O. Painter, and H. Mabuchi. Feasibility of detecting single atoms using photonic bandgap cavities. *Nanotechnology*, **15**, (2004).

[Liu05] X. Liu et al. Fabrication of alignment structures for a fiber resonator using deep uv lithography, (2005). to be published.

[Lon03] R. Long, T. Steinmetz, P. Hommelhoff, W. Hänsel, T. W. Hänsch, and J. Reichel. Magnetic microchip traps and single atom detection. *Phil. Trans. R. Soc. Lond.*, **361**, 1375, (2003).

[Lug84] L.A. Lugiato. Theory of optical bistablility. *Prog. Opt.*, **21**, 71, (1984).

[Luo04] X. Luo, P. Krüger, K. Brugger, S. Wildermuth, H. Gimpel, M.W. Klein, S. Groth, R. Folman, I. Bar-Joseph, and J. Schmiedmayer. An atom fiber for guiding cold neutral atoms. *Opt. Lett.*, **29**, 2145, (2004).

[Mab01] H. Mabuchi, M. Armen, B. Lev, M. Loncar, J. Vuckovic, H. J. Kimble, J. Preskill, M. Roukes, and A. Scherer. Quantum networks based on cavity QED. *Quantum Information and Computation 1, Special Issue on Implementation of Quantum Computation*, **1**, 7, (2001).

[Maj32] E. Majorana. Atomini orientati in campo magnetico variable. *Nouvo Cimento*, **8**, 43, (1932).

[Mat02] H. Mathée. Aufbau und Charakterisierung einer magnetooptischen Falle für Experimente mit Atomchips. Diploma thesis, University of Heidelberg, (2002).

[Mau04] P. Maunz, T. Puppe, I. Schuster, N. Syassen, P. W. H. Pinkse, and G. Rempe. Cavity cooling of a single atom. *Nature*, **428**, 50, (2004).

[Mau05] P. Maunz, T. Puppe, I. Schuster, N. Syassen, P.W.H. Pinkse, and G. Rempe. Normal-mode spectroscopy of a single bound atom-cavity system. *Phys. Rev. Lett.*, **94**, 033002, (2005).

[McK03] J. McKeever, A. Boca, A. D. Boozer, J. R. Buck, and H. J. Kimble. Experimental realization of a one-atom laser in the regime of strong coupling. *Nature*, **425**, 268, (2003).

[McK04] J. McKeever, A. Boca, A. D. Boozer, R. Miller, J. R. Buck, A. Kuzmich, and H. J. Kimble. Deterministic generation of single photons from one atom trapped in a cavity. *Science*, **303**, 1992, (2004).

[Mes85] D. Meschede, H. Walther, and G. Mller. One-atom maser. *Phys. Rev. Lett.*, **54**, 1985, (1985).

[Mil05] MiLaSys technologies GmbH. http://www.milasys.de/.

[Mil73] P.W. Milonni and P.L. Knight. Spontaneous emission between mirrors. *Opt. Comm.*, **9**, 119, (1973).

[Mor73] H. Morawitz. Superradiant level shift and its possible detection in a transient optical experiment. *Phys. Rev. A*, **7**, 1148, (1973).

[Nie00] M.A. Nielsen and I.L. Chuang. *Quantum computation and Quantum information*. Cambridge university press, Cambridge, (2000).

[OKe88] A. O'Keefe and D.A.G. Deacon. Cavity ring-down spectroscopy for absorption measurements using pulsed laser sources. *Rev. Sci. Inst.*, **59**, 2544, (1988).

[Ott01] H. Ott, J. Fortagh, G. Schlotterbeck, A. Grossmann, and C. Zimmermann. Bose-Einstein condensation in a surface microtrap. *Phys. Rev. Lett.*, **87**, 230401, (2001).

[Pay01] F. Payr. Ein orts- und zeitaufgelöster Detektor für kalte Li-Atome. Diploma thesis, University of Innsbruck, (2001).

[Pin00] P.W.H. Pinkse, T. Fischer, P. Maunz, and G. Rempe. Trapping an atom with single photons. *Nature*, **404**, 365, (2000).

[Pur46] E. M. Purcell. Spontaneous emission probabilities at radio frequencies. *Phys. Rev.*, **69**, 681, (1946).

[Raa87] E. Raab, M. Prentiss, A. Cable, S. Chu, and D. Pritchard. Trapping of neutral sodium atoms with radiation pressure. *Phys. Rev. Lett.*, **59**, 2631, (1987).

[Rau00] A. Rauschenbeutel, G. Nogues, S. Osnaghi, P. Bertet, M. Brune, J.M. Raimond, and S. Haroche. Step-by-step engineered multiparticle entanglement. *Science*, **288**, 2024, (2000).

[Rau99] A. Rauschenbeutel, G. Nogues, S. Osnaghi, P. Bertet, M. Brune, J. M. Raimond, and S. Haroche. Coherent operation of a tunable quantum phase gate in cavity QED. *Phys. Rev. Lett.*, **83**, 5166, (1999).

[Rem91] G. Rempe, R.J. Thompson, R.J. Brecha, W.D. Lee, and H.J. Kimble. Absorptive optical bistablility in two-state atoms. *Phys. Rev. A*, **43**, (1991).

[Rem92] G. Rempe, R. J. Thompson, H. J. Kimble, and R. Lalezari. Measurement of ultralow losses in an optical interferometer. *Opt. Lett.*, **17**, 363, (1992).

[Ric95] L. Ricci, M. Weidemüller, T. Esslinger, A. Hemmerich, C. Zimmermann, V. Vuletic, W. Knig, and T.W. Hänsch. A compact grating-stabilized diode laser system for atomic physics. *Opt. Comm.*, **17**, 541, (1995).

[Roh96] H. Rohde. Injektionsstabilisierung von Laserdioden. Diploma thesis, University of Göttingen, (1996).

[Ros04] M. Rosenblit, P. Horak, S. Helsby, and R. Folman. Single-atom detection using whispering gallery modes of microdisk resonators. *Phys. Rev. A*, **70**, 053808, (2004).

[Saj87] J. Sajeev. Localization and the density of states for an electron in a quantized elastic continuum. *Phys. Rev. B*, **35**, 9291, (1987).

[San92] V. Sandoghdar, C.I. Sukenik, E.A. Hinds, and S. Haroche. Vacuum radiative level shift and spontaneous-emission linewidth of an atom in an optical resonator. *Phys. Rev. Lett.*, **68**, 3432, (1992).

[Sch03] S. Schneider, A. Kasper, Ch. vom Hagen, M. Bartenstein, B. Engeser, T. Schumm, I. Bar-Joseph, R. Folman, L. Feenstra, and J. Schmiedmayer. Bose-einstein condensation in a simple microtrap. *Phys. Rev. A*, **89**, 023612, (2003).

[Sch04] M. Schwarz. Aufbau eines Glasfaserresonators zur Detection einzelner Atome auf einem Atomchip. Diploma thesis, University of Heidelberg, (2004).

[Sch99] W. Schnemann, H. Engler, R. Grimm, M. Weidemller, and M. Zielonkowski. Simple scheme for tunable frequency offset locking of two lasers. *Rev. Sci. Inst.*, **70**(1), 242, (1999).

[Sie86] A. Siegman. *Lasers*. University Science Books, Mill Valley, CA, (1986).

[Sor03] Anders S. Sørensen and Klaus Mølmer. Measurement induced entanglement and quantum computation with atoms in optical cavities. *Phys. Rev. Lett.*, **91**, 097905, (2000).

[Tho92] R.J. Thompson, G. Rempe, and H. J. Kimble. Observation of normal mode splitting for an atom in an optical cavity. *Phys. Rev. Lett.*, **68**, 1132, (1992).

[Tra68] M. Travis and F.W. Cummings. Exact solution for an N- molecule radiation-field hamiltonian. *Phys. Rev.*, **170**, 379, (1968).

[Tre04] P. Treutlein, P. Hommelhoff, T. Steinmetz, T.W. Hänsch, and J. Reichel. Coherence in microchip traps. *Phys. Rev. Lett.*, **92**, 203005, (2004).

[Ums99] G. Umshaus. Eine magneto-optische Falle für Lithium. Master's thesis, University of Innsbruck, (1999).

[Ver98] D. W. Vernooy, V. S. Ilchenko, H. Mabuchi, E. W. Streed, and H. J.Kimble. High-q measurements of fused-silica microspheres in the near infrared. *Opt. Lett.*, **23**, 247, (1998).

[Vuc01] J. Vuckovic, M. Loncar, H. Mabuchi, and A. Scherer. Design of photonic crystal microcavities for cavity QED. *Phys. Rev. E*, **65**, 016608, (2001).

[Wei95] J.D. Weinstein and K.G Libbrecht. Microscopic magnetic traps for neutral atoms. *Phys. Rev. A*, **52**, 4004, (1995).

[Wil02] M. Wilzbach. Aufbau und Charakterisierung eines Resonators zur Detektion einzelner Atome. Diploma thesis,University of Heidelberg, (2002).

[Wil04] S. Wildermuth, P. Krüger, C. Becker, M. Brajdic, S. Haupt, R. Folman A. Kasper, and J. Schmiedmayer. Optimized mageto-optical trap for experiments with ultracold atoms near surfaces. *Phys. Rev. A*, **69**, 030901(R), (2004).

[Wil20] M. Wilzbach. *The Art of Doing Nothing*. PhD thesis, University of Heidelberg, (Sanktnimmerleinstag).

[Yab87] E. Yablonovitch. Inhibited spontaneous emission in solid-state physics and electronics. *Phys. Rev. Lett.*, **58**, 2059, (1987).

[Yu03] X. Yu and S. Fan. Bends and splitters for self-collimated beams in photonic crystals. *Appl. Phys. Lett.*, **83**, 3251, (2003).

[Zub03] M. S. Zubairy, M. Kim, and M. O. Scully. Cavity-QED-based quantum phase gate. *Phys. Rev. A*, **68**, 033820, (2003).

[vEnk00] S. J. van Enk and H. J. Kimble. Single atom in free space as a quantum aperture. *Phys. Rev. A*, **61**, 051802, (2000).

[vEnk01] S. J. van Enk and H. J. Kimble. Strongly focused light beams interacting with single atoms in free space. *Phys. Rev. A*, **63**, 023809, (2001).

[vEnk04] S. J. van Enk. Atoms, dipole waves, and strongly focused light beams. *Phys. Rev. A*, **69**, 043813, (2004).